Technische Universität München
TUM School of Medicine and Health

Functional analysis of MEIS transcription factors during neural development

Volker Richard Kittke

Vollständiger Abdruck der von der TUM School of Medicine and Health der Technischen Universität München zur Erlangung eines

Doktors der Naturwissenschaften (Dr. rer. nat.)

genehmigten Dissertation.

Vorsitz: Prof. Dr. Thomas Misgeld

Prüfende der Dissertation:

1. Prof. Dr. Juliane Winkelmann
2. Prof. Dr. Wolfgang Enard

Die Dissertation wurde am 19.07.2024 bei der Technischen Universität München eingereicht und durch die TUM School of Medicine and Health am 04.12.2024 angenommen.

Table of Contents

Abbreviations

AAVS1	adeno-associated virus integration site 1
ATAC	assay for transposase-accessible chromatin using sequencing
BrdU	bromodeoxyuridine
CCR	closed chromatin region
CGE	caudal ganglionic eminence
ChIP-seq	chromatin immunoprecipitation sequencing
FRiP	fraction of reads in peaks
GE	ganglionic eminence
GWAS	genome-wide association study
HA	hemagglutinin
HCNR	highly conserved non-coding region
hNSC	human neural stem cell
HSPC	hematopoietic stem and progenitor cells
IDR	irreproducible discovery rate
IF	immunofluorescence
IP	immunoprecipitation
iPSC	induced pluripotent stem cell
ISH	in-situ hybridisation
IZ	intermediate zone
LCS	lateral cortical stream
LD	linkage disequilibrium
LGE	lateral ganglionic eminence
MAF	minor allele frequency
MGE	medial ganglionic eminence
miRNA	micro RNA
mRNA	messenger RNA
MSN	medium spiny projection neuron
MZ	marginal zone
NPC	neural progenitor cell
OCR	open chromatin region
PCX	piriform cortex
PHH3	phospho-histone H3
RA	retinoic acid
POA	preoptic area
qPCR	quantitative real-time PCR
RG	radial glia cell
RLS	restless legs syndrome
s.e.	standard error
sd	standard deviation
SNP	single nucleotide polymorphism
SNV	single nucleotide variant
SVZ	subventricular zone
TSS	transcriptional start site
VMS	ventral migratory stream
vSTR	ventral striatum
VZ	ventricular zone

Summary

Restless legs syndrome (RLS) is a common neurological disorder with combined contribution of environmental and genetic risk factors, the strongest being located within the *MEIS1* gene. Its highly conserved paralog *MEIS2* is also located in an RLS risk locus. Genome-wide association studies (GWAS) imply a neurodevelopmental component in RLS, with the developing forebrain likely being involved in the underlying mechanism.

My overall goal was to elucidate the regulation and function of the homeodomain transcription factor MEIS1 during embryonic brain development and to identify putative relations with RLS.

Thus, I investigated expression patterns of MEIS1 in the embryonic mouse forebrain by immunofluorescence, specifying new regions of expression as well as confirming previously described patterns. Highest MEIS1 concentration was observed in the piriform cortex, ventral striatum and prospective amygdala. I proved MEIS1 and MEIS2 are co-expressed in inhibitory spiny projection neurons of the developing striatum, a brain region previously implicated in RLS. Furthermore, co-immunostaining of MEIS1 with neuronal markers indicated that cells with high MEIS1 expression in the piriform cortex and ventral striatum are likely of the inhibitory neuron or glial lineage.

To study MEIS in human neural development, I first generated three-dimensional cerebral organoids from induced pluripotent stem cells (iPSC). These organoids displayed basic structures of the embryonic forebrain and expressed MEIS along with neural marker genes, similar to expression patterns in the developing mouse forebrain. Subsequently, I generated MEIS1-deficient iPSC by employing CRISPR/Cas9 genome editing and verified their potency to differentiate towards neural lineage cells, to be used in future in-vitro experiments.

Finally, I investigated downstream effectors of MEIS1 by chromatin immunoprecipitation sequencing (ChIP-seq) in human neural stem cells. Hereby, I identified direct target genes, many of which are implicated in RLS, brain development or physiology of postnatal neurons.

To evaluate implications of MEIS1 binding sites in RLS, I integrated ChIP-seq and chromatin accessibility data with summary statistics of RLS GWAS. While MEIS1 binding sites in general did not display enriched RLS heritability, human neural stem

cells were identified as a putative cell type involved in the pathophysiology of RLS. Finally, I determined a previously undescribed DNA motif within MEIS1 binding sites, specific to human neural stem cells, supposedly representing the binding motif of a transcriptional co-regulator.

Together, these findings specify the role of MEIS1 in neural stem cells as well as its spatiotemporal expression in the developing brain, providing a basis for future research on the possible cell types involved in RLS.

Zusammenfassung

Das Restless Legs Syndrom (RLS) ist eine häufige neurologische Erkrankung, hervorgerufen durch eine Kombination aus Umwelt- und genetischen Faktoren, wovon sich der stärkste im *MEIS1* Gen befindet. Das hochkonservierte, paraloge Gen *MEIS2* befindet sich ebenfalls in einem Risikolocus für RLS. Genomweite Assoziationsstudien (GWAS) legen eine entwicklungsbedingte Komponente des RLS nahe, wobei das embryonale Vorderhirn wahrscheinlich in den zugrunde liegenden Mechanismus von RLS involviert ist.

Das Ziel dieser Arbeit war es, die Regulierung und Funktion von MEIS1 während der Embryonalentwicklung auf mögliche Zusammenhänge mit der Biologie des RLS zu erforschen.
Zu diesem Zweck untersuchte ich zunächst Expressionsmuster von MEIS1 im embryonalen Vorderhirn der Maus durch Immunfluoreszenz, und identifizierte sowohl bisher unbeschriebene, als auch bekannte Expressionsregionen. Die höchste MEIS1-Konzentration wurde im piriformen Kortex, im ventralen Striatum und in der prospektiven Amygdala beobachtet. Ich konnte nachweisen, dass MEIS1 zusammen mit MEIS2 in Projektionsneuronen des sich entwickelnden Striatums exprimiert wird. Koexpressionsmuster von MEIS1 mit neuronalen Markergenen deuteten darauf hin, dass Zellen mit einer hohen MEIS1-Expression im piriformen Kortex und im ventralen Striatum wahrscheinlich zur Linie der inhibitorischen Neuronen oder Glia gehören.
Um die MEIS-Transkriptionsfaktoren während der neuronalen Entwicklung in menschlichen Zellen zu untersuchen, wurden zunächst zerebrale Organoide aus menschlichen induzierten pluripotenten Stammzellen (iPSC) erzeugt. Diese Organoide wiesen Grundstrukturen des embryonalen Vorderhirns auf, wobei Expressionsmuster von MEIS Transkriptionsfaktoren und neuronalen Markergenen mit dem entwickelnden Vorderhirn übereinstimmten. Anschließend erzeugte ich mit Hilfe des CRISPR/Cas9 Systems MEIS1-knockouts in iPS-Zellen und wies deren Fähigkeit nach, sich in Zellen der neuronalen Linie zu differenzieren, um in zukünftigen in vitro Experimenten verwendet werden zu können.
Schließlich untersuchte ich genetische Effektoren von MEIS1 durch Chromatin-Immunpräzipitations-Sequenzierung (ChIP-seq) in menschlichen neuronalen Stammzellen. Auf diese Weise konnten direkte Zielgene im neuronalen Kontext

identifiziert werden, von denen viele mit RLS, der Gehirnentwicklung und der Funktionalität postnataler Neuronen in Verbindung stehen.

Um die mögliche Bedeutung von MEIS-Bindungsstellen für RLS zu beurteilen, wurden ChIP-seq- und Chromatin-Zugänglichkeitsdaten mit einer genomweiten Assoziationsstudien (GWAS) von RLS-Patienten kombiniert. Während MEIS-Bindungsstellen im Allgemeinen keine ehöhte Heritabilität für RLS aufwiesen, wurden menschliche neuronale Stammzellen als ein potentieller Zelltyp identifiziert, der an der Pathophysiologie des RLS beteiligt ist.

Schlussendlich konnte ich ein bisher unbeschriebenes DNA-Motiv innerhalb der MEIS-Bindungsstellen identifizieren, welches spezifisch für menschliche neuronale Stammzellen ist und vermutlich das Bindemotiv eines transkriptionellen Co-Regulators darstellt.

Zusammengenommen präzisieren diese Ergebnisse die Rolle von MEIS1 in neuronalen Stammzellen sowie seine räumlich-zeitliche Expression im sich entwickelnden Gehirn, und bilden somit eine Grundlage für künftige Forschungen zu an RLS beteiligten Zelltypen.

1 Introduction

1.1 Restless legs syndrome: clinical picture

Restless legs syndrome (RLS) is one of the most common neurological disorders in Europe and North America, with a prevalence of 2-10% (Allen et al., 2010; Allen et al., 2011). Incidence increases with age, with women being diagnosed twice as often as men (Allen et al., 2005; Hening et al., 2004).

Patients usually suffer from sensations of discomfort in their legs during periods of rest, which heightens during the evening and night. Symptoms in other parts of the body are less common (Ruppert, 2019). While patients' descriptions of these sensations vary, they agree that only movement can bring relief, albeit only temporarily. Consequently suffering from insomnia, patients experience significantly reduced quality of life (Allen et al., 2011). Severity, frequency and duration of symptoms vary largely, and are found sufficiently severe to warrant medical treatment in over 2% of the general population (Allen et al., 2005).

While dopaminergic drugs have been used as first-line treatment against RLS for decades, they are often accompanied by a gradual loss of efficacy and often by worsening of the symptoms, known as augmentation (Earley et al., 2017). To prevent this phenomenon, current treatment strategies include a variety of dopaminergics, dopamine agonists, opiates and α2δ calcium channel blockers (Trenkwalder et al., 2018; Winkelmann et al., 2018).

RLS occurs both primary (idiopathic), and secondary to pre-existing conditions, which include renal insufficiency, pregnancy, iron deficiency, and diabetes. RLS prevalence in neurodegenerative disorders is less clear but may be masked by dopaminergic medication, e.g. in Parkinson's disease (Garcia-Borreguero et al., 2011).

The pathophysiology underlying RLS is to date still poorly understood, but it is generally accepted that both environmental and genetic factors contribute to the disorder. Mechanisms involved in RLS are sensorimotor signalling, especially dopaminergic signalling, as well as brain iron homeostasis, although the detailed modes of their contributions remain unclear (Koo et al., 2016). Brain imaging studies of RLS patients revealed brain iron deficiency in the thalamus, putamen, caudate nucleus and substantia nigra, while systemic iron levels did not indicate an association with RLS (Allen et al., 2001; Earley et al., 2006; Godau et al., 2008).

Involvement of dopamine pathways seems evident, since dopaminergics effectively mitigate symptoms of RLS (Trenkwalder et al., 2018). Further imaging studies of the basal ganglia, which are involved in the majority of dopamine pathways, revealed several aberrations including an increase in striatal dopamine and decreased dopamine transporter levels (Earley et al., 2011; Earley et al., 2013; Earley et al., 2017). Furthermore, decrease in D2R dopamine receptor and increased tyrosine hydroxylase in the putamen and substantia nigra were reported (Connor et al., 2009). In the thalamus, which processes and relays sensory information to the cortex, fMRI studies suggested increased neuronal activity in RLS patients (Astrakas et al., 2008; Bucher et al., 1997; Margariti et al., 2012). Furthermore, mouse models with deletions of dopamine receptor D3 displayed increased locomotor activity and sensory excitability (Meneely et al., 2018).

Since subjective perception by patients is the most reliable way to diagnose RLS (Winkelmann et al., 2007a), determination of the RLS-phenotype by objective and specific criteria remains a key aspect required to improve understanding of the disorder. As the mechanisms behind RLS are still unclear, identification and characterization of the genetic components will shed light on genetic variants conveying risk for RLS, and thus lead to better understanding of its underlying pathophysiology.

1.2 Genetic component of RLS

1.2.1 Early studies

Already in the first half of the 20th century, RLS was often observed to be passed on from parent to offspring, demonstrating a familial component of the disease (Oppenheim, 1923). Subsequent studies of RLS in families pointed towards an autosomal dominant inheritance (Ekbom, 1960). Recent studies estimate family history in 60% of RLS patients (Winkelmann et al., 2007a), and depict an intricate aetiology in which both genetic factors and environmental conditions contribute.

Early-onset patients typically show a family history more frequently than late-onset patients (Winkelmann et al., 2007a). In cases where RLS manifests at a later age, symptoms usually do not progress, and family history is less common. These findings indicate that multiple aetiologies for RLS exist, as well as different genetic predispositions and varying environmental factors (Mathias et al., 2006). Subsequently, linkage studies in families displaying an early onset of the disease

were conducted, but never identified causally related sequence variants, although several loci have been suggested by these studies (Desautels et al., 2005, Pichler et al., 2006).

1.2.2 Genome-wide association studies (GWAS) identified *MEIS1* as strongest RLS risk factor

Genome-wide association studies (GWASs) have been used to associate disease phenotypes and genomic regions, by comparing variable genomic regions (variants) of RLS patients with age-matched controls. Depending on the penetrance and frequency of the genetic variants, hundreds to tens of thousands of individuals must be tested to identify significant differences in allele frequencies.

In GWAS, the variants tested are single nucleotide polymorphisms (SNPs). The SNP alleles are identified for each individual, typically with microarray chips that can test up to several million SNPs. Due to genetic linkage, SNPs in close proximity to each other tend to contain the same combination of alleles, referred to as a haplotype. Thus, the SNPs serve as indicators for genomic elements in the vicinity, facilitating the deduction of alleles of nearby genes and regulatory elements.

The first successful GWAS discovered an association of RLS with loci within intronic regions in the *MEIS1* and *BTBD9* genes, as well as an intergenic region near *MAP2K5* and *LBXCOR1* (Winkelmann et al., 2007b). Subsequent studies confirmed these findings, establishing the *MEIS1* locus as the strongest genetic risk factor for RLS with an odds ratio of 1.92, and identifying a total of 19 RLS-associated loci (Schormair et al., 2008; Schormair et al., 2017; Winkelmann et al., 2011). Most recently, this number was extended to 164 risk loci (Schormair et al., 2024).

Analysis of genes located in RLS-associated regions showed enrichment for regulators of neurogenesis and neural circuit formation, axon guidance and synaptogenesis as well as DNA damage repair, all of which are key features for the development and maintenance of the central nervous system (Schormair et al., 2017, Schormair et al., 2024). GWAS are the first step towards solving the puzzle of genetic predisposition for RLS. The knowledge about the genetic factors involved in RLS also provides a prerequisite to study the underlying molecular mechanism of the disease. However, as loci discovered in RLS-GWASs only account for 10% of heritability, further variants must be identified to complete the picture (Schormair et al., 2017). Since disease-associated regions found in GWAS usually span tens of kilobases, the

search for causative variants is a lengthy process and requires characterization of individual genes and regulatory elements in appropriate model systems.

1.2.3 Physiological and genomic studies implicate *MEIS1* in RLS

The strongest RLS-association of any SNP was discovered within intron 8 of myeloid ecotropic viral integration site 1 (*MEIS1;* Winkelmann et al., 2007b). Although intronic elements can regulate genes other than the host gene (Smemo et al., 2014), this genomic region harbours only one protein coding gene, encoding the MEIS1 homeobox transcription factor. A recent study found that the RLS-associated region in intron 8 forms direct chromatin interactions solely with the *MEIS1* promoter (Lam et al., 2022), demonstrating that *MEIS1* is the regulatory target of this region. The RLS risk haplotype in *MEIS1* is thought to perturb gene expression, resulting in reduced *MEIS1* expression, observed in post-mortem tissue biopsies of the thalamus, as well as lymphoblastoid cell lines from homozygous carriers (Xiong et al., 2009). Moreover, *MEIS1* knockdown in neural cells was found to affect iron homeostasis in vitro (Catoire et al., 2011).

Genome-wide SNP arrays used in GWASs are currently limited to common variants, with a minor allele frequency (MAF) of >5%, thereby omitting single nucleotide variants (SNVs) with lower frequency (Gibson, 2012; Maher, 2008). This partly explains why many loci found by segregation analysis in RLS-affected families were not identified in RLS-GWAS (Schormair et al., 2017; Winkelmann et al., 2007a). In addition to the common RLS-associated variants discovered by GWAS, low-frequency SNVs play a role in conferring RLS risk. Investigation of SNVs with a MAF below 1% in exons of MEIS1 showed a high prevalence of loss-of-function variants in RLS patients, as well as an enrichment of rare variants in the 5’ UTR, likely affecting mRNA stability (Schulte et al., 2014).

Aiming to pinpoint causal variants within the RLS-associated region in intron 8 of *MEIS1*, highly conserved non-coding regions (HCNR) were identified, containing, variants enriched in RLS patients (Spieler et al., 2014). One of these regions, HCNR 617, demonstrated reproducible enhancer activity in a mouse LacZ-reporter assay. This activity was highly specific to the ganglionic eminences (GE, Figure 1.3.1F,G), an area of high MEIS1 expression and the main source of interneurons and striatal projection neurons in the developing forebrain (Rubenstein and Rakic, 2013). Activity of HCNR 617 was reduced when it contained an RLS-associated risk variant,

compared to the protective allele. In vitro, the risk variant increases DNA-binding affinity of the CREB1 transcription factor to HCNR 617, reducing its activity (Spieler et al., 2014).

Together, these studies imply that regional reduction or loss of function in MEIS1 within the ganglionic eminences can perturb developmental processes and thereby alter neuronal activity, connectivity, or function in the forebrain, resulting in a vulnerability or predisposition to RLS. Disruption of developmental processes in RLS is supported by an enrichment of neurogenesis-associated genes in and around RLS-associated loci, suggesting that RLS is at least in part a neurodevelopmental disorder (Schormair et al., 2017).

Despite MEIS1 being a widely expressed pleiotropic developmental transcription factor, RLS patients with the *MEIS1* risk haplotype do not display any developmental comorbidities. Current understanding of the neural specificity of the *MEIS1* risk haplotype is limited and requires close investigation of the molecular and cellular functions of MEIS1 in neural cells, as well as insight into spatiotemporal expression patterns in the developing and adult brain.

1.3 Embryonic forebrain development

In the mouse brain, telencephalic inhibitory neurons originate in the ganglionic eminences (GE) during the second half of embryonic development (Marin and Rubenstein, 2001). Their progenitors emerge from highly proliferative stem cells in the ventricular zone (VZ) of the GEs and preoptic area (POA), adjacent to the lateral ventricles. These cells initially divide symmetrically, generating a growing pool of radial glia cells (RG) until embryonic day ten (E10; Noctor et al., 2004). Starting at E11, RG can also divide asymmetrically, one progeny cell retaining RG identity and remaining proliferative in the VZ, while the other cell migrates radially away from the ventricle. The latter cell undergoes more rapid divisions in the subventricular zone (SVZ) before becoming post-mitotic. Neuronal migration is influenced by chemical cues, directing cells along diverse migratory routes (Marin, 2013). Interneurons originating from the POA, MGE and CGE either migrate into the striatum, or tangentially in a dorsal direction via a superficial (lateral) or deep (medial) migratory route, followed by terminal differentiation and inward migration to their final positions

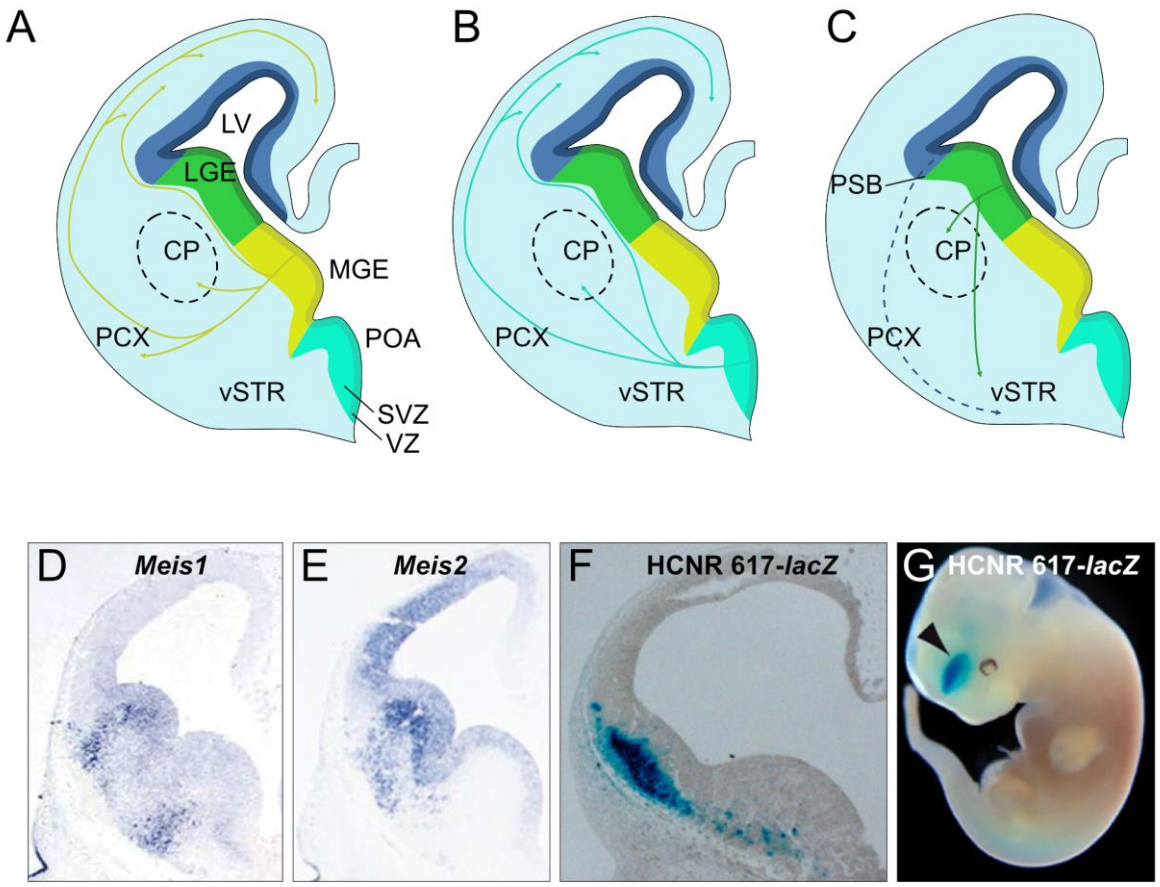

Figure 1.3.1: Migration of neurons originating in the ganglionic eminences of the developing forebrain. A-C: migration paths originating in MGE (yellow), POA (teal) and LGE (green), respectively. Pallial VZ/SVZ indicated in blue. Schematic coronal sections were adapted from Marin and Rubenstein (2001) and Rubenstein and Campbell (2013). D&E: Coronal sections of in-situ hybridisation against Meis1 & Meis2 transcripts at E12.5 (Toresson et al., 2000). F & G: LacZ staining of HCNR 617 enhancer activity at E12.5, coronal section and whole mount, respectively (Spieler et al., 2014). LV: lateral ventricle, CP: caudoputamen, VZ: ventricular zone, SVZ: subventricular zone, PCX: piriform cortex, vSTR: ventral striatum, PSB: pallial-subpallial border.

in specific layers of the cortex (Figure 1.3.1A-C). Interneuron type and spatial position are determined by a combination of external signals and apical progenitor identity, which progresses between mid- and late embryogenesis (Telley et al., 2019). In contrast to MGE and CGE, the LGE generates striatal medium spiny projection neurons (MSN), olfactory bulb interneurons and interneurons of ventral basal ganglia formations (Wichterle et al., 2001). The lateral cortical stream (LCS) originates at the pallial-subpallial border in the dorsal LGE, leading along the lateral caudoputamen to the piriform cortex and ventral striatum (vSTR), which consists of the olfactory tubercle and nucleus accumbens (Figure 1.3.1C), containing a mixture of excitatory and inhibitory neurons (Carney et al., 2006). Expression of *Meis1* transcript and MEIS1 protein in the developing mouse embryo forebrain have been described in the VZ, SVZ, prospective striatum and cortical areas adjacent to medial and lateral GE

(Barber et al., 2013; Toresson et al., 2000), which overlap with the activity of the RLS-associated HCNR 617 (Figure 1.3.1D&F, Spieler et al., 2014).

The *MEIS2* gene, a close homolog of *MEIS1*, has also been found to be associated with RLS (Schormair et al., 2017). MEIS1 and MEIS2 proteins share a high sequence homology of over 85% (Oulad-Abdelghani et al., 1997), and their expression patterns in the developing forebrain overlap. MEIS proteins have proven the ability to partly compensate for the loss of either homologue (Antosova et al., 2016; Lai et al., 2017; Machon et al., 2015, Dupacova et al., 2021). Thus, wherever possible, I have addressed both MEIS1 and MEIS2 in this thesis.

Meis2 is expressed in the pallial and subpallial VZ, the SVZ and marginal zone of the LGE, but not of the MGE (Figure 1.3.1E). Moreover, *Meis2* expression is found throughout the pallial VZ and SVZ. In later developmental stages, MEIS2 continues to be expressed throughout the cortex and striatum, while MEIS1 expressing cells are found in the ventral striatum, piriform cortex and medial septum (Toresson et al., 2000). Given the numerous migration routes intersecting with areas of high MEIS1 expression in the striatum and prospective piriform cortex, identification of cell types and their terminal positions in the brain are crucial for understanding the contribution of MEIS1 to RLS. Recent studies have shown versatile, tissue-specific roles of MEIS proteins in the retina, olfactory bulb, cerebellum, midbrain and sympathetic neurons as well as the spinal cord (Agoston and Schulte, 2009; Agoston et al., 2014; Bouilloux et al., 2016; Marcos et al., 2015; Owa et al., 2018).

1.4 MEIS proteins regulate developmental processes by interacting with various binding partners

MEIS homeodomain transcription factors regulate developmental processes by driving proliferation in progenitors of the olfactory epithelium and retina, leukemia and neuroblastoma (Bessa et al., 2008; Heine et al., 2008; Lin et al., 2019; Moskow et al., 1995; Patel et al., 2016; Spieker et al., 2001), or by initiating cell cycle exit and differentiation in neuronal and cardiac precursors (Agoston et al., 2014; Hau et al., 2017; Mahmoud et al., 2013; Owa et al., 2018; Tucker et al., 2010).

MEIS are structurally conserved within the protein family (MEIS1/2/3), as well as among vertebrates (Longobardi et al., 2014). This conservation is especially pronounced for the two N-terminal protein interaction domains and the homeodomain, required for DNA binding and nuclear localization, while the C-

terminal transcriptional activation domain is more variable (Figure 1.4.1A, Chang et al., 1997; Huang et al., 2005; Shen et al., 1997). Target specificity has been observed for different MEIS isoforms (Gross et al., 2018; Maeda et al., 2001), but is considered to be mainly directed by interaction with varying proteins, which has been described in detail for members of the PBX and HOX families (Blasi et al., 2017). Direct complex formation of MEIS with PBX is facilitated by a set of matching, N-terminal domains which allows heterodimerization, modulating DNA binding affinity, transcriptional activation, nuclear import and export, and likely protein stability (Berthelsen et al., 1999; Chang et al., 1997; Hyman-Walsh et al., 2010; Longobardi et al., 2014).

MEIS1 and MEIS2 share the same hexameric DNA binding motif, TGACAG (Figure 1.4.1B), which is conserved between vertebrates and *Drosophila* (Shen et al., 1997 Chang et al., 1997 Ferretti et al., 2000). Further binding motifs of MEIS have been described when acting as a heterodimer with PBX, binding the TGATTGACAG sequence (Figure 1.4.1B, Chang et al., 1997; Knoepfler et al., 1997), or forming heterodimeric complexes with AbdB-like HOX proteins at TGACAGTTTTAYGA sequences (Shen et al., 1997). MEIS can also form trimeric complexes, by interacting with PBX-HOX dimers, binding the TGATNNAT motif (Berthelsen et al., 1999; Ferretti et al., 2000; Shanmugam et al., 1999). In this configuration, MEIS can bind a nearby hexameric TGACAG motif, or interact with PBX without DNA binding (Figure 1.4.1C, D; Shanmugam et al., 1999). In the mouse embryonic trunk, TGATNNAT was discovered to be the most frequent motif within MEIS binding sites, highlighting the

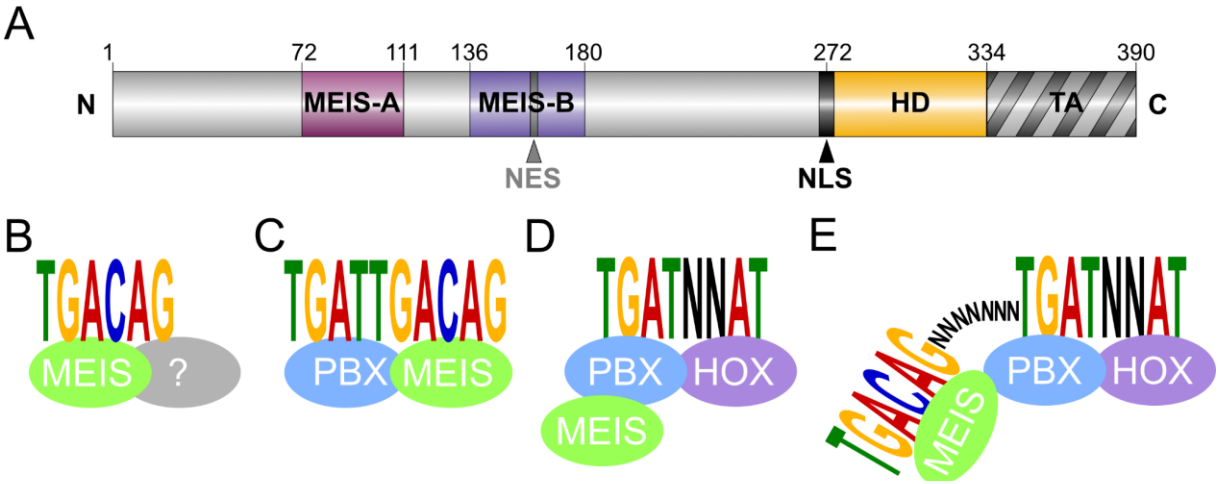

Figure 1.4.1: MEIS Protein structure and interaction with PBX & HOX. A) Schematic representation of human MEIS1 isoform A. Two N-terminal protein interaction domains, MEIS-A and MEIS-B, allow dimerization with PBX proteins. HD: homeodomain, TA: transactivation domain. NES: nuclear export signal, NLS: nuclear localisation signal. Amino acid positions of domains are indicated above. B-E) MEIS protein complexes have affinity for specific DNA motifs.

functional importance of MEIS-PBX-HOX interaction in this tissue (Penkov et al., 2013). In the anterior brain however, absence of HOX proteins (Duboule, 2007) suggests the formation of structurally different regulatory complexes involving MEIS proteins. Several MEIS interaction partners in the mouse and chick brain have already been described, including transcription factors PAX3, PAX6, PAX7, OTX4, PBX1, DLX1 and DLX2 (Agoston and Schulte, 2009; Agoston et al., 2012; Agoston et al., 2014; Hau et al., 2017). This variety mirrors the varying roles described for MEIS proteins in different parts of the brain (Schulte and Geerts, 2019) and highlights the necessity of cell-type specific analyses.

1.5 Aim and research objectives

Genome-wide association studies (GWAS) have implicated neurodevelopment in RLS, and identified an intronic region within *MEIS1* as the strongest genetic risk factor. In this region, a disease-associated SNP proved to reduce the activity of forebrain-specific enhancer HCNR 617, presumably leading to a reduction in *MEIS1* expression. Both HCNR 617 and *Meis1,* respectively display strongest activity and expression in embryonic stages in the prospective basal ganglia, which show functional aberrations in RLS patients.

The aim of this work was to characterize MEIS1 expressing cell types in the developing forebrain, using immunofluorescence and in-situ hybridization and thus to determine cells co-expressing MEIS1 and neural marker genes in mouse embryo brains. Furthermore, MEIS binding sites were addressed by chromatin-immunoprecipitation sequencing (ChIP-seq) and mRNA knockdown in cultured human neural progenitors. To investigate the prevalence of RLS-associated regions among MEIS targets, MEIS binding sites were integrated with existing GWAS data. Finally, to understand the effects of MEIS1 deficiency, I established knockout lines of human induced pluripotent stem cells (iPSC) and applied 2D and 3D in vitro differentiation techniques on hNSC and iPSC.

2 Results

2.1 Histological studies identify and characterize populations of MEIS1 expressing cells in the embryonic mouse brain

MEIS1 protein expression during embryonic development was examined using the previously established transgenic mouse line C57BL/6N-Meis1^{em1Bcca} (Xiang et al., 2017). The line expresses the GFP-P2A-HA-MEIS1 construct, containing a hemagglutinin (HA)-MEIS1 fusion protein in the endogenous *Meis1* locus. As GFP fluorescence proved insufficient for reliable detection (data not shown), coronal sections of mouse embryos at post-conceptual day 14 (E14.5) were immunostained for MEIS1 with an antibody directed against the HA-tag, allowing clear distinction of MEIS1 from the structurally homologous MEIS2 protein, which is otherwise not possible with anti-MEIS1 antibodies.

Strongest Meis1 expression was found throughout the piriform cortex (PCX), forming a caudo-rostral gradient (Figure 2.1.1). Expression extended dorsally into the insular cortex and ventrally throughout the ventral striatum (vSTR) into the medial septum (Figure 2.1.1B, C), with a distinct population in the nucleus accumbens in the rostral forebrain (Figure 2.1.1C), while caudal sections depicted expression up to the prospective amygdalar cortex (Figure 2.1.1E). Lower MEIS1 protein expression was detected in the caudoputamen (CPu, Figure 2.1.1C). Furthermore, MEIS1 expressing cells were detected in the hypothalamus, ventral to the thalamocortical tract (Figure 2.1.1E), while expression was detected neither in the hippocampus, nor in the caudal diencephalon (Figure 2.1.1F). In addition, in-situ hybridisation (ISH) was performed for *Meis1* and *Meis2* transcripts in a wild type mouse embryo at E14.5. *Meis1* ISH signal mostly overlapped with protein expression patterns, also showing strongest expression in the PCX and vSTR (Figure 2.1.1G). Furthermore, distinct *Meis1* mRNA signal was detected in the SVZ of the LGE, extending as far as the VZ of the LGE, revealing expression which was not detected at the protein level. No distinguishable signal was found in the VZ/SVZ of the MGE.

In the adult mouse forebrain, patterns of *Meis1* expressing cells are reminiscent of those in the embryonic forebrain, although in lower numbers: *Meis1* mRNA expression is found in the piriform cortex, the olfactory tubercle, lateral caudoputamen, pallidum, and medial septum (Supplementary Figure 1A&B, Allen Brain Atlas at P56).

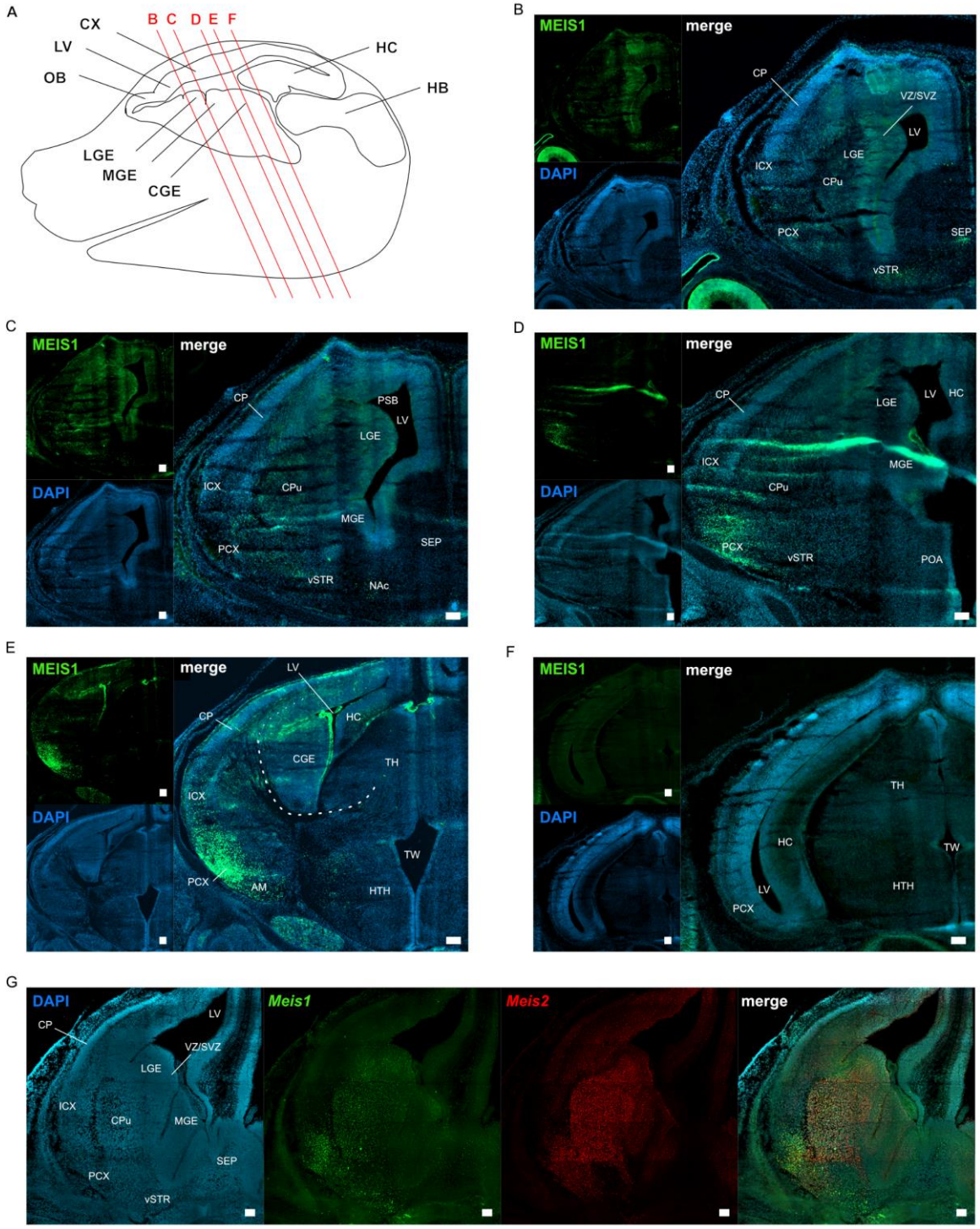

Figure 2.1.1: Immunostaining of MEIS1 in the developing mouse brain. A) overview of coronal section planes. B-F) coronal sections of C57BL/6N-Meis1^{em1Bcca} E14.5 mouse embryos, stained against the HA-MEIS1 fusion protein. E) dotted line indicates thalamocortical tract. G) In-situ hybridization against *Meis1* and *Meis2* mRNA in a wt mouse embryo at E14.5. Scale bars = 100 µm. CGE: caudal ganglionic eminence, CX: cortex, HB: hindbrain, HC: hippocampus, HTH: hypothalamus, ICX: insular cortex, LGE: lateral ganglionic eminence, LV: lateral ventricle, LSN: lateral septal nucleus, MGE: medial ganglionic eminence, OB: olfactory bulb, OT: olfactory tubercle, PCX: piriform cortex, STR: striatum, TH: thalamus, TW: third ventricle.

MEIS2 protein was co-expressed in the majority of MEIS1^{+} cells in the PCX, isocortex, caudoputamen and nucleus accumbens (Figure 2.1.2A-A'''). Furthermore,

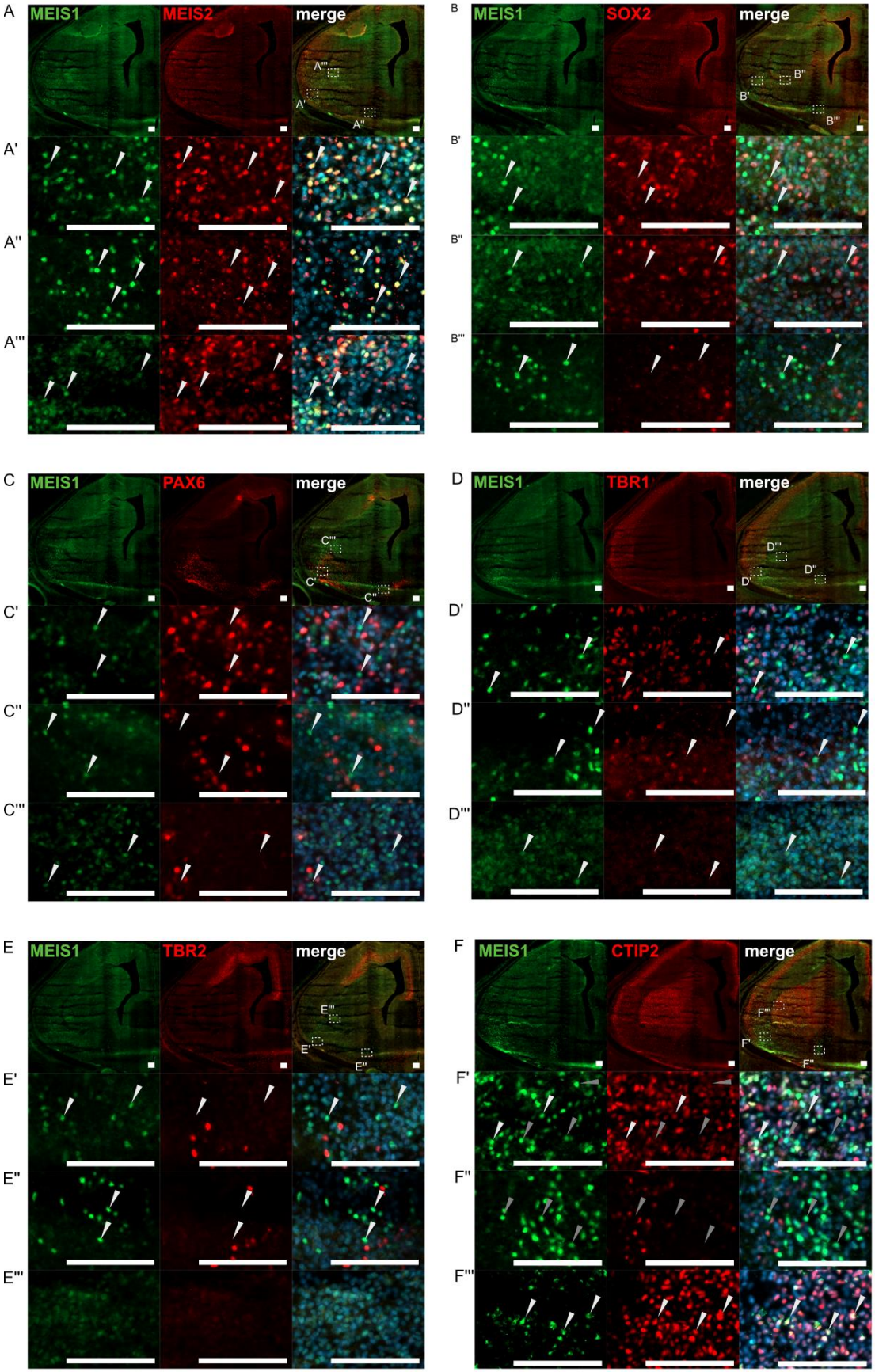

Figure 2.1.2: Co-immunostainings of MEIS1 with neural markers. Coronal sections of C57BL/6N-Meis1^{em1Bcca} E14.5 mouse embryos. Cells co-expressing MEIS1 and another neural marker appear yellow/orange. A'-E'''). Detail images of PCX (X'), vSTR (X'') and dSTR (X'''). White arrowheads mark cells expressing MEIS1. F'-F''') white arrowheads mark MEIS1^{+}/CTIP2^{+}, grey arrowheads indicate MEIS1^{+}/CTIP2^{-} cells. Scale bars = 100 µm

Meis2 transcripts were expressed throughout the LGE, and in the cortex (Figure 2.1.1G). To identify the neural cell types expressing MEIS1, co-immunostainings were performed with antibodies against the neural marker proteins SOX2, PAX6, TBR1, TBR2 (EOMES) and CTIP2 (BCL11B). Expression patterns of MEIS1 and the progenitor cell marker SOX2 overlapped in the CPu, PCX and vSTR, but co-expression was not observed (Figure 2.1.2B-B''). Likewise, no MEIS1$^+$ cells were detected that co-express either PAX6, TBR1 or TBR2 which mark excitatory progenitors, precursors and neurons, respectively (Figure 2.1.2C-E; Englund et al., 2005). Furthermore, I investigated co-expression with CTIP2 (BCL11B), a marker of striatal projection neurons which is also expressed in cortical inter- and projection neurons (Arlotta et al., 2008; Nikouei et al., 2016). Co-expression of MEIS1 with CTIP2 varied between brain regions: while all MEIS1$^+$ cells in the CPu co-expressed CTIP2 (Figure 2.1.2F&F'''), only a subpopulation of MEIS1$^+$ cells were positive for CTIP2 in the dorsal PCX (Figure 2.1.2F'), gradually declining in a ventral direction, with no co-expression detected in the vSTR or prospective nucleus accumbens (Figure 2.1.2F-F'').

2.2 MEIS in neural differentiation

As the functions of MEIS are highly tissue-specific, even among different neural cell types, defining the roles of MEIS1 in neural differentiation is imperative to understanding implications for RLS. Therefore, different in vitro models of neural differentiation were employed.

2.2.1 Human cerebral organoids as a model to study the effect of MEIS1 in forebrain differentiation

Brain organoids model early stages of brain development, and region-specific methods generate a variety of neuronal subtypes while mirroring basic structures in the brain (Lancaster et al., 2013; Lancaster and Knoblich, 2014b; Quadrato et al., 2017).

I generated ventralized organoids (Bagley et al., 2017; Lancaster and Knoblich, 2014a) from human induced pluripotent stem cells (iPSC) to assess their suitability in modelling the role of MEIS1 during forebrain development and performed histological analysis after 32 days in culture. Immunostaining revealed the presence of fluid-filled, ventricle-like cavities encircled by SOX2$^+$ progenitor cells, reminiscent of the lateral

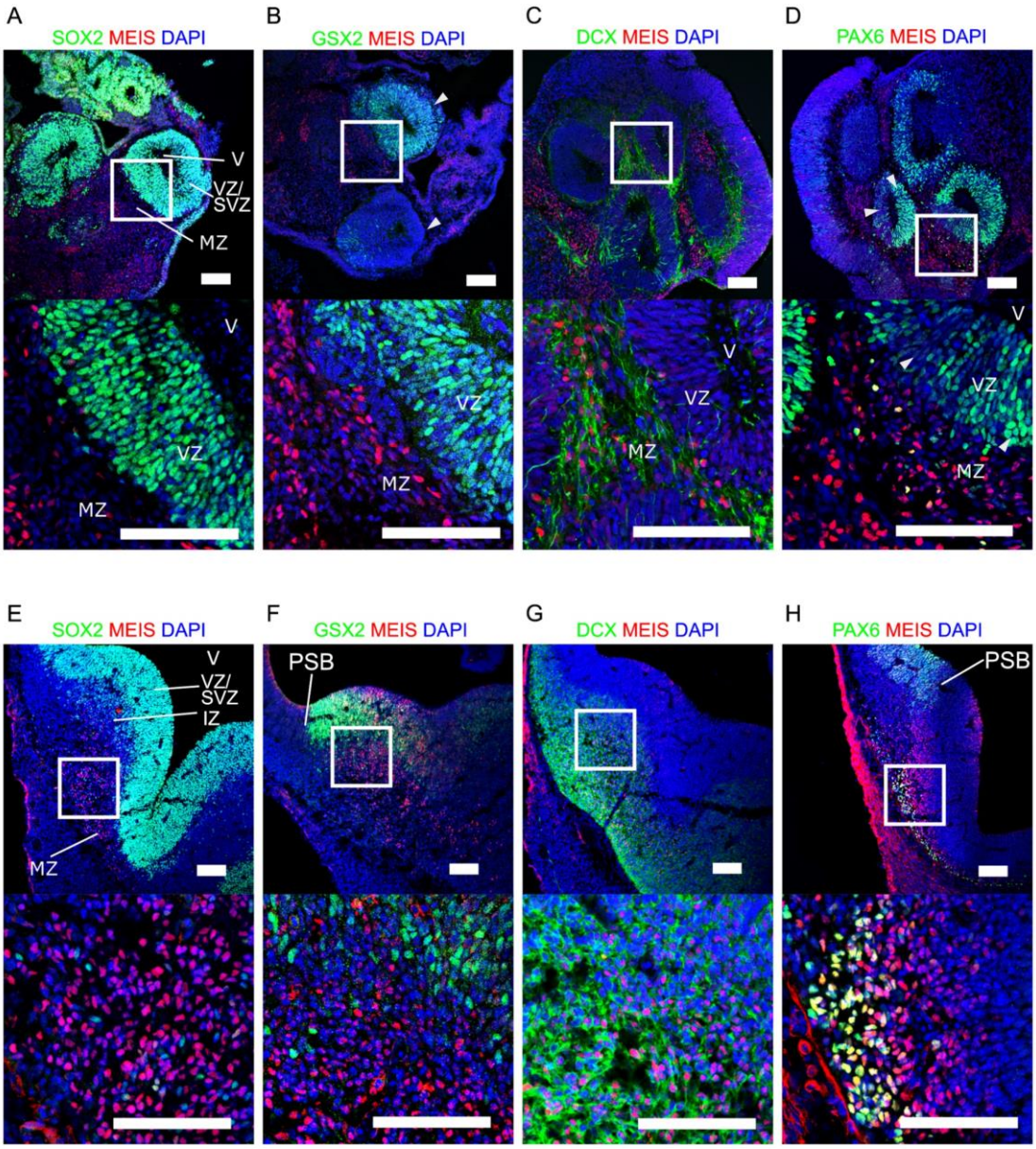

Figure 2.2.1: Cerebral organoids generated from human iPS cells mirror organization and cell types at the lateral ventricles during embryogenesis. A-D) 32-day old organoids and E-H) coronal forebrain sections of E12.5 embryos were stained against neural markers. Arrowheads indicate pallial-type and subpallial-type cells in the VZ/SVZ. MZ: marginal zone, PSB: pallial-subpallial border, SVZ: subventricular zone,V: ventricle, VZ: ventricular zone, Scale bars = 100 µm.

ventricles and surrounding ventricular/subventricular zones (VZ/SVZ) in the embryonic mouse forebrain (Figure 2.2.1A&E). Here, expression of PAX6 and GSX2 mark the pallial and sub-pallial part of the VZ/SVZ, respectively (Figure 2.2.1F&H). In organoids, part of the VZ/SVZ-like structures expressed GSX2, while other areas in the VZ/SVZ stained positive for PAX6, indicating a mixture of pallial- and subpallial-like progenitors (Figure 2.2.1B&D). In the mouse brain, after radial migration away from the lateral ventricle, progenitors become post-mitotic and differentiate to doublecortin-expressing (DCX^+), immature neurons (Figure 2.2.1G & section 1.3),

which was also reproduced in organoids, evident by DCX$^+$ cells surrounding VZ-like structures (Figure 2.2.1C).

By staining with a pan-MEIS antibody, MEIS-expressing cells in organoids were found mainly overlapping with DCX$^+$ neurons (Figure 2.2.1C&G), while partial co-expression with PAX6 was observed distal to the VZ/SVZ (Figure 2.2.1D&H). In contrast, while low MEIS expression in VZ/SVZ progenitors of the LGE was found in the mouse (Figure 2.2.1F&H), expression in VZ/SVZ-like structure of organoids could not be detected.

2.2.2 *MEIS1* Knockout results in increased *MEIS2* mRNA expression

To investigate the effect of MEIS1 depletion throughout neural differentiation in human cells, frame-shift deletions within exon 3 of the *MEIS1* gene were introduced in induced pluripotent stem cells (iPSC) using CRISPR/Cas9 genome editing (Jinek et al., 2012), to be used in future in vitro differentiation experiments. Expanded from single clones, four complete *MEIS1* knockouts carrying homozygous or compound-heterozygous frame-shift mutations were identified by Sanger sequencing. As iPSC do not express MEIS1, its expression was induced by retinoic acid (Mercader et al., 2000) to verify the knockout on the protein level. Western blotting revealed bands at 50 kDa and 60 kDa after induction in WT iPSC, corresponding to the isoforms MEIS1a and MEIS1b (Figure 2.2.2A). A third, unknown band was detected at 45 kDa. MEIS2 protein levels were not affected by knockout of MEIS1.

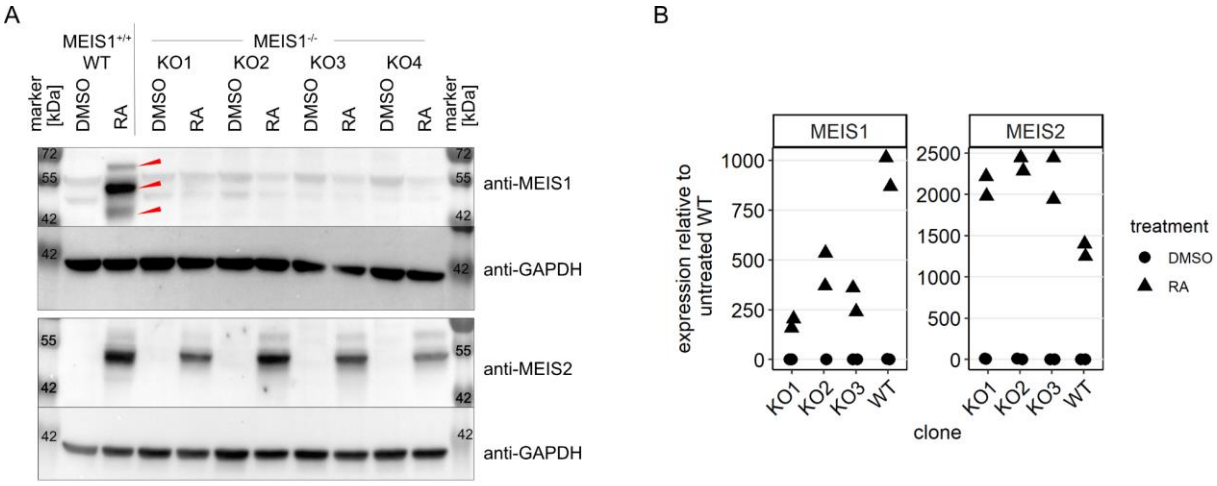

Figure 2.2.2: MEIS1 expression in RA-treated iPS cells. A) western blot analysis of MEIS1 and MEIS2 protein expression in WT and *MEIS1*$^{-/-}$ iPSC after treatment with 10 µM RA for four days, with DMSO used as negative control. Arrowheads indicate three bands appearing after RA induction. GAPDH expression was used as loading control. B) *MEIS1* and *MEIS2* mRNA expression of *MEIS1*$^{-/-}$ clones 1-3 and WT clone after RA treatment determined by qPCR. Values are relative to expression in the untreated (DMSO) wild type control. RA: retinoic acid. DMSO: di-methyl sulfoxide

qPCR found *MEIS1* mRNA expression in MEIS1$^{-/-}$ cells reduced by 50-75%, likely resulting from partial nonsense-mediated mRNA decay. In contrast, mRNA expression of MEIS2 was increased 1.3-1.8-fold (Figure 2.2.2B), which may point towards a compensation of MEIS1-loss by MEIS2.

2.3 Human neural stem cells as model system for neural development

Impaired or aberrant expression of *MEIS1* during neural development could cause perturbations that manifest only in later stages of life. Appropriate model systems are therefore required to reveal its connection to RLS.

Neural development in the brain is regulated by a multitude of transcription factors, including MEIS1 and MEIS2. To investigate their potential roles in RLS, we employed a model system of human neural stem cells (hNSC), multipotent immature neural cells capable of stable expansion and differentiation in vitro.

We observed that these cells can be expanded up to 20 passages, without displaying changes in morphology or growth rate (Figure 2.3.1A-D). Immunostaining revealed nuclear signal for MEIS proteins in hNSC (Figure 2.3.1H). Furthermore, the cells stained positive for the neural stem cell markers SOX2 and nestin (NES; Figure 2.3.1E&F), while being unreactive to antibodies directed against the pluripotent stem cell marker OCT4 (data not shown). In addition, expression of PAX6 protein was detected, which is found abundantly in neural progenitors of the developing telencephalon and in neuroepithelial cells (Osumi et al., 2008). Whole transcriptome sequencing performed at the ING prior to this study confirmed the expression pattern observed by immunostainings, showing high mRNA expression of genes encoding *SOX2* and nestin (*NES*), and low expression of *MEIS1, MEIS2* and *PAX6* (Figure 2.3.1I). Comparison of global gene expression of the neural proliferation markers *SOX2*, *VIM*, *NES* and the regional markers *FGF8*, *FOXG1*, *DLX1*, *DLX2*, and *GSX1* with their homologs in the Mouse Organogenesis Cell Atlas (MOCA, Cao et al., 2019) showed hNSC most closely resemble cells assigned to the classes radial glia, neural tube and neural progenitor (data not shown). In conclusion, hNSC constitute a suitable model for immature, proliferative neural progenitor cells, allowing investigation of basic MEIS functions in a human neural context, and were therefore used in chromatin immunoprecipitiation-sequencing (ChIP-seq) and gene knockdown experiments.

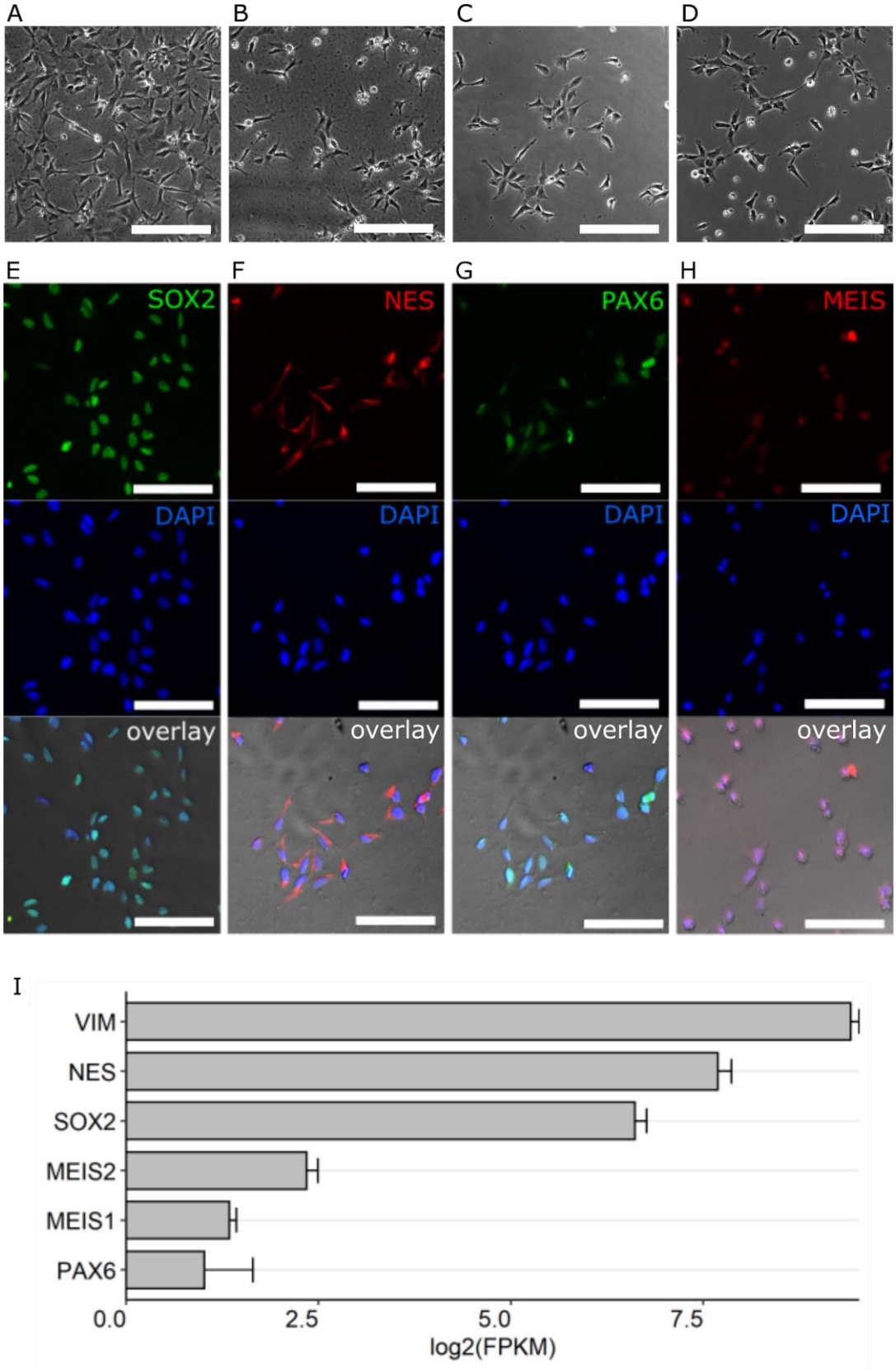

Figure 2.3.1 Expression of neural markers in hNSC. A)-D): bright field images of hNSC at different passages show unchanged morphology A,B= P6, C,D= P20. E)-H) Immunostaining against neural marker genes in hNSC. The cells display strong fluorescent signal when stained with antibodies against SOX2 and Nestin (NES), and weaker signal from PAX6 and MEIS antibodies. Overlay of signal from antibody, DAPI and bright field images. Scale bar = 100 µm. I) comparison of gene expression for selected neural marker genes mirror results of immunostainings, with high expression of nestin (NES) and SOX2, and medium to low expression for MEIS1, MEIS2 and PAX6. Mean FPKM of four replicates, error bars represent standard error of the mean.

2.4 Partial mRNA-knockdown of MEIS1 and MEIS2 in hNSC and NPC does not affect gene expression of selected MEIS targets

To identify genes controlled directly and indirectly by MEIS1 and MEIS2, mRNA knockdown via RNA-interference (RNAi; Fire et al., 1998) was performed in human neural stem cells (hNSC). A previously developed microRNA (miRNA) scaffold was used (Fellmann et al., 2013), expressing pri-miRNAs, which are processed to short hairpin RNA (shRNA) by the cells' internal miRNA machinery. These "shRNAmir" constructs have been shown to facilitate efficient depletion of mRNA while minimizing off-target effects, which were often reported in connection to traditional siRNA and shRNA constructs (Fellmann et al., 2013; Rao et al., 2009).

Scrambled shRNAmir, or shRNAmir targeting *PPP1R12C* mRNA served as negative controls. The *PPP1R12C* gene is located within the adeno-associated virus integration site 1 (*AAVS1*), also known as safe harbour locus, that has frequently been used for stable gene integration without showing adverse effects (Oceguera-Yanez et al., 2016). shRNAmir constructs directed against *MEIS1* or *MEIS2* proved efficient when transfected in HEK293T by lipofection, reducing average expression by 50% and 70%, respectively (Figure 2.4.2A). *MEIS1*-shRNAmir did not affect the expression of *MEIS2*, and vice versa, proving specificity. hNSC served as a model system to investigate the functions of MEIS proteins during neural development (see section 2.3). Transfection approaches with lipofectamine and electroporation proved challenging, while lentiviral transduction was highly efficient. Thus, in vitro cultured cells were transduced with lentivirus, expressing *PPP1R12C*-, *MEIS1*- or *MEIS2*-

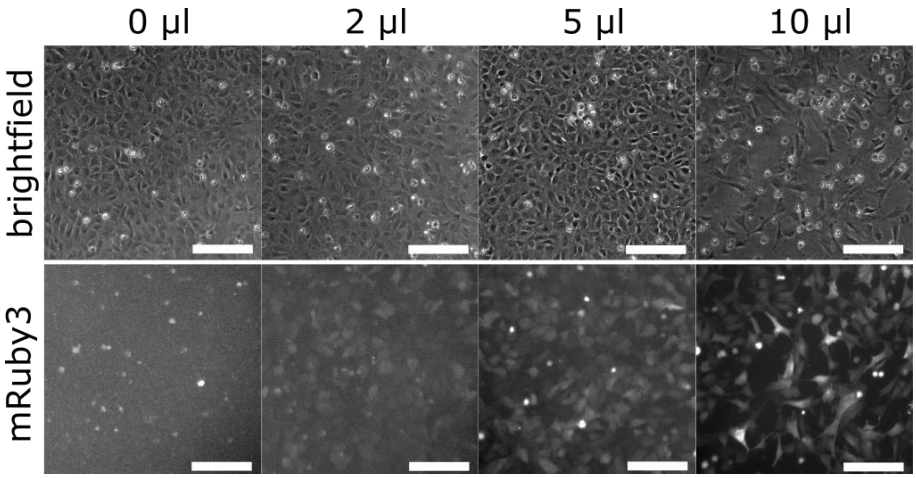

Figure 2.4.1 Lentiviral transduction efficiency of PPP1R12C shRNAmir vector in hNSC. Different volumes of virus-containing supernatant were tested on hNSC. Top: bright field images 72 h after infection. Bottom: fluorescence images of the mRuby3 reporter. Scale bars 100 µm.

transcript-specific shRNAmir, along with the mRuby3 fluorescent reporter (Bajar et al., 2016). Gene expression was evaluated by quantitative real-time PCR (qPCR) or western blot. The optimal lentiviral transduction titer of hNSC was determined based on fluorescence of mRuby3 and cell density relative to untransduced cells, using a vector containing control shRNAmir (Figure 2.4.1). High lentiviral transduction efficiency in hNSC (>90%) was confirmed by fluorescence microscopy. As expected, mRNA knockdown efficiency was correlated with the amount of virus (Figure 2.4.2C). 5 µl of concentrated virus-containing supernatant were subsequently used to infect cells, as 10 µl supernatant lead to increased apoptosis and reduced density of cells.
SOX2, *NES* and *PAX6* were shown to be putative target genes of MEIS proteins in hNSC (section 2.6). These genes are expressed throughout embryonic development of the nervous system, primarily in stem and progenitor states. Furthermore, previous studies revealed the *Pax6* gene and PAX6 protein as direct target and interaction partner of MEIS in the developing mouse central nervous system (Antosova et al., 2016; Zhang et al., 2002; Owa et al., 2018). *SOX2*, *NES* and *PAX6* were chosen for gene expression analysis after knockdown of *MEIS1* and *MEIS2*. In addition to hNSC, iPS-derived neural progenitor cells (NPC) were transduced with lentivirus. In hNSC and NPC cell lines, knockdown reduced average *MEIS1*-expression by 34% and 26%, respectively, which was only statistically significant in hNSC (Wilcoxon rank-sum test, adjusted P = 0.325, Figure 2.4.2E, F). MEIS2-knockdown resulted in significant reduction of *MEIS2* in hNSC (44%) and NPC (47%; Figure 2.4.2B, D). However, none of the putative MEIS-targets *PAX6*, *NES* or *SOX2* were significantly affected by *MEIS1* or *MEIS2* knockdown, in either cell line. To increase knockdown efficiency, new shRNAmir constructs against MEIS1 were designed, and showed improved mRNA knockdown efficiency in hNSC (Figure 2.4.2E). Despite increasing MEIS1 knockdown efficiency from 20% to 60%, *PAX6* and *SOX2* expression remained unaffected after transduction with the new shRNAmir construct (Figure 2.4.2F).

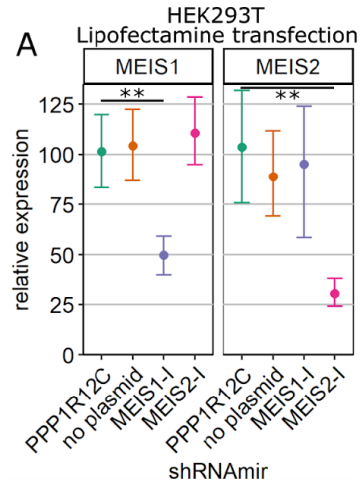
A
HEK293T
Lipofectamine transfection
MEIS1
MEIS2
relative expression
PPP1R12C
no plasmid
MEIS1-I
MEIS2-I
shRNAmir

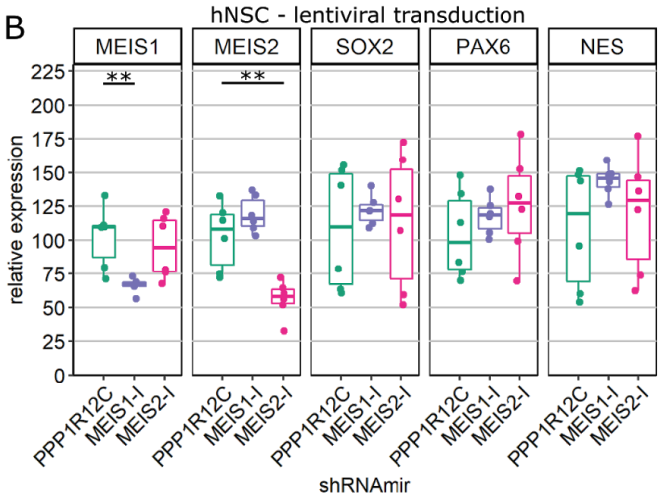
B
hNSC - lentiviral transduction
MEIS1
MEIS2
SOX2
PAX6
NES
relative expression
PPP1R12C
MEIS1-I
MEIS2-I
shRNAmir

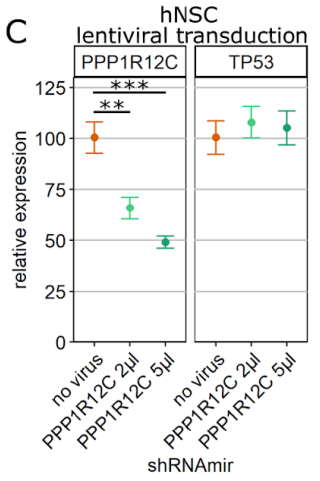
C
hNSC
lentiviral transduction
PPP1R12C
TP53
relative expression
no virus
PPP1R12C 2µl
PPP1R12C 5µl
shRNAmir

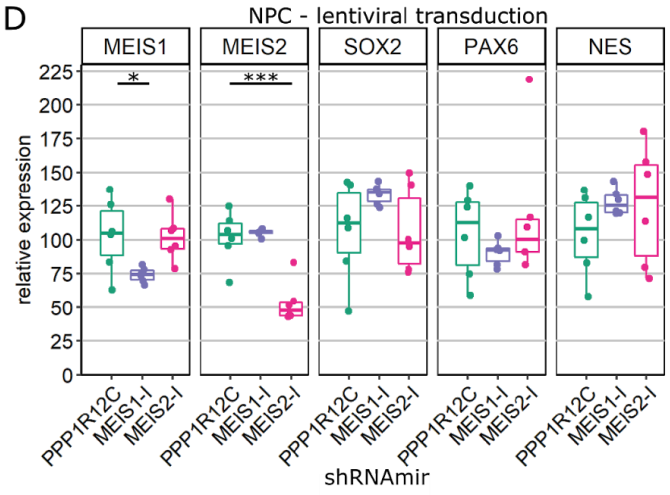
D
NPC - lentiviral transduction
MEIS1
MEIS2
SOX2
PAX6
NES
relative expression
PPP1R12C
MEIS1-I
MEIS2-I
shRNAmir

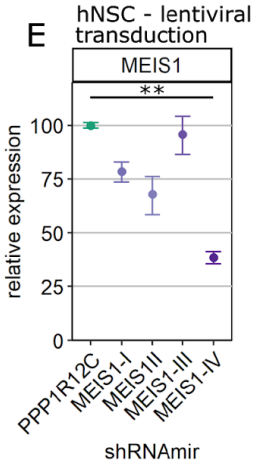
E
hNSC - lentiviral
transduction
MEIS1
relative expression
PPP1R12C
MEIS1-I
MEIS1II
MEIS1-III
MEIS1-IV
shRNAmir

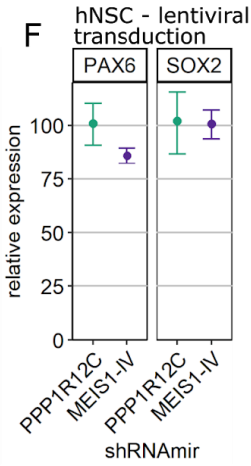
F
hNSC - lentiviral
transduction
PAX6
SOX2
relative expression
PPP1R12C
MEIS1-IV
shRNAmir

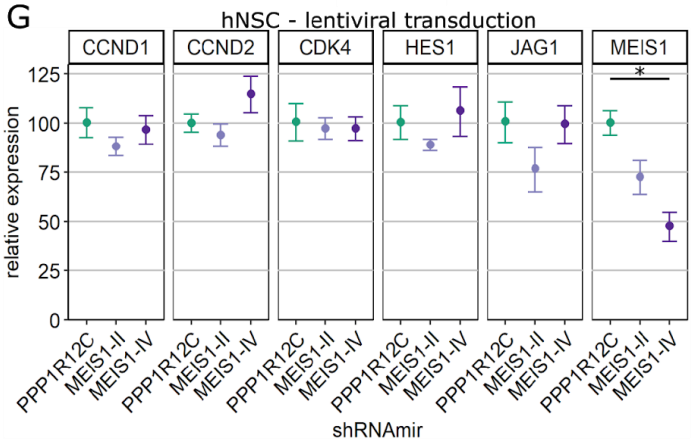
G
hNSC - lentiviral transduction
CCND1
CCND2
CDK4
HES1
JAG1
MEIS1
relative expression
PPP1R12C
MEIS1-II
MEIS1-IV
shRNAmir

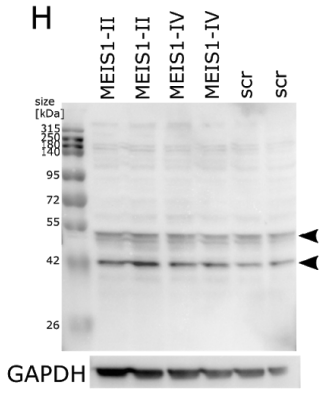
H
MEIS1-II
MEIS1-II
MEIS1-IV
MEIS1-IV
scr
scr
size
[kDa]
GAPDH

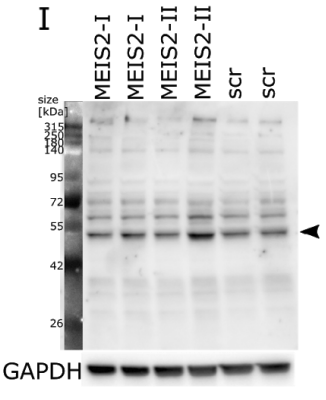
I
MEIS2-I
MEIS2-I
MEIS2-II
MEIS2-II
scr
scr
size
[kDa]
GAPDH

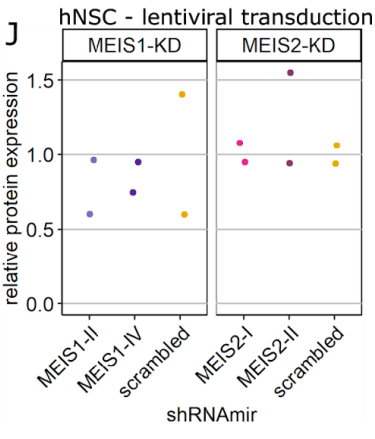
J
hNSC - lentiviral transduction
MEIS1-KD
MEIS2-KD
relative protein expression
MEIS1-II
MEIS1-IV
scrambled
MEIS2-I
MEIS2-II
scrambled
shRNAmir

Figure 2.4.2 (continued from previous page): shRNA knockdown successfully reduces *MEIS1* and MEIS2 mRNA expression, but does not affect their putative target genes in hNSC. A) shRNAmir vectors were transfected in HEK293T cells with Lipofectamine. Expression of both *MEIS1* (-50%, p=0.0051) and *MEIS2* (-70%, p=0.0036) was selectively reduced (n=4). C) Lentiviral vector carrying positive control shRNA was tested on hNSC, showing concentration-dependent mRNA depletion of the *PPP1R12C* target transcripts (2 µl virus: 34% p=0.0023, 5 µl virus: 51% p= 0.00011, n=4). Expression of the *TP53* apoptosis marker was not affected by lentiviral transduction. B) hNSC and D) NPC were infected with lentiviral vectors carrying shRNAmir against *MEIS1* or *MEIS2* mRNA. qPCR shows moderate reduction of *MEIS1* and *MEIS2* mRNA In both cell lines (hNSC – MEIS1:-34%, p=0.006, MEIS2:-44%, p=0.0028; NPC – MEIS1:-26%, p=0.047, MEIS2:-47%, p=0.00067, n=6). Expression of the putative MEIS target genes *SOX2*, *PAX6* and Nestin (*NES*) was not significantly affected by MEIS knockdown. E) test of further MEIS1-shRNAmir constructs in hNSC by lentiviral transduction. Knockdown efficiency of MEIS1-II (32%, p=0.092) and MEIS1-IV (61%, p=0.0049) prove more effective than the previously used MEIS1-I (22%, p=0.05, n=3). F) Expression of *PAX6* and *SOX2* in hNSC was not affected by MEIS1-VI knockdown (n=3). G) While *MEIS1* expression was reduced by 27% and 52% (p=0.09 & p=0.027, n=3), respectively, putative MEIS1 targets involved in cell cycle control were not affected by *MEIS1* knockdown. Gene expression was quantified by qPCR using gene-specific probes. Expression is shown relative to the mean of the control shRNAmir *PPP1R12C*. H & I) Western blots comparing H) MEIS1 and I) MEIS2 protein expression after gene knockdown. Expected band sizes for MEIS1 and MEIS2 are indicated with arrowheads. J) quantification of band intensities from western blots shows no significant differences between the shRNAmir used. To evaluate gene expression in qPCR, dCT values were compared using Welch's t-test. Significance levels for P-values: * < 0.05, ** < 0.01, *** < 0.001. CCND1: Cyclin D1, CCND2: Cyclin D2, NES: Nestin.

In mice, MEIS proteins also regulate *Jag1*, *Hes* family genes and other components of the Wnt and Notch signaling pathways (Marcos et al., 2015,) as well as Cyclin D1 (*Ccnd1*, Bessa et al., 2008; Heine et al., 2008), all of which are critically involved in cell cycle control (Bryja et al., 2017). *CCND1*, *CDK4*, *HES1* and *JAG1* were selected for analysis, as they show substantial expression in hNSC and are potential MEIS targets in this cell type (see 2.6).

While *MEIS1* knockdown using two improved shRNAmirs with higher efficiency reduced expression of *MEIS1* by 29% and 52%, respectively, expression of putative MEIS target genes was not significantly affected (Figure 2.4.2G). The effect on MEIS protein expression in response to knockdown was determined by western blot, using antibodies against MEIS1 and MEIS2 (Figure 2.4.2H&I). Despite considerable reduction of *MEIS* mRNA, protein levels of MEIS1 and MEIS2 seemed unaffected (Figure 2.4.2H).

Moderate depletion of *MEIS* mRNA of up to 60% did therefore not significantly affect known target genes, likely due to insufficient knockdown effect on MEIS protein expression.

2.5 Partial mRNA knockdown does not significantly affect proliferation of hNSC during neuronal differentiation

H9-derived human neural stem cells (hNSC, see 2.3) used in this experiment are multipotent cells, capable of differentiating towards neural and glial lineage (Shin and Vemuri, 2009). While the cells require growth factors to retain proliferative capability, differentiation can be induced by removing growth factors (EGF and FGF-b) from the

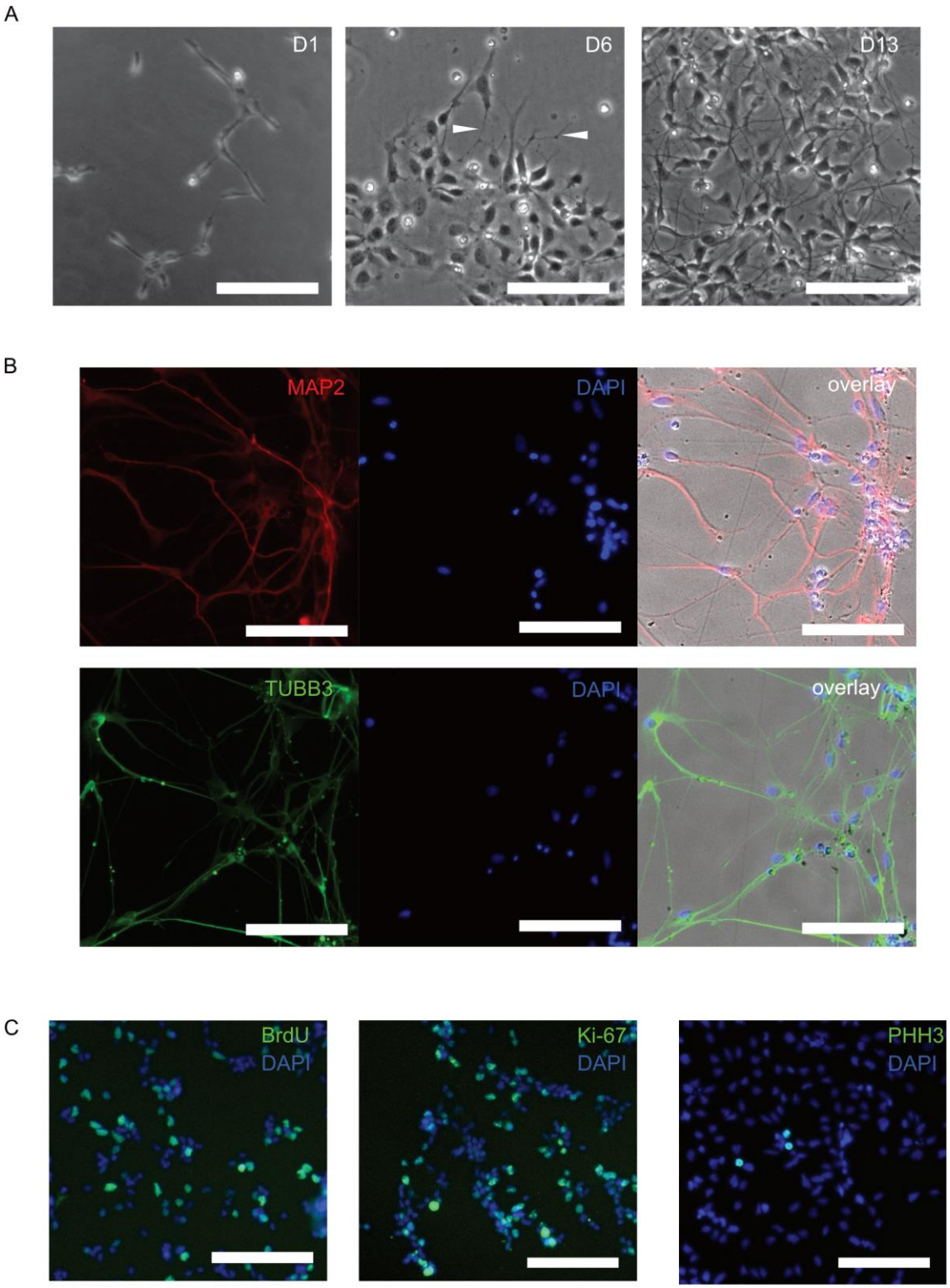

Figure 2.5.1 Growth factor withdrawal induces spontaneous neuronal differentiation in hNSC. A) Phase-contrast images of hNSC at day 1 show morphology similar to radial glia cells. After 6 days growth in media without FGF-b and EGF, cells start to form elongated cellular projections (arrowheads). After 13 days, axon-bearing neurons have formed. B) Neurons cultured for 7 weeks stain positive for neuronal markers TUBB3 (βIII-tubulin) and MAP2 Overlay includes phase contrast image. C) hNSC cultured without growth factors for 9 days and stained against proliferation markers BrdU, Ki-67and phosphohistone H3 (PHH3). Cells were treated with 10 µM BrdU 24 h before fixation. Scale bars = 100 µM.

culture medium. Upon growth factor withdrawal, cells started to show morphological changes after 6 days, displaying prolonged cellular projections (Figure 2.5.1A). By

day 13, neurons emerged, distinguishable by the appearance of neurites. After seven weeks, all cells had differentiated to neurons, staining positive for the neuronal markers MAP2 and TUBB3 (Figure 2.5.1B). In conclusion, hNSC present a suitable model to study neuronal differentiation, minimizing effects of external stimuli since they differentiate spontaneously.

To test proliferation rates after growth factor withdrawal, cells were immunostained against the proliferation markers phospho-histone H3 (PHH3) and bromodeoxyuridine (BrdU) after 9 days in growth-factor depleted culture medium. The nuclear core histone H3 is phosphorylated from late G2 phase through methaphase and is a reproducible indicator of mitosis (Kim et al., 2017). In contrast, Ki-67 is found in the nucleus during all stages of the cell cycle, only absent in G_0 in resting cells. BrdU is incorporated in the cells' DNA during replication following mitosis, and thus indicates if cells underwent division since the addition of BrdU to growth media (Nowakowski et al., 1989). After 9 days in growth-factor depleted medium, 36% of cells stained positive for BrdU, indicating cell division in the previous 24h (Figure 2.5.2). 42% stained positive for Ki-67 and <1% of cells stained positive for PHH3. However, fluorescence intensity of Ki-67 staining was close to background intensity, complicating analysis, and was therefore not evaluated further.

While mRNA knockdown did not significantly affect target genes in the short term (see section 2.4), continuous moderate MEIS-depletion could still affect proliferation. Limited MEIS reduction could thus mirror the RLS-related physiology of MEIS1 more closely, as patients showed only moderately reduced MEIS1 levels in brain tissue (Xiong et al., 2009). To reveal the impact of MEIS on proliferation and differentiation, shRNA-mediated gene knockdown of MEIS1 or MEIS2 was performed simultaneously with growth factor withdrawal-induced neuronal differentiation. MEIS1 and MEIS2 knockdown was conducted in two independent experiments, each using scrambled shRNAmir as control. Seven to eight replicate wells per shRNAmir were used. Cells were stained against PHH3 and BrdU after nine days in culture without growth factors. Mean fluorescence intensity for both markers was determined by automated cell detection. The number of cells counted per sample varied between 96 and 60,000 for *MEIS1*-shRNAmir, and between 3000 and 373,000 for *MEIS2*-shRNAmir. To minimize random stochastic effects, samples counting less than 3000 cells were removed from analysis. In three cases, samples were removed from analysis due to focus errors during automated image acquisition. In total, 457,171

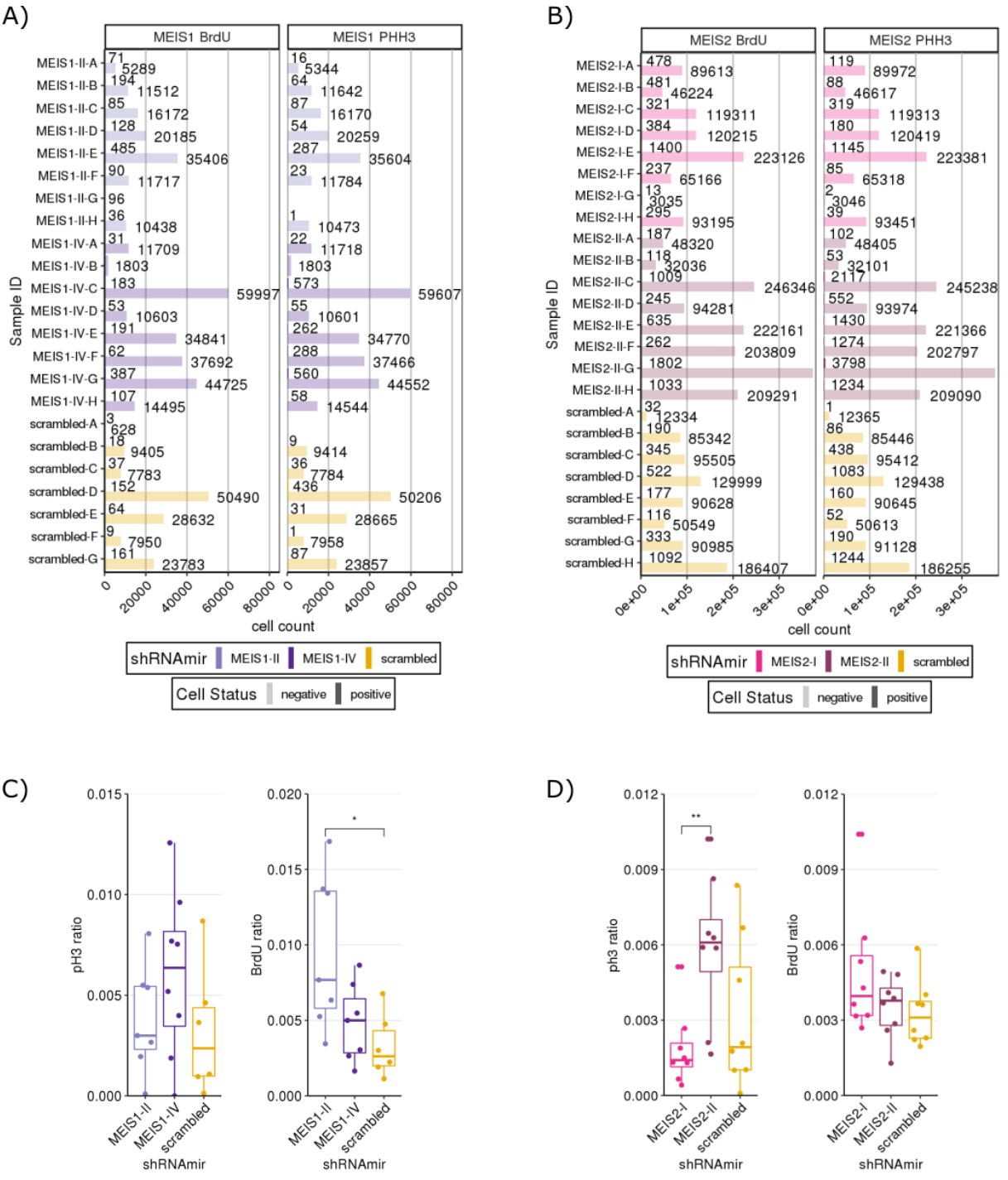

Figure 2.5.2: Proliferation markers in hNSC show no response to shRNAmir. A),B) Counts for positive and negative cells by well, stained against phosphohistone H3 (PHH3) or Bromodeoxyuridine **(**BrdU). Individual wells show strong variation in cell numbers. Number of positive cells is low and accounts for <1% for both BrdU and PHH3 staining. C), D) Ratio of positive to negative cells for PHH3 and BrdU staining. MEIS1 or MEIS2 knockdown did not result in systematic effect on proliferation. Though individual comparisons suggest significant differences between groups, these were not consistent among the shRNAmir for the same target, and proliferation markers did not show consistency either. these did not hold up after correction for multiple testing. Differences were comparable among MEIS-shRNAmirs and between scrambled shRNAmir. Welch's t-test was used to assess differences between shRNAmirs, P-value given for pairwise comparisons: * < 0.05, ** < 0.01. N= 6-7 images.

and 2,943,404 cells were analyzed for *MEIS1* and *MEIS2* knockdown, respectively (Figure 2.5.2A-D).

Proliferation rates of cells in each sample well were determined by counting BrdU/PHH3-positive and BrdU/PHH3-negative cells, and subsequently calculating the ratio of positive/negative cells for each acquired image, a higher ratio indicating higher proliferation. The ratios were compared between shRNAmirs, and differences between groups evaluated by Welch's t-test (Figure 2.5.2C&D). *MEIS1* knockdown with MEIS1-II significantly increased the ratio of BrdU-positive cells compared to scrambled shRNAmir (Figure 2.5.2C, $P < 0.05$). However, this was not observed for MEIS1-IV shRNAmir, despite the higher knockdown efficiency of MEIS1-IV compared to MEIS1-II found in earlier experiments (Figure 2.5.2E&G). In addition, no effect was observed for PHH3 positive cells. Furthermore, the low ratio of proliferative cells, staining positive for BrdU or PHH3, complicated statistical analysis by increasing the influence of stochastic effects and resulted in high variance between samples (relative standard deviation ranged from 0.35 to 1). Notably, the amount of BrdU-positive and PHH3-positive cells after lentiviral transduction and differentiation was more than 40 times lower compared to the previous experiment (Figure 2.5.1C), in which no lentiviral vectors were used. In summary, the experiment appears to lack robustness, and therefore no conclusions could be drawn from the results.

2.6 Genomic binding landscape of MEIS transcription factors

While the genomic binding landscape of MEIS transcription factors has been investigated in neural cells in the mouse embryonic eye and neurally induced P19 carcinoma cells (Dupacova et al., 2021, Mahe et al., 2017; Marcos et al., 2015), studies in human tissue and cell lines have been restricted to hematopoietic and solid tumors (Lin et al., 2019; Novershtern et al., 2011; Nurnberg et al., 2012). I therefore studied a human neural cell line, to overcome possible interspecific differences in MEIS1 binding specificities.

2.6.1 MEIS ChIP-seq in cultured human neural cells

ChIP-seq in human neural stem cells (hNSC) was performed using a combination of two antibodies against MEIS1 and MEIS2, thus identifying binding sites of both transcription factors.

In addition, eight publicly available datasets were analyzed. Three were generated from leukemia-derived cell lines, K562 (myelogenous leukemia), SEM (acute lymphoblastic leukemia) and CHRF-288-11 (acute megakaryoblastic leukemia), while

the remaining were created from hematopoietic stem and progenitor cells (HSPC), Ewing bone sarcoma, as well as embryonic mouse eye, trunk and ganglionic eminences (Table 2.6.1). The publicly available datasets were generated by various sources, using different immunoprecipitation protocols and antibodies, and differ in number of replicates, library preparation methods as well as sequencing chemistry. Biological replicates were only present for hNSC, K562, SEM and HSPC, and for embryonic eye and Ewing sarcoma, no input controls (background controls) were available. These differences are of key importance for data analysis and need to be considered when comparing datasets.

Read count among ChIP-seq datasets differed widely, ranging from 3 to 60 Mio per replicate (6 Mio to 56 Mio per experiment, (Figure 2.6.1A). Three datasets were removed from further analysis (CHRF-288-11, HSPC, Ewing sarcoma), due to insufficient read depth, as a minimum of 10 Mio reads per replicate (20 Mio reads per experiment) is generally recommended for ChIP-seq experiments (Landt et al., 2012).

The fraction of reads within peaks (FRiP), estimating immunoprecipitation efficiency and enrichment (Figure 2.6.1B), displayed high variance between experiments, with values ranging from 0.1% for HSPC, mouse trunk and eye to 10% for K562. While this variation can partly be explained by expression differences and binding patterns of MEIS in different cell types, the strongest effect is likely due to differences in immunoprecipitation efficiency.

Table 2.6.1: ChIP-seq data overview. Hs: Homo sapiens, Mm: Mus musculus

Tissue / cell line	Species	NCBI Accession #	Publication	Repli-cates
Neural stem cells (hNSC)	Hs	unpublished	Kittke et al., unpublished	2
SEM (ALL-derived)	Hs	GEO: GSE38339	unpublished	2
K562 (ML-derived)	Hs	GEO: GSE127590	unpublished	2
CHRF-288-11 (AMKL-derived)	Hs	SRA: ERR063469	Nurnberg et al., 2012	1
Ewing Sarcoma	Hs	GEO: GSE109477	Lin et al., 2019	1
HSPC ($CD133^+$)	Hs	GEO: GSE26014	Novershtern et al., 2011	3
Ganglionic Eminences (GE, E14.5)	Mm	GEO: GSE231779	Dvoretskova et al., 2024	1
Trunk (E11.5)	Mm	GEO: GSE39609	Penkov et al., 2013	1
Eye (E10.5)	Mm	GEO: GSE62786	Marcos et al., 2015	1

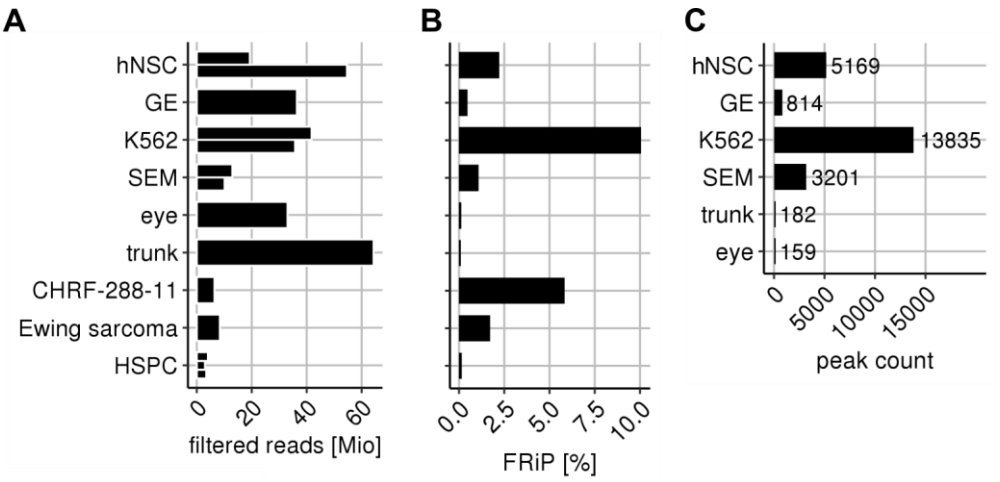

Figure 2.6.1 Quality assessment of ChIP-seq datasets reveal differences between experiments. A) count of mapped and filtered reads per biological replicate. Number of replicates varies across cell types B) Fraction of reads in peaks (FRiP), averaged across replicates. C) Number of peaks called for each dataset.

2.6.2 MEIS peaks are predominantly located in regions distal to TSS

The number of MEIS binding sites (peaks) varied significantly between samples. Irreproducible discovery rate (IDR) was used to determine high confidence binding sites, resulting in 159 to 13,800 peaks per dataset (Figure 2.6.1C), with 5169 peaks detected in hNSC.

Binding sites were found both near and distal to transcriptional start sites (TSS, Figure 2.6.2A). Distribution of peaks varied among cell types, with 10-25% of peaks located within 5 kb of a TSS (TSS-associated, TSSA), which includes the promoter region. In hNSC, peaks with high enrichment were found less frequently within TSSA regions (Supplementary Figure 2A). Across all samples, MEIS most frequently bound to TSS-distal regions, both intragenic and intergenic (Figure 2.6.2A).

The datasets of GE, trunk and eye, derived from mouse samples, were first converted to human coordinates. Peak positions were compared after combining all datasets, and merging overlapping peaks, thereby generating a global, non-redundant peak list containing 21890 peaks. The vast majority of peaks was found only in one dataset, with fractions of specific peaks varying from 64% to 93% (Figure 2.6.2B; hNSC: 88%, GE: 86%, K562: 93%, SEM: 75%, eye: 86%, trunk: 64%), indicating high tissue-specificity of MEIS targets.

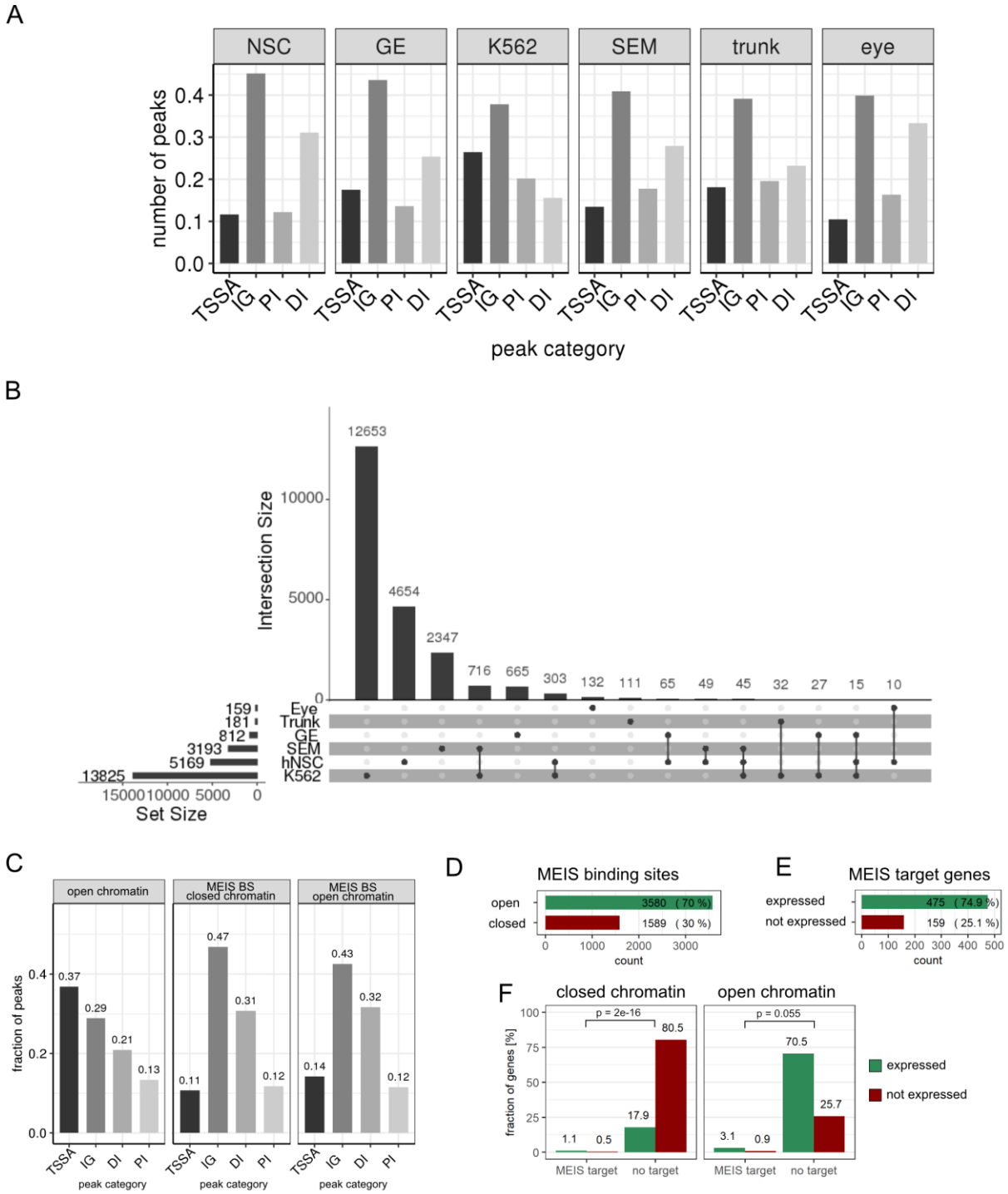

Figure 2.6.2: MEIS binding site distribution and genomic context. Peaks were assigned to nearest transcriptional start site A) Peaks assigned to genomic categories: TSSA: TSS-associated, within 5 kb up- or downstream of TSS. IG: intragenic, located within the gene body. PI: proximal intergenic, intergenic region within 50 kb of TSS. DI: distal intergenic, intergenic region >50 kb of TSS. B) Number of overlapping peaks between datasets. Set size: number of peaks within each dataset, percentages indicate fraction of peaks specific to each dataset. Bars represent the number of overlapping peaks for each intersection between datasets, indicated by the connected dots below. Single dots: peaks only found in one dataset. Top 15 intersections are displayed. C) Distribution of open chromatin regions among genomic categories in hNSC, relative to the TSS of the nearest gene. D) Chromatin state in all MEIS binding sites in hNSC. E) Expression of direct MEIS target genes in hNSC. F) Gene expression in relation to MEIS binding and chromatin state. Expression of direct MEIS target genes was compared against non-target genes, dependent on the chromatin state at the TSS using Pearson's Chi-squared test with Yates' continuity correction. Expression differed highly between MEIS targets and non-targets in closed chromatin regions (P = 2e-16), but not in open chromatin regions (P = 0.055).

I used published data of assay for transposase-accessible chromatin using sequencing (ATAC-seq) in hNSC (Lam et al., 2022) to elucidate the relation between MEIS binding sites and chromatin state. MEIS binding sites were more prevalent in (OCR) than in closed chromatin regions (CCR; 70% and 30%, respectively; Figure 2.6.2D). OCR were then categorized by their distance to the nearest gene, being located predominantly in the vicinity of TSS (37%, Figure 2.6.2C), while only 14% of MEIS binding sites were located in TSSA regions. MEIS binding sites in OCR were only slightly more abundant in (TSSA) regions (14% vs 11%), compared to binding sites in closed chromatin regions (CCR, Figure 2.6.2C), highlighting MEIS' preference for promoter-distal binding.

In-house mRNA expression data of hNSC was used to study potential relationships between gene expression and MEIS binding. Peaks were assigned to genes when located within +-5 kb of a TSS using ChIPseeker, yielding 648 direct target genes in hNSC (Fig. 2.6.3A). Of all genes assigned to MEIS binding sites, 75% were also expressed in hNSC. Grouping target genes by chromatin status, we found that in CCR, MEIS targets were more frequently expressed compared to non-targets (Figure 2.6.2F, Pearson's Chi-squared test, p = 2e-16), while no significant difference was detected in OCR (P = 0.055), suggesting MEIS binding results in increased gene expression in CCR.

2.6.3 MEIS targets vary between tissues and control specific biological functions

From the non-redundant peak list of 18381 peaks across all samples, 9431 genes were inferred with a TSS closest to any MEIS binding site within one million bases. Target gene overlap revealed lower specificity between datasets, compared to peak overlap (Supplementary Figure 3; hNSC: 28% vs. 63%, GE: 25% vs. 47%, K562: 74% vs. 92%, SEM: 30% vs. 44%, eye: 25% vs. 64%, trunk: 20% vs. 40%). As promoter-distal regulatory elements rarely interact with the nearest TSS (Jung et al., 2019), peaks were assigned to transcripts only if located within 5 kb of a TSS for subsequent analyses. Among these direct, promoter-bound genes, target gene specificity was lower compared to peak specificity (Figure 2.6.3A, hNSC: 63%, GE: 47%, K562: 92%, SEM: 44%, eye: 64%, trunk: 40%).

Overrepresentation analysis was used to determine whether target genes were enriched within functionally pre-defined sets of genes of the REACTOME database (Jassal et al., 2020). The enriched pathways differed substantially between

datasets (Figure 2.6.3B). In hNSC and GE, MEIS targets were enriched for regulators of the Notch and Wnt signalling pathways, in K562 regulators of Golgi-associated transport and Rho/GTPase signalling were targeted, while in embryonic trunk HOX gene activators were major enriched targets. The low number of direct MEIS targets in the embryonic eye did not permit meaningful enrichment analysis.

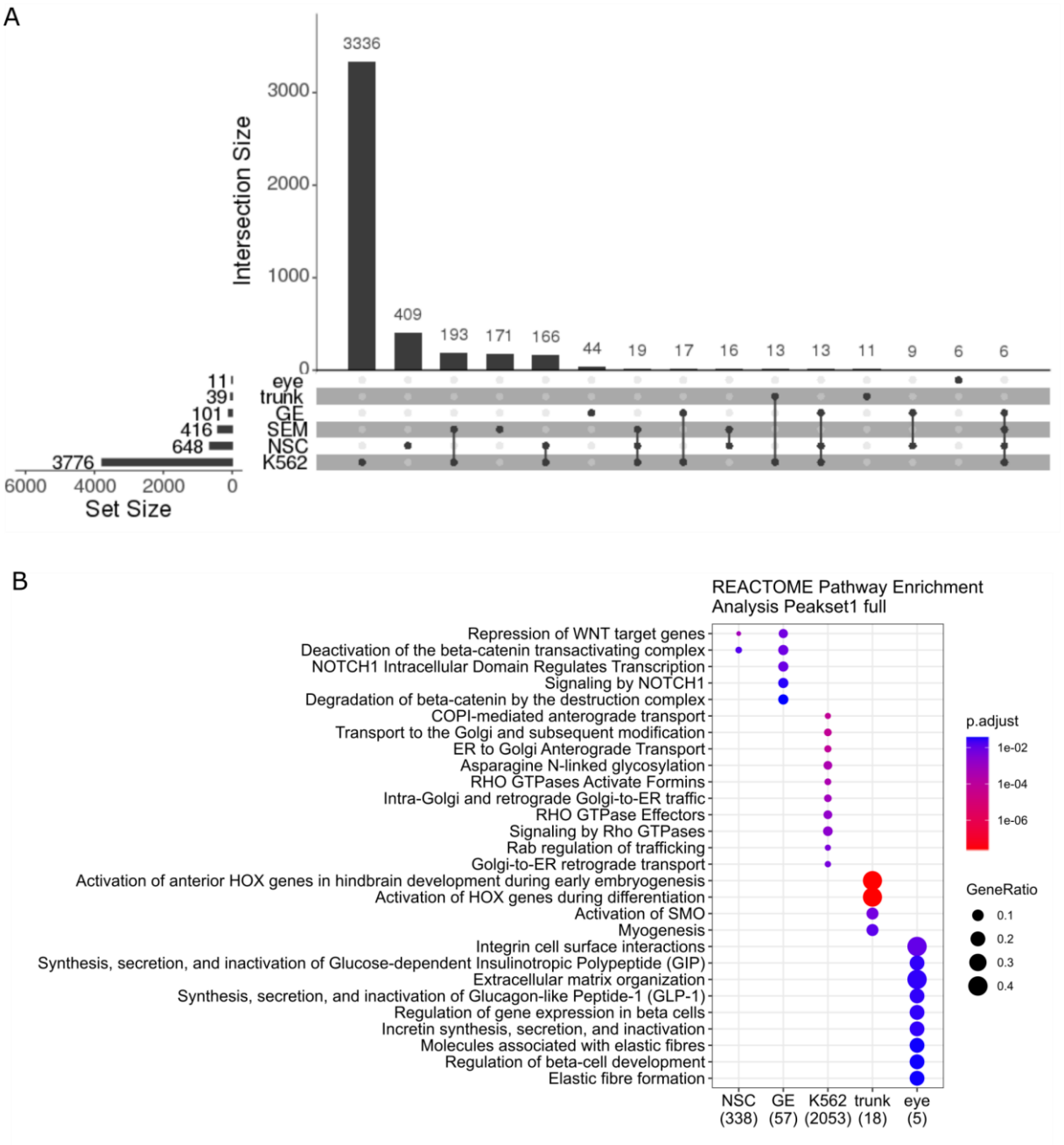

Figure 2.6.3: MEIS target genes vary across tissues. A) Overlap between direct target genes of MEIS ChIP-seq datasets. Direct target genes were assigned when a peak was located within 5 kb of a transcriptional start site. B) Pathway enrichment analysis, performed with direct MEIS target genes using clusterProfiler. Gene ratio indicates the fraction of input genes occurring in a given gene set. Numbers in parentheses indicate genes included in the REACTOME database. P-value was adjusted with the Benjamini-Hochberg procedure, cutoff P = 0.05.

2.6.4 MEIS binds to promoters of known and newly discovered targets and to RLS-associated genes

In hNSC, MEIS binding sites were detected within 5 kb of the TSS of 648 transcripts, including transcripts of *MEIS1* and *MEIS2* themselves, as well as transcripts of TALE homeodomain transcription factors *PBX1*, and *PREP2* (*PKNOX2*). Of these four target genes, none was exclusive for hNSC, with *MEIS1*, *MEIS2* containing promoter-associated peaks in four and three other datasets, respectively (Table 2.6.2).

Further target genes were selected for comparison, based on previously described functions of MEIS1 and MEIS2. Wnt/Notch-associated genes *TLE1*, *TLE4*, *HES1*, and *SOX13* were identified as direct targets, all essential regulators of neural differentiation (Ochi et al., 2020; Verginelli et al., 2013; Wang et al., 2005). Furthermore, the cell cycle regulators cyclin D2 (*CCND2*) and *POU3F3* were exclusive to hNSC, while *SOX2* was targeted in both hNSC and GE.

MEIS was found to bind 21 out of 658 putatively RLS-associated genes from a current meta-analysis of three independent RLS GWAS (Schormair et al., 2024), including the *MEIS1* gene itself. The 658 genes were selected because they had been prioritized by at least one of four gene prioritization methods using the summary statistics of the meta-analysis. These methods were: 1) DEPICT gene prioritization (FDR < 0.05), 2) MAGMA gene-based association test (FDR < 0.05), 3) FUMA gene prioritization based on eQTLs in all tissues (FDR < 0.05), and 4) TWAS in GTEx brain tissue dataset using S-MultiXcan ($p < 2.5 \times 10\text{-}6$). Of these 24 direct MEIS target genes, 17 were specific for hNSC, and contained several regulators of cell migration, axonogenesis and dendrite formation, including the genes of ephrin receptor *EPHA7*, GTPase activator *RABGAP1L*, neural adhesion molecule *CNTN6*, focal adhesion kinase *PTK2* and filamin A-associated protein 1 *FILIP1*. Further targets included the neurodevelopmental regulator genes *PRMT8*, *LRRN1*, *BCL11A* (*CTIP1*), *ZBTB20*, as well as an isoform of the *KCNAB1 gene,* which encodes a subunit of a voltage-gated potassium channel and is expressed in cortical and striatal neurons.

The aforementioned GWAS also suggested a putative association with RLS for *PBX3.* MEIS binding sites near the TSS of PBX were only found in the mouse GE, located within the promoter and second intron, 7kb downstream of the TSS and overlapping the VISTA enhancer hs1030 (Visel et al., 2007), which is active during early embryonic brain development.

Table 2.6.1: Selected MEIS target genes as determined by ChIP-seq on hNSC and comparison with other MEIS ChIP-seq datasets.

Target gene	hNSC	GE	K562	trunk	SEM	eye
Wnt/Notch pathway						
TLE1	x	x			x	x
TLE4	x	x	x			
HES1	x		x			
KAT2B	x	x				
SOX13	x					
TALE Homeodomain						
MEIS1	x	x	x	x	x	
MEIS2	x	x	x	x		
PREP2	x	x				
PBX1	x			x		
Cell cycle						
CDH2	x					
POU3F3	x					
SOX2	x	x				
Putative RLS-associated genes						
BAZ2B	x		x			
BCL11A (CTIP1)	x					
C15orf41	x		x	x		
CNTN6	x					
DNAH8	x					
EPHA7	x					
FILIP1	x					
FREM1	x					
GALNTL6	x					
KCNAB1	x					
KLF12	x					
LRRN1	x					
MLF2	x					
NBEAL1	x		x			
PDE4D	x		x			
PLAU	x		x			
PRMT8	x					
PTK2	x		x		x	
RABGAP1L	x		x		x	
SAMD5	x					
ZBTB20	x					

2.6.5 Heritability signal of genome-wide association studies within MEIS binding sites

The heritability of polygenic diseases as accessible by GWAS (so-called “SNP heritability”) is not only associated with the reported disease gene loci. Instead, it is heterogeneously distributed over the entire genome, while only those loci reaching the restrictive threshold of genome-wide significance are reported. Therefore, genome partitions such as the MEIS binding sites can be tested for enrichment of the heterogeneously distributed SNP-heritability. If a partition comprises a fraction of the SNP-heritability that is much larger than the partition’s proportion of the genome, then the partition may be considered as being involved in the pathogenesis of the disease. Stratified linkage disequilibrium score regression (S-LDSC, Finucane et al., 2015) is a tool for partitioning SNP heritability by functional annotations using GWAS summary statistics. To test whether MEIS binding sites comprise a disproportionally large component of the RLS SNP-heritability, S-LDSC was applied to the GWAS summary statistics of a meta-analysis of three independent RLS GWASs, involving a total of 116,403 cases and 1,473,166 controls of European ancestry (Schormair et al., 2024). While heritability within conserved regions was 23-fold over global background, heritability within MEIS binding sites was enriched only 3-fold compared to genomic background (Figure 2.6.4A). As high heritability enrichment within conserved regions would overshadow other effects, only the conserved parts within MEIS binding sites were used for further analysis. RLS heritability of conserved regions within MEIS peaks was enriched 45.2-fold over background, almost twice the enrichment compared to conserved regions alone. Conserved regions within open chromatin regions (OCR), determined by ATAC-seq of hNSC, yielded 39.8-fold enrichment.

For comparison, the same enrichment analyses were performed with GWAS of insomnia, schizophrenia and body mass index (Jansen et al., 2019; Loh et al., 2015; Yengo et al., 2018). Results were similar to RLS GWAS, with conserved regions in MEIS binding sites and OCR being 2.2 to 3-fold and 1.7 to 2.9-fold enriched, respectively, when compared to conserved regions alone (Figure 2.6.4A). Notably, overall enrichment within conserved regions in both MEIS peaks and OCR was highest for RLS GWAS, compared to other GWAS.

As the *MEIS1* locus is the most highly RLS-associated region in the genome, its contribution to overall heritability and to genome-wide enrichment within MEIS binding sites was assessed. Repetition of the analysis excluding the MEIS1 locus reduced heritability enrichment within conserved regions by 4%, while enrichment

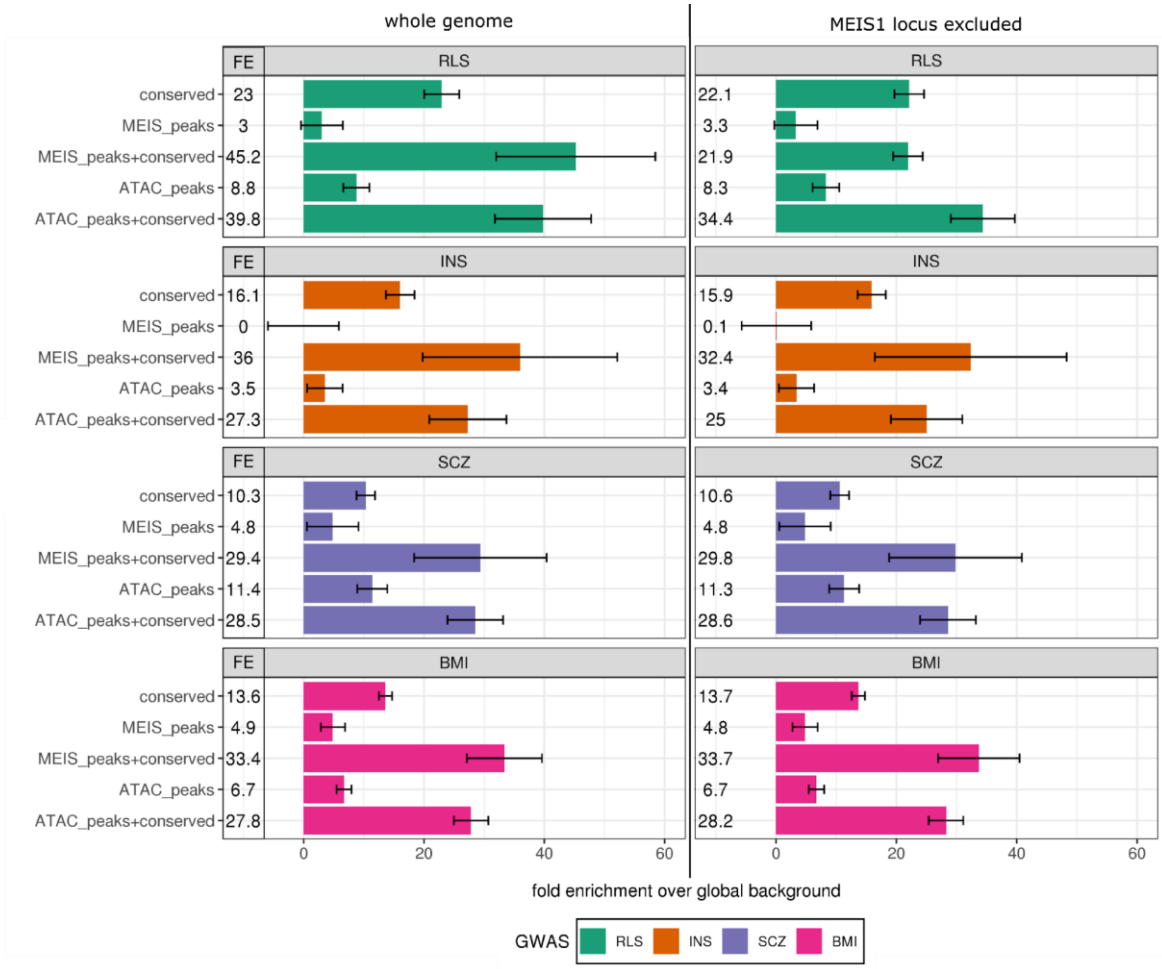

Figure 2.6.4: LD-score regression of MEIS binding sites and open chromatin. Regions were determined by ChIP-seq and ATAC-seq experiments in hNSC. Error bars represent jackknife standard errors (s.e.) around the estimates of enrichment. FE: fold-enrichment, INS: insomnia, SCZ: schizophrenia.

within MEIS binding sites dropped by 51% to 21.9-fold enrichment, similar to the enrichment within conserved regions alone (Figure 2.6.4B). Enrichment in conserved OCR was only reduced by 14%, and thus 1.5-fold higher compared to conserved regions alone. Thus, we do not see an indication that MEIS binding sites convey an increased SNP heritability for RLS.

In contrast, removal of the *MEIS1* locus had little effect on heritability enrichment of other GWAS and did not affect the proportion between MEIS binding sites and OCR, highlighting the importance of *MEIS1* in RLS.

2.6.6 Motif analysis reveals a novel MEIS-associated DNA motif

MEIS binding sequences have been studied in various cell types (Dardaei et al., 2015; Penkov et al., 2013), while investigations in neural cell types remain limited (Marcos et al., 2015; Mahe et al., 2017). In addition to direct binding sequences, motif

analysis reveals possible binding sites of other transcription factors and thus potential co-regulators or competitors.

Consensus DNA sequences within MEIS binding sites were identified using the unbiased search algorithm MEME (Bailey and Elkan, 1994), which detected two to seven significantly enriched motifs per dataset (Supplementary Figure 4).

In all datasets, the core hexameric MEIS consensus binding sequence TGACAG (HEXA motif, Figure 1.4.1B) was identified, ranking highest in hNSC and GE (Figure 2.6.5A). In contrast, the previously described octameric sequence TGATNNAT (OCTA-motif, Figure 1.4.1D) was identified as the most highly enriched motif found in K562, SEM and mouse trunk. Detection of this motif indicates the presence of a trimeric MEIS-PBX-HOX complex, in which MEIS itself does not directly bind to DNA (Shanmugam et al., 1999). Furthermore, the decameric sequence TGATTGACAG (DECA-motif) was detected in hNSC, which is associated with binding of the heterodimeric PBX1-MEIS1 complex (Chang et al., 1997; Knoepfler et al., 1997).

A previously undescribed motif with the consensus sequence WDAYRTCTTHATTW was associated with MEIS binding sites in hNSC and showed the second-highest enrichment ($E=1.3*10^{-81}$, Figure 2.6.5B), henceforth referred to as MEIS-associated motif. Comparison with the JASPAR database of known transcription factor binding motifs (Fornes et al., 2020) using TOMTOM (Gupta et al., 2007), did not show significant similarity with known motifs (adjusted $P > 0.1$). While transcription factor motifs are enriched around ChIP-seq peak centers, the distribution of the MEIS-associated motif across all peaks showed distinct bimodal enrichment between 10 and 20 bp from the peak maxima (Figure 2.6.5C).

The HEXA motif was detected in 2061 (40%) out of 5169 MEIS binding sites using the motif identification tool FIMO. An additional 1083 (21%) peaks contained both HEXA and MEIS-associated motifs (Grant et al., 2011, Figure 2.6.5D), while the MEIS-associated motif alone was found in 928 (18%) peaks. Preference for genomic regions was observed when grouping peaks by presence of HEXA and accessory motifs (Figure 2.6.5E, Pearson’s chi-squared test $p=0.014$), driven by reduced preference of binding sites with accessory motif for TSSA, compared to binding sites with exclusively HEXA motif, or no motif.

In peaks containing both HEXA and MEIS-associated motif, they frequently appeared in close proximity (Figure 2.6.5F). In these peaks, motif orientation and spacing showed a preference for oppositely orientated motifs with 2&3 bp spacing, as well as

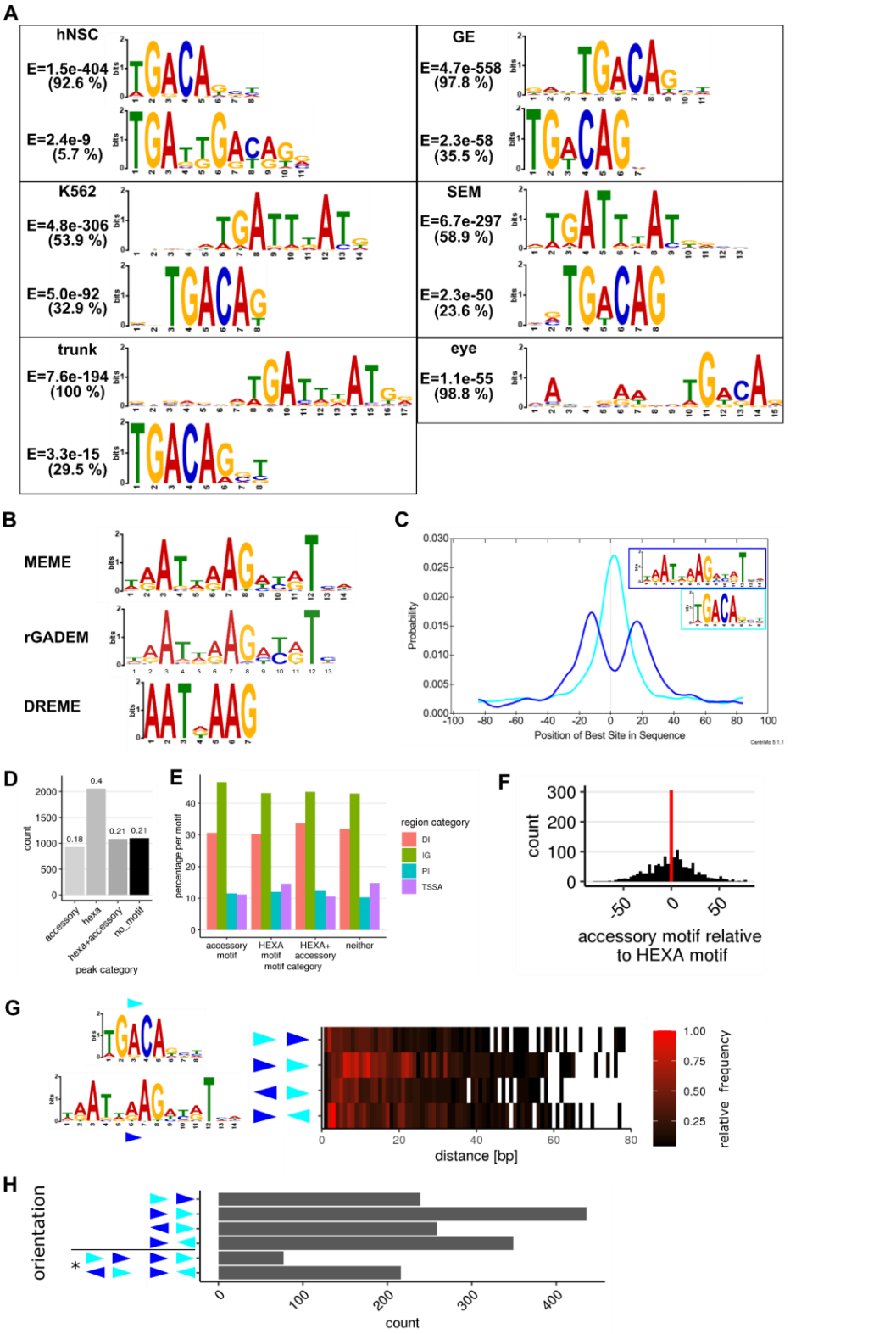

Figure 2.6.5 MEIS binding motif preference differs between neural and non-neural tissues. A) Known MEIS-associated binding motifs identifed by MEME. Percentage in parenthesis indicates the fraction of peaks carrying the sequence. B) A previously undescribed binding motif was determined independently by MEME, rGADEM and DREME. C) Average distribution of the MEIS consensus motif and accessory motif across all peaks, relative to each peak center. D) fractions of peaks in hNSC carrying accessory or hexa, both accessory and hexa or no motifs, identified by FIMO. E) genomic region distribution of peaks, grouped by presence of binding motifs. Percentage of each region category per motif class. Presence of motifs is not independent from region category (Person's chi-squared test, p=0.014) F) Histogram of distances between HEXA and accessory motifs. Red bar indicates overlapping motifs G) Distance and relative orientation of HEXA and accessory motifs. Arrowheads indicate motif orientations. Heatmap indicates ratio between counts of motif constellations, divided by the maximum count observed for any distance. Instances of overlapping motifs were omitted from the analysis. H) Frequencies of relative orientation of HEXA and accessory motif. Asterisk indicates instances of overlapping motifs. Distinction was only made between opposite and identical orientation.

for evenly oriented motifs with 5-10 bp spacing, but only when the MEIS-associated motif was located upstream of the HEXA motif (Figure 2.6.5H).

3 Discussion

3.1 Embryonic MEIS1 expressing cell types contribute to multiple regions in the forebrain

Meis1 is highly expressed in the ganglionic eminences (GE) of the embryonic mouse brain and the intronic, RLS-associated enhancer element HCNR 617 displays spatially and temporally restricted activity in the GEs during embryogenesis (Spieler et al., 2014; Toresson et al., 2000). MEIS1-positive cell populations in the forebrain were thus characterized to identify possible implications in brain development.

Using immunofluorescence (IF) I confirmed previously described MEIS1$^+$ populations in the intermediate zone (IZ, prospective caudoputamen) and marginal zone (MZ, prospective piriform cortex) of lateral and caudal ganglionic eminences (LGE and CGE), marginal zone of the medial ganglionic eminence (MGE, prospective ventral striatum), the ventricular and subventricular zones (VZ and SVZ) of the LGE, as well as in the ventral septum (Barber et al., 2013; Spieler et al., 2014; Toresson et al., 2000). Furthermore, I showed that MEIS1 expression in the piriform cortex extends and increases intensity in a caudal direction, peaking in the CGE, including the prospective amygdalar area (Figure 2.1.1).

MEIS1 expressing cell types differ depending on their spatial position, and analysis of co-expression with neural marker genes determined at least four different cell types expressing MEIS1.

The piriform cortex and ventral striatum, harboring the largest population of MEIS1$^+$ cells, are comprised of cells originating from the pallial and subpallial LGE, MGE, dorsal telencephalon and rostromedial telencephalic wall and septum (Carney et al., 2006; Ceci et al., 2012; Garcia-Moreno et al., 2008; Marin et al., 2001; Martin-Lopez et al., 2019), rendering the developmental origin of this MEIS1$^+$ population unclear. Nevertheless, the absence of the excitatory neuronal lineage markers PAX6, TBR2 (EOMES) and TBR1 (Englund et al., 2005) in all MEIS1$^+$ cells (Figure 2.1.2) indicates either an inhibitory identity, and therefore a subpallial origin (Rubenstein and Campbell, 2013; Rubenstein and Rakic, 2013), or glial identity. A subpopulation of MEIS1$^+$ cells in the lateral piriform cortex (PCX) co-expresses CTIP2 (BCL11B), typically expressed in both glutamatergic projection neurons and GABAergic interneurons of upper and deep layers in the adult somatosensory cortex (Arlotta et al., 2005; Chen et al., 2008; Nikouei et al., 2016). Due to the lack of excitatory

markers, MEIS1$^+$/CTIP2$^+$ cells of the PCX may therefore constitute MGE- or PoA-derived interneuron precursors, migrating along the superficial migratory route (Figure 1.3.1, Anderson et al., 2001; Marin et al., 2001.), and ceasing MEIS1 expression before reaching the somatosensory cortex. This would also explain the presence of individual MEIS1$^+$/CTIP2$^+$ cells in the isocortex, dorsal to the PCX (Figure 2.1.2F).

MEIS1$^+$/CTIP2$^-$ cells increased towards the ventral PCX and throughout the ventral striatum, possibly representing one of the numerous interneuron classes found in this brain region (Cansler et al., 2020). Examinations of further developmental stages will help to reveal if MEIS1$^+$/CTIP2$^+$ and MEIS1$^+$/CTIP2$^-$ belong to different neuronal lineages or represent different stages of the same lineage.

In most, if not all, MEIS1$^+$ cells in the caudoputamen, co-expression of MEIS2 and CTIP2 was observed (Figure 2.1.2A&F), which both control the differentiation of medium spiny projection neurons (MSN, Arlotta et al., 2008; Ghanem et al., 2008; Waclaw et al., 2010).

Finally, a progenitor population expressing *Meis1*-transcripts throughout the VZ and SVZ of the LGE was identified by in-situ hybridization, which had earlier been described at the protein level (Barber et al., 2013). The ventral LGE generates precursors of striatal medium spiny neurons in the caudoputamen and ventral striatum, migrating in a dorsoventral direction along the ventral migratory course (VMC, Martin-Lopez et al., 2019). Dorsal LGE-derived progenitors give rise to glutamatergic projection neurons of the piriform cortex and amygdala, moving along the lateral cortical stream (LCS, Bai et al., 2008; Carney et al., 2006). However, no MEIS1$^+$ cells were identified along either the VMC or LCS, suggesting MEIS1 expression in the LGE is limited to progenitors in the VZ and SVZ, and to MSN precursors of the caudoputamen. Optimization of stainings will be required to characterize the progenitor cell types in the LGE.

While spatial analysis of MEIS1 expressing cells and co-labelling for neural markers yields cues to cell type and regional identity in the adult brain, lineage tracing using Cre-loxP reporter systems will be required to precisely characterize their fate. Integration of these histological studies with single cell RNA-sequencing (scRNA-seq), can help to determine cell type identity while mapping their spatial positions.

Characterization of MEIS1 expressing cell types is one approach to unravel the developmental origins of RLS. As MEIS1 is a widely expressed transcription factor

with varying developmental functions, its role on a molecular level must be considered in detail. Altered MEIS1 expression can potentially affect interaction partners and downstream targets alike. For instance, the TALE homeodomain transcription factor PBX1 is expressed in the GE, overlapping regions of MEIS1 expressing cells (Toresson et al., 2000). Disruption of PBX1 expression in the embryonic forebrain causes defects in neuron distribution and laminar patterning (Golonzhka et al., 2015). Furthermore, interaction with PAX6 and SOX2 transcription factors, or targeting their respective genes *Pax6* and *Sox2* in LGE-progenitors, may control proliferation and differentiation.

The expression of MEIS1 in progenitors, MSN precursors and cortical neurons suggests varying roles in different cell types, which requires regulation of cell-type and function-specific sets of target genes. It is therefore imperative to identify MEIS1 targets specific to individual neural cell types.

3.2 Gene knockdown is required to identify pathways controlled by MEIS1

While shRNA-mediated knockdown of *MEIS1 and MEIS2* was successful in two human stem and progenitor cell lines, mRNA depletion was insufficient to markedly affect MEIS1 protein expression, or the expression of known and potential MEIS target genes (Figure 2.4.2).

Previous studies showed that mRNA does not correlate very well with protein levels, owing to regulatory processes that occur post-transcriptionally, translationally, or that affect protein stability and degradation (Vogel and Marcotte, 2012). This effect was shown to be especially pronounced in brain tissue (Bauernfeind and Babbitt, 2017), and likely applies to neural stem and progenitor cells in vitro. To achieve effective depletion of MEIS protein in neural cells, higher mRNA knockdown efficiency is therefore crucial to achieve effective depletion of MEIS protein in neural cells, in order to identify downstream targets of MEIS transcription factors.

As no increase in expression of the apoptosis marker TP53 (Kerr et al., 1972, Figure 2.4.2C) was found in response to lentiviral transduction, and therefore presumably no increase in apoptotic cells, lentivirus transduction itself appears to affect cell proliferation. Previous studies suggested that shRNA vectors themselves can trigger an interferon response (Bridge et al., 2003), known to inhibit proliferation and tumor growth (Ivashkiv and Donlin, 2014), and thus may explain the reduced proliferation after lentiviral transduction.

In future experiments, these effects will have to be minimized, so that they do not mask the effects of mRNA knockdown. Furthermore, a higher ratio of fraction cells is required to identify reproducible effects and differences.

3.3 MEIS1 knockout in iPSC may be partially compensated by MEIS2

Successful CRISPR/Cas9-mediated knockout of MEIS1 in human iPS-cells enables the investigation of MEIS1 in neurodevelopmental processes in vitro, using the successfully established differentiation to cerebral organoids (Bagley et al., 2017), as well as further differentiation methods to generate GABAergic neurons (Close et al., 2017; Yang et al., 2017). In *MEIS1*$^{-/-}$ cells, I observed upregulation of *MEIS2* transcripts, indicating a compensatory mechanism between MEIS proteins, which has already been observed in leukemic cells as well as eye and neural crest development (Antosova et al., 2016; Lai et al., 2017; Machon et al., 2015), facilitated by the high degree of homology between MEIS1 and MEIS2. This compensation could mitigate effects of the *MEIS1* knockout during differentiation but can be overcome by the generation of *MEIS1/MEIS2* double-knockouts.

3.4 MEIS TF can bind promoter-distal regulatory elements in open and open and closed chromatin regions

In hNSC, MEIS was found to preferentially bind promoter-distal elements (Figure 2.6.2A), as had been shown in earlier studies in embryonic mouse trunk, eye and carcinoma cells (Dardaei et al., 2015Marcos et al., 2015; Penkov et al., 2013). MEIS binding sites in hNSC were located both in open and closed chromatin regions (Figure 2.6.2C-F). Recently, MEIS and PBX1 were shown to jointly bind closed chromatin at the doublecortin gene (*Dcx*) promoter, recruiting chromatin remodeling complexes and thus causing de-compaction and consequently initiating neuronal differentiation in the adult mouse brain (Hau et al., 2017). Similarly, in differentiating myoblasts, MEIS1 and PBX1 facilitate chromatin remodeling during early myoblast differentiation by recruiting MYOD (Pliner et al., 2018).

The majority of direct MEIS target genes in hNSC, bound near the transcriptional start site (TSS), were found to be expressed in this cell type (Figure 2.6.2E), arguing for a role as transcriptional activator, which was previously suggested to be more pronounced when binding to distal regulatory elements, compared to promoter

regions (Pliner et al., 2018). However, Penkov et al. (2013) suggested a transcriptionally repressive function of MEIS when binding directly to a promoter. In addition, the low expression of MEIS1 in hNSC must be considered, likely limiting the effect on overall target gene expression. Additional studies are required to characterize transcriptional regulatory properties of MEIS, specifically focusing on interaction partners. Furthermore, the majority of promoter-distal MEIS binding sites have not been characterized, preventing the assignment of downstream target genes.

3.5 MEIS targets WNT and cell cycle regulators

A high tissue specificity was observed when comparing MEIS binding sites from different studies, and target genes were associated with specific regulatory pathways (Figure 2.6.3). In hNSC and mouse ganglionic eminences, MEIS targets were enriched for regulators of the WNT and NOTCH pathways, which are known to be regulated by MEIS in the embryonic mouse eye (Marcos et al., 2015). WNT/NOTCH signaling is essential in brain development, including regulation of neurogenesis in the MGE, cortical progenitors and the olfactory bulb (Munji et al., 2011; Bocchi et al., 2017; Hirabayashi et al., 2004; Ma et al., 2019; Wang et al., 2011). MEIS1 binds the promoters of the WNT and NOTCH regulators *TLE1*, and *HES1*, which collaborate in the repression of neurogenesis in telencephalic progenitors (Yao et al., 2001).
In hNSC, a binding site within *CCND2* (encoding cyclin D2) was discovered, making it a potential target gene. MEIS1 and MEIS2 are known regulators of cell cycle control, maintaining a proliferative state by driving *Ccnd*1 expression in retinal progenitors in the zebrafish and chick eye (Bessa et al., 2008; Heine et al., 2008).
These results confirm the role of MEIS proteins as cell-cycle regulators, contributing to the list of known proliferation-driving targets. Whether MEIS TF act as drivers of proliferation or differentiation in hNSC remains to be established.

3.6 RLS-associated genes implicated in forebrain development are regulated by MEIS in neural cells

A new meta-analysis of genome-wide association studies identified 164 genetic loci (Schormair et al., 2024), putatively contributing to RLS. MEIS targets in hNSC included several RLS-associated genes involved in axonogenesis, dendrite formation and cell motility. Ephrin receptor EPHA7 regulates dendrite development and

interneuron connectivity in the cortex (Beuter et al., 2016; Clifford et al., 2014). Cell adhesion protein contactin 6 (CNTN6*)* regulates neurite outgrowth in sensorimotor neuronal pathways and has been implicated in a neurodevelopmental disorder (Hu et al., 2015; Mercati et al., 2017). Filamin A-associated protein 1 (FILIP1) controls radial migration of cortical progenitors in the ventricular and subventricular zones (Nagano et al., 2002; Nagano et al., 2004; Sato and Nagano, 2005).

Further targets included the RLS-associated transcription factor *ZBTB20*, involved in neurogenesis of interneurons and projection neurons in the olfactory bulb (Doeppner et al., 2019). Defects in ZBTB20 expression were found to affect differentiation in cortical projection neurons and astrocytes as well as dendritic and synaptic structure and cause atypical cortical layer formation (Jones et al., 2018; Nagao et al., 2016; Nielsen et al., 2010; Tonchev et al., 2016). Furthermore, neural-specific deletion of *Zbtb20* in mice increased activity at the end of the dark period (Qu et al., 2016), mirroring the circadian activity pattern in RLS.

Another target, *BCL11A* (*CTIP1*), is expressed throughout the mouse embryonic neocortex (Leid et al., 2004), regulating differentiation and migration of projection neuron progenitors (Canovas et al., 2015; Wiegreffe et al., 2015), and its loss results in a reduction of cortico-thalamic projections (Woodworth et al., 2016).

In the mouse GE, MEIS targeted *Pbx3*, encoding a TALE homeodomain transcription factor which is highly expressed in interneuron progenitors within the ganglionic eminences, but downregulated after neuronal differentiation (Batista-Brito et al., 2008).

In summary, direct MEIS targets include several potentially RLS-associated genes, many of which are known regulators of brain development. Further studies are required to characterize the effect of MEIS on these targets.

3.7 RLS heritability is enriched in open chromatin regions in hNSC

Summary statistics of RLS GWAS were used to quantify SNP-based heritability within MEIS binding sites by stratified LD-score regression (S-LDSC).

While initial analysis suggested an enrichment of RLS heritability within MEIS binding sites, this effect was found to be driven by the RLS-associated locus within *MEIS1*, as removal of the MEIS1 locus from analysis resulted in enrichment comparable to conserved regions alone. At the same time, open chromatin regions (OCR) were enriched for RLS heritability, even after removal of the MEIS1 locus. S-LDSC has

been used successfully to identify heritability enrichment of various traits within open chromatin regions of fetal cell types (Domcke et al., 2020), therefore an enrichment in OCR of hNSC suggests a developmental role in RLS pathophysiology, although further analyses including comparison to other cell types and correction for multiple testing are required.

MEIS binding sites were also enriched for heritability signals in insomnia and schizophrenia, for which a positive genetic correlation has been reported (Schormair et al., 2017). RLS symptoms often affect sleep, and comorbidity with insomnia has been observed in the past (Mucsi et al., 2005). Schizophrenia is a neurodevelopmental disorder, and the enriched heritability within binding sites of MEIS proteins highlights their vital role in neural development. Enriched heritability for high BMI risk within MEIS binding sites reflect the positive correlation between RLS and obesity in an earlier study, attributed to reduction of dopamine receptors in the brain (Gao et al., 2009). Obesity has since been verified as a strong risk factor for RLS (Baran et al., 2018).

3.8 Motifs discovered in MEIS binding sites hint possible co-regulators

Analysis of enriched DNA motifs within MEIS binding sites revealed a previously undescribed motif exclusively in hNSC, which displayed preferences in distance and orientation relative to the MEIS hexa motif. This MEIS-associated motif shared no significant similarity with known motifs, and may present a cell-type specific co-regulator of transcription. Further experiments involving mass-spectrometry will be required to identify proteins binding to the sequence in conjunction with MEIS.

The discovery and strong enrichment of the hexameric MEIS consensus motif TGACAG, previously referred to as the HEXA motif (Penkov et al., 2013), showed a preference of MEIS binding to this motif in hNSC, mouse GE and eye. In non-neural tissues and cells (mouse trunk, SEM and K562), the HEXA motif was discovered, but enrichment was low. In these tissues, the highest enrichment was found for the previously described octameric motif TGATNNAT (Figure 1.4.1D), which was previously discovered to be bound by a trimeric MEIS-PBX-HOX protein complex (Shanmugam et al., 1999), in which MEIS does not directly bind DNA. This complex displays increased DNA-binding affinity compared to dimeric PBX-HOX or MEIS-HOX complexes (Shanmugam et al., 1999). The HOX-dependent OCTA motif was

not discovered in hNSC, mouse GE or eye, as HOX proteins are not expressed rostral to the hindbrain (Duboule, 2007).

MEIS proteins also form heterodimers with other homeodomain TFs in order to localize to the nucleus and bind DNA. Therefore, the identification of protein binding partners is crucial to understand cell-type specific function in the brain. The co-occurrence of further homeobox transcription factor binding motifs with the MEIS1 hexa motif could indicate either protein-protein interaction, co-regulation as part of the same regulatory complex, or opposing function, which has been described for PKNOX1 (PREP1) and MEIS (Blasi et al., 2017; Dardaei et al., 2015), competing for the same binding sequence.

3.9 Cortical projection neuron and interneuron development may rely on MEIS-PBX interaction

The strongest telencephalic MEIS expression was found in the cortical areas lateral and ventral of the GEs, indicating MEIS1 plays an important role in this population. Histological analyses suggested an inhibitory, post-mitotic identity of these cells, which indicates a novel function of MEIS1 in neural tissue, in contrast to previously described roles driving proliferation of retinal progenitors and promoting PAX6-dependent differentiation into excitatory and dopaminergic neurons in the cerebellum and olfactory bulb, respectively (Bessa et al., 2008; Heine et al., 2008; Marcos et al., 2015; Owa et al., 2018). Expression patterns of PBX1 and MEIS2, as well as PBX3 and MEIS1 are highly overlapping in the ganglionic eminences and lateroventral cortex of the embryonic mouse forebrain (Toresson et al., 2000), including the region of highest activity of the RLS-associated enhancer HCNR 617 in the embryonic forebrain (Spieler et al., 2014). MEIS/PBX co-expression was described in the embryonic striatum (Toresson et al., 2000), but the extent and combination of different MEIS/PBX homologs remain unclear.

In-vitro translated MEIS protein favors the HEXA (TGACAG) motif (Chang et al., 1997), and this affinity for the HEXA motif was confirmed by chromatin-immunoprecipitation (ChIP-seq) in cultured cells and in vivo (Dardaei et al., 2015; Mahe et al., 2017; Marcos et al., 2015; Penkov et al., 2013). In contrast, PBX/MEIS heterodimers were found to bind the DECA (TGATTGACAG) motif in vitro (Chang et al., 1997). For PBX alone, in-vitro binding preferred TGATTGATTTGAT and TGATTGAT sequences (Calvo et al., 1999), but this could not be confirmed by ChIP-

seq experiments. The preferred MEIS and PBX binding motifs in non-neural cells differ from the HEXA and DECA motifs, and indicate complex formation with HOX proteins as a preferred mode of action (Penkov et al., 2013; Shen et al., 1997). Since HOX proteins are not expressed in the forebrain (Duboule, 2007), PBX would be expected to preferentially bind the decameric TGATTGACAG motif in concert with MEIS. However, PBX ChIP-seq in the embryonic mouse cortex found the HEXA motif enriched above all other motifs, being present in >75% of peaks, while the DECA motif was found in less than 5% of all binding sites (Golonzhka et al., 2015). For PBX, DNA binding site selection in the brain must therefore be highly dependent on a MEIS interaction partner. Since heterodimerization of PBX with MEIS increases DNA binding affinity and controls nuclear export and import (Chang et al., 1997; Hyman-Walsh et al., 2010), and PBX1 and PBX3 are direct downstream targets of MEIS in hNSC and mouse GE (section 2.6.4), even minor aberrations in MEIS expression are likely to have significant effects on PBX-directed processes in the forebrain.

In excitatory progenitors and neurons in the forebrain, loss of PBX1 resulted in hypoplasia and thinning of superficial cortical layers in the frontal cortex, localized cortical layer inversion and a ventrally expanded dorsomedial cortex (Golonzhka et al., 2015). In contrast, the role of PBX in interneuron differentiation remains mostly undescribed, with only PBX3 known to be expressed in interneuron progenitors in the GEs (Batista-Brito et al., 2008). Lack of excitatory lineage markers in MEIS1^{+} cells and high spatial overlap with PBX3 in the GEs thus suggests a joint control of cortical and striatal interneuron differentiation.

Further studies involving co-immunofluorescence of MEIS1 and PBX3 are required, as well as genetic fate-mapping, in order to determine the adult interneuron subtypes generated from MEIS1- and PBX3 positive progenitors. MEIS1/PBX3 protein interaction can be confirmed by mass-spectrometry (Figeys et al., 2001) of MEIS1-positive cells, purified from embryonic brain of the already established C57BL/ 6N-Meis1^{em1Bcca} line (Xiang et al., 2017) by fluorescence activated cell sorting (Bonner et al., 1972).

3.10 Conclusion & Outlook

With RLS being a multifactorial neurological disorder with an unclear mechanism, understanding the contribution of genetic factors, proteins and individual cell types involved will facilitate the development of targeted treatment approaches.

To this end, I investigated the strongest genetic risk factor, *MEIS1*, in human neural cells in vitro and the developing mouse brain. I identified new target genes of MEIS1 in a neural context, many of which are implicated in RLS, brain development and function of postnatal neurons. Furthermore, I discovered evidence of a putative, cell-type specific transcriptional co-regulator of MEIS1 in neural stem cells. Additionally, I specified MEIS1 expressing cell types in the embryonic mouse brain, which are crucial to understanding the effects of reduced MEIS1 expression in RLS patients. Finally, I propose MEIS1 and PBX3 as regulators of forebrain interneuron development.

Future studies will further specify MEIS1-dependent neural cell types, aided by the ongoing rise of single cell genomics, for instance by detailing the change in neural cell type composition in response to aberrant MEIS1-expression in mouse models and human brain organoids. Together with cell-type specific identification of MEIS1 downstream targets, the molecular pathways governed by this transcription factor will be elucidated, shedding light on how perturbed MEIS1 expression contributes to RLS.

Eventually, patients with high genetic burden could benefit from directly targeting risk genes, opening up additional treatment options without the risk of augmentation associated with currently used drugs.

4 Materials & Methods

4.1 Nucleic Acids

4.1.1 Primers and DNA oligos

Table 4.1.1 Primers and DNA oligos

Type and ID	Sequence (5'>3')
PCR primers	
MEIS1-E3-5-F	TAGGTGCAGCCCGTTGACAG
MEIS1-E3-5-R	GTCCACAGCAGCTACAACCGT
qPCR primers ChIP-seq	
MEIS1-ChIP-qPCR-1a-F	CTAGGGCTTTGTGCATTTGAA
MEIS1-ChIP-qPCR-1a-R	GGTTGTCAACGTGGTGAATG
hs-MEIS1-ChIP-pos-4a-F	AGGAAGCCATTGACCTTTAG
hs-MEIS1-ChIP-pos-4a-R	CAAAACTCATTAGCACTGCC
hs-MEIS1-ChIP-pos-5a-F	AATTTGCAAGCATGTGTTGT
hs-MEIS1-ChIP-pos-5a-R	CATACATCCCACTGTCTCAT
MEIS1-ChIP-1a-neg-F	CGCTGGAGAAAGAGCTAGTG
MEIS1-ChIP-1a-neg-R	GCTGCCTTTGTCTTAGAGGC
MEIS1-ChIP-2a-neg-F	GGGTAGCTGACATCTGTGTT
MEIS1-ChIP-2a-neg-R	CTGCCCACAGGTACTAGATG
shRNAmir oligos	
shRNAmir_MEIS1_I_F	TGTAAAAATAAATCTTCAGTCTATTTCAAGAGAATAGAC TGAAGATTTATTTTTACTTTTTTC
shRNAmir_MEIS1_I_R	tcgaGAAAAAAGTAAAAATAAATCTTCAGTCTATTCTCT TGAAATAGACTGAAGATTTATTTTTACA
shRNAmir_MEIS1_II_F	TGCCCTCTTGGAACAGAGATCATTTCAAGAGAATGATCT CTGTTCCAAGAGGGCTTTTTTC
shRNAmir_MEIS1_II_R	tcgaGAAAAAAGCCCTCTTGGAACAGAGATCATTCTCTT GAAATGATCTCTGTTCCAAGAGGGCA
shRNAmir_MEIS1_IV_F	TGAAGTGAACAATTGGTTTATTAATTCAAGAGATTAATA AACCAATTGTTCACTTCTTTTTTC
shRNAmir_MEIS1_IV_R	tcgaGAAAAAAGAAGTGAACAATTGGTTTATTAATCTCT TGAATTAATAAACCAATTGTTCACTTCA
shRNAmir_MEIS2_I_1F	tcgagaaggtatattgctgttgacagtgagcgTAACTAC TGTAGTATAAATATAtagtgaagc
shRNAmir_MEIS2_I_1R	tgtggcttcactaTATATTTATACTACAGTAGTTAcgct cactgtcaacagcaatataccttc
shRNAmir_MEIS2II_1F	tcgagaaggtatattgctgttgacagtgagcgACACACG CAAAAACTATTTTAAtagtgaagc
shRNAmir_MEIS2II_1R	tgtggcttcactaTTAAAATAGTTTTTGCGTGTGTcgct cactgtcaacagcaatataccttc

4.1.2 shRNA sequences

Table 4.1.2 shRNA sequences

ID	Sequence (5'>3')
MEIS1-I	ATAGACTGAAGATTTATTTTTA
MEIS1-II	CAGTAATGAAATCTGAATCTAA
MEIS1-IV	AAGTGAACAATTGGTTTATTAA
MEIS2-I	TAACTACTGTAGTATAAATATA
MEIS2-II	ACACACGCAAAAACTATTTTAA

4.1.3 Plasmid vectors

Table 4.1.3 Plasmid Vectors

Plasmid	Description / Application	Supplier/source
psPAX2	2nd generation lentiviral packaging plasmid	psPAX2 (Addgene plasmid # 12260) and pMD2.G (Addgene plasmid # 12259) were gifts from Didier Trono
pMD2.G	VSV-G envelope expressing plasmid	
lenti-BB-Ef1a-mRuby3-pamiRNA-E-AAVS1-WPRE lenti-BB-Ef1a-mRuby3-pamiRNA-E-MEIS1_I-WPRE lenti-BB-Ef1a-mRuby3-pamiRNA-E-MEIS1_II-WPRE lenti-BB-Ef1a-mRuby3-pamiRNA-E-MEIS1_III-WPRE lenti-BB-Ef1a-mRuby3-pamiRNA-E-MEIS1_IV-WPRE lenti-BB-Ef1a-mRuby3-pamiRNA-E-MEIS2_I-WPRE lenti-BB-Ef1a-mRuby3-pamiRNA-E-MEIS2_II-WPRE	Lentiviral transfer vectors for shRNAmir expression	gifts from Florian Giesert & Christoph Gruber

4.1.4 Oligo duplex cloning of shRNA

shRNAmir sequences were cloned into the lenti-BB-Ef1a-mRuby3-pamiRNA-E by creating oligonucleotide duplexes with matching overhangs. Oligos were annealed and treated with Polynucleotide Kinase (PNK from NEB, R3539): reaction mix containing 1 µl forward and reverse DNA oligos encoding for shRNAmir (100 µM each), 1 µl 10x T4 ligase buffer (NEB), 0.5 µl PNK (10U/µl) and 6.5 µl ddH_2O was set up, incubated in a thermocycler at 37°C, 30 min followed by 95°C, 5 min before ramping to 25°C at -0.1°C/s. The mixture was then diluted 1:200 in ddH_2O. The lenti-BB-Ef1a-mRuby3-pamiRNA-E vector was digested with EcoRI-HF (NEB) and XhoI

(NEB) and purified. 2 µl of the annealed and diluted oligos were ligated into 100 ng purified vector and transformed into E.coli Top10.

4.1.5 DNA quantification with PicoGreen

DNA was quantified using the Quant-iT™ PicoGreen dsDNA Assay-Kit (Thermo Fisher Scientific, P7589) according to the manufacturer's protocol.

4.1.6 Quantitative real-time PCR (qPCR)

For measurement of mRNA expression in human neural stem cells and neural progenitor cells, RNA was extracted from cells grown in 24-well plates, using the RNeasi mini Kit (Qiagen) as per the manufacturer's protocol. Cells were lysed in buffer RLT supllmented with 40 µM dithiothreitol (DTT) and stored at -80°C until processing. Extraction included on-column DNaseI digest. Reverse transcription was performed using the High-Capacity cDNA Reverse Transcription Kit (Applied Biosystems) with equal amounts of RNA input. qPCR was performed with the Taqman FastAdvanced Master mix (Thermo Fisher Scientific) on a QuantStudio 7 Flex (Applied Biosystems), using gene-specific probes (Table 4.1.4). Mean CT values were calculated from two technical replicates, and normalized by subtracting the mean CT values of GAPDH. The resulting dCT values were averaged across biological replicates and normalized by subtracting the mean dCT value of the control shRNAmir (either PPP1R12C or scrambled shRNAmir), yielding ddCT values. ddCT values were converted to linear form (2^{-ddCT}) for graphical representation. Statistical analyses were performed on dCT values using Welch's t-test in R.

For evaluation of ChIP enrichment, purified DNA samples were analysed using the PowerUp SYBR Green Master Mix (Applied Biosystems).

Table 4.1.4: probes used in quantitative real-time PCR (Integrated DNA Technologies, IDT)

target gene	assay ID (IDT)
CCND1	HS.PT.56a.4930170
CCND2	HS.PT.58.4170183
CDK4	Hs.PT.58.38531977
GAPDH	Hs.PT.39a.22214836
HES1	Hs.PT.58.4181121
JAG1	Hs.PT.56a.14582321
MEIS1	Hs.PT.58.24338203
MEIS2	Hs.PT.58.26282949
NES	Hs.PT.58.1185097
PAX6	Hs.PT.58.3002797
PPP1R12C	HsPT.58.20207588
SOX2	Hs.PT.58.237897.g
TP53	Hs.PT.58.39676686

4.2 Cell Culture

4.2.1 Coating cell culture plates with Geltrex for use with human iPSC, NSC and NPC

Geltrex (Gibco A1413201) was diluted 1:100 in DMEM-F12 (Gibco) according to the manufacturer's protocol. Cell culture plates were covered with with diluted Geltrex solution and incubated at 37°C for at least one hour. If not used directly, plates were sealed with Parafilm and stored at 4°C for up to 10 days.

4.2.2 Culture of human neural stem cells and neural progenitor cells

Human Neural Stem Cells (hNSC) were purchased from Gibco (N7800-100) and cultured in complete StemPro NSC SFM (A1050901) containing epidermal growth factor (EGF) and basic fibroblast growth factor (FGF-β). The Line was originally derived from the H9 (WA09) embryonic stem cell (ESC) line. Cells were cultured in sterile cell culture grade plates, coated with Geltrex at 37°C, 5% CO_2. hNSC were passaged using Accutase: culture media was aspirated and cells washed with DPBS before adding Accutase. Cells were then incubated for 2-3 min. at 37°C and dislodged by pipetting, creating a single-cell suspension. Accutase was neutralized by addition of one volume growth media, before centrifugation at 200 xg for 4 min at

RT. Supernatant was aspirated and cells resuspended in appropriate volume of culture media. Cells were split at a ratio of 1:4 – 1:6.
NPC had previously been produced at the ING, Helmholtz Zentrum München, by differentiation from iPSC (HMGU-12) according to a published protocol (Liu et al., 2013) and were cultured similarly to hNSC, while being maintained in a different growth medium (DMEM/F12, 1:100 B-27 without Vitamin A (Gibco, 12587010), 1:200 N2 supplement (Gibco, 17502048), 1% GlutaMAX (Thermo Scientific, 35050038) 50 ng/ml bFGF (Gibco, PHG0266)

4.2.3 Culture of induced pluripotent stem cells (iPSC)

The human iPSC line HMGU-1 was provided by the Core Facility Induced pluripotent stem cells (CF-iPSC), Helmholtz-Zentrum München. Cells were initially cultured in mTeSR-1 (StemCell Technologies), later in StemFlex (Invitrogen A3349401) on tissue culture plates coated with Geltrex at 37°C, 5% CO_2. Media was generally exchanged daily (2 ml / well in 6-well plate); For StemFlex, double-feeding allowed feeding breaks for two consecutive days (see manufacturer's protocol). Clump cell passaging was performed using Versene (Gibco, 15040033). Cells were washed with 1 volume of Versene and consequently incubated in 1 volume of Versene for 5-10 min at 37° until colonies could be dislodged by applying media with a 1000 µl pipette directly onto the colony, without breaking up the cells completely. The cell suspension was then centrifuged 200xg, 4 min, resuspended in culture media and plated at a ratio of 1:5 to 1:20, depending on the initial density.
MEIS1 and MEIS2 expression was induced by adding 10 µM all-trans retinoic acid to the culture medium for four days.

4.2.4 Culture of HEK 293T cells

HEK293T cells were cultured in DMEM (Gibco, 41965039) with 10% FBS, 1:100 Sodium Pyruvate (Gibco, 11360039) and 1:100 Penicillin/Streptomycin (Gibco, 15140148) at 5% CO_2, 37°C. Cells were passaged using Trypsin-EDTA (Gibco, 25200056) at ratios between 1:10 and 1:50.

4.2.5 MEIS1 knockout in human induced pluripotent stem cells

CRISPR Cas9-mediate knockout was achieved by introducing frameshift mutation in exon 3 of *MEIS1*, using the Alt-R CRISPR-Cas9 system (Integrated DNA

Technologies) as per the manufacturer's protocol in the human iPS cell line HMGU1, (provided by the Institute for Stem Cell Research, HMGU München). In brief, a single-cell suspension of iPS cells was generated, treated with 1x RevitaCell solution 1h prior. 150,000 cells were resuspended in 20 µl nucleofection solution (16.4 µl P3 Nucleofection solution, 3,6 µl Supplement) before adding 5 µl RNP (4.6 µM crRNA:tracrRNA, 4 µM Cas9 nuclease, and 4 µM Cas9 electroporation enhancer) containing the target-specific crRNA against exon3 (GCTGACCTGTTTGGCGAACA). Electroporation was performed using the Amaxa 4D nucleofector with the P3 primary cell kit, pulse code CB-156. Cells were carefully resuspended in StemFlex containing 1x RevitaCell, and plated to 1 well in a 24 well plate. After cells recovered for up to 5 days and reached 80% confluency, a single cell solution was generated using Accutase, and 1000 cells were plated to a 60 mm culture dish containing StemFlex with 1x RevitaCell. Colonies were manually transferred to 24 well plates under the microscope as soon as they reached a size of 500 µm, typically 7 days after plating. Single colonies were then further expanded and screened for mutations in exon 3 by Sanger sequencing. Complete loss of MEIS1 protein was confirmed by western blotting, using a MEIS1-specific antibody (Abcam, ab19867).

4.2.6 Generation of cerebral organoids

Organoids were generated using the protocol previously described by Lancaster and Knoblich (2014a) with minor modifications: iPSC were dissociated to single cells using accutase and 9,000 cells per microwell (2.7 mio per plate) were plated in a Aggrewell 800 plate (StemCell Technologies) to increase homogeneity between individual organoids. Furthermore, we added 2.5 µM IWP2 (Sigma, cat. no. I0536) and 100 nM SAG (Millipore, cat. no. 566660) to the neural induction medium, as it promotes the formation of ventral cell identities (Bagley et al., 2017). Organoids were finally grown in 6-well plates on an orbital shaker until day 32.

4.2.7 Generation of lentivirus

Lenitvirus was used to transduct human neural stem cells, human neural progenitor cells and HEK293T cells in vitro.

Lentivirus was generated using the psPAX2 packaging and pMD2.G envelope plasmids along with a transfer plasmid encoding the target gene for integration. Lenti-X 293T cells (Takara Bio, CN 632180) were seeded 24 h prior to transfection,

onto 10 cm culture dishes at 6 Mio cells per dish. 1.5 µg pMD2.G, 4.5 µg psPAX2, 6 µg target vector were mixed with 600 µl Opti-MEM (Gibco, CN 11058021), 48 µl polyethyleneimine (PEI, 1 mg/ml, Polysciences CN 24765-1), mixed by inversion of the tube and incubated for 10-20 min at room temperature. The mixture was added dropwise to the culture dish and cells were incubated for 16 h at 37°C and 5% CO_2. Growth media was replaced and cells cultivated for another 2 days. Culture media containing lentivirus was harvested 72 h after transfection, centrifuged at 1200 xg for 5 min at 4°C. Supernatant was filtered with a 0.45 µm ploye thersulfone (PES) syringe filter. Virus was concentrated by sucrose gradient centrifugation: in a 15 ml centrifuge tube, 3 ml ice-cold sucrose buffer (10% (m/v) sucrose, 50 mM Tris-Cl pH 7.4, 100 mM NaCl, 0.5 mM EDTA) were carefully overlaid by pipetting with 9 ml filtered supernatant and centrifuged at 15,000 xg for 4 h at 4°C. Supernatant was carefully removed with a serological pipet and the lentiviral pellet was resuspended with DPBS and diluted to a total volume of 1 ml. Virus was stored at 4°C until infection of cells on the same day. Due to the instability of lentiviral particle, fresh virus was generated for each transduction.

4.2.8 Lentiviral infection of hNSC, NPC and 293T cells

hNSC, NPC or 293T cells were stably transduced by adding 5 µl concentrated viral supernatant (4.2.3.1), replacing culture media 16 h after infection. The lentiviral vectors expressed PPP1RC12-, MEIS1- or MEIS2-transcript-specific shRNAmir, along with the mRuby3 fluorescent reporter (Bajar et al., 2016). Cells were harvested for isolation of RNA or Protein 72h after infection. Transcript expression was determined by quantitative real-time PCR (qPCR), protein expression was measured by western blot.

4.3 Chromatin Immunoprecipitation sequencing (ChIP-seq)

4.3.1 Chromatin isolation

Nuclei from human neural stem cells (hNSC) were isolated by dissociating cells with Accutase (Sigma A6964) and washing with DPBS. Samples were henceforth processed with the truChIP™ Chromatin Shearing Kit (Covaris, PN 520154) according to the manufacturer's protocol (010179 Rev K, July 2017).

In brief, the resulting pellet was resuspended in fixation buffer before addition of formaldehyde (Thermo Scientific, #28908) to a final concentration of 1%. Samples were fixed for 5 min at room temperature while rotating. Processed nuclei were snap-frozen in liquid nitrogen and stored at -80°C, or were sonicated directly in a Covaris E220 Focused-Ultrasonicator in milliTUBE–1 mL with AFA Fiber, using nuclei from 30 Mio cells per tube. Samples were sonicated in TruChIP shearing buffer (10 mM Tris-Cl, 1 mM EDTA, 0.1% SDS) with 5% peak intensity power, 140 W, 200 cycles per burst for 2 min. Sheared chromatin was centrifuged at 10,000xg for 10 min at 4°C before decanting the supernatant. A 20 µl aliquot of the supernatant was taken to analyze fragment size distribution and DNA concentration. 20 µl supernatant were mixed with 1 µl RNAse A (10 µg/µl), 1 µl proteinase K (10 µg/µl) and 80µl elution buffer (1% SDS, 100 mM NaHCO3), incubated at 37°C for 10 min, 55°C for 10 min, 65°C for 3h. Cleanup was performed with MinElute PCR purification kit (Qiagen, 28004). Size distribution of DNA fragments was verified by running on a 1% agarose gel, DNA concentration of the was quantified using Quant-iT™ PicoGreen (Thermo Fisher Scientific, P7589) on a Cytation 3 microplate reader (Biotek).

4.3.2 Immunoprecipitation (IP)

Sheared chromatin was adjusted to dilution buffer (final concentration 20 mM Tris-Cl, 150 mM NaCl, 10 mM EDTA, 0.1% SDS, 1% Triton X-100, protease inhibitor) in a total volume of 5 ml. Samples were pre-cleared with 10 µl Dynabeads Protein-A beads (Invitrogen ,10001D) per 40 µl chromatin, by rotating for 4 h at 4°C. Sheared chromatin was then divided, matching 120 µg chromatin per sample. 1.5 µg of anti-MEISa K830 and 1.5 µg of anti-MEIS1 K844 were added to each sample, incubating for 16 h at 4°C on a rotator at 30 rpm. 4.1 µl magnetic Dynabeads Protein A beads per sample were washed 3 times in bead blocking solution (0.5% BSA in PBS) and incubated on a rotator beside the chromatin samples. The next day, chromatin was centrifuged at 3,000xg for 20 min at 4°C. Beads were washed 3 times, resuspended

in 80 µl (per sample) immunoprecipitation (IP) buffer (50 mM Tris-Cl pH7.5, 150 mM NaCl, 5 mM EDTA, 1% Triton X-100, 0.5% IGEPAL® CA-630) containing protease inhibitor and divided into single tubes. Supernatant from immunoprecipitated chromatin was added to beads, and rotated for 4 h at 4°C. At 4°C, beads were then washed 6x in IP Buffer or 5x in IP Buffer & 3x in IP Buffer + 250 mM LiCl (all without inhibitors), and 1x TE buffer pH 8.0. Samples were eluted from beads in 200 µl bead elution buffer (10% SDS, 100 mM $NaHCO_3$) for 30 min while shaking at room temperature. The supernatant was mixed with 8 µl 5M NaCl and de-crosslinked at 65°C over night. 4 µl RNase A (10 µg/µl) were added and samples incubated for 30 min at 37°C. Protein was digested by adding 4 µl EDTA, 8 µl 1M Tris-Cl and 4 µl proteinase K (10 µg/µl) and incubating at 55°C for 2h. DNA was then purified using the MinElute PCR purification kit (Qiagen, 28004), with 1 ml Buffer PB and 50 µl 3M NaOAc (pH 5.2). DNA was quantified using PicoGreen.
Input control samples of chromatin were taken after pre-cleaning with beads, and were de-crosslinked and purified along with immunoprecipitated samples

4.3.3 Enrichment by qPCR and library prep

In order to verify enrichment of DNA bound by MEIS transcription factors, qPCR was performed with site-specific primer pairs, spanning approximately 100 bp within known binding sites, as well as control primer pairs in unbound regions. The results of immunoprecipitated samples were compared against input control. If sufficient enrichment over input control was confirmed (>8-fold on average), libraries for Illumina sequencing were prepared.

4.3.4 Library preparation and sequencing

An Illumina sequencing library was generated using the NEBNext Ultra II Library Prep Kit for Illumina (E7645) with NEBNext Multiplex Oligos for Illumina (Dual Index Set1, E7600) according to the manufacturer's protocol. 12 PCR cycles were performed for Samples < 2 ng input, otherwise 11 cycles were used. Size selection was performed after PCR. Due to the amount of large fragments >1000 bp remaining, additional size selection was performed using a Pippin Prep (Sage Science), using a 2% cassette, size window 300-750 bp. Samples were sequenced 36bp paired-end on an Illumina NextSeq550.

4.4 Protein isolation and Western Blot

In vitro cultured cells washed in cold PBS and subsequently treated with ice-cold lysis buffer (150 mM NaCl, 0.5% Triton-X, 50 mM Tris-Cl pH 8.0, protease inhibitor) by agitating for 30 min at 4°C. Lysates were centrifuged at 10,000xg for 10 min at 4°C, and supernatants transferred to protein lo-bind tubes (Eppendorf). Protein concentration was determined by BSA standard curve, using the DC Protein Quantification Assay (Bio-Rad, 500-0116) according to the manufacturer's instructions, or downscaled to 1/4th of the volume. Absorption was measured on a NanoDrop One (Thermo Fisher Scientific) at 750 nm. Up to 30 µg protein per sample was used for western blot. Volume was adjusted to 15 µl with TBST before adding 3 µl 6x Lämmli Buffer (66 mM Tris-HCl, 10% SDS (w/v), 52% Glycerol (v/v), 100 mM DTT, 666 µg/ml Bromophenol blue) and boiling at 95 °C for 5 min.

Samples were loaded on 12% Mini-Protean TGX Gel (456-1095, Bio-Rad) in a Mini-Protean Tetra System (Bio-Rad). Gels were transferred semi-dry to nitrocellulose membranes using the Trans-Blot Turbo system (Bio-Rad).

Membranes were blocked in blocking buffer (5% Non-Fat Dry Milk (NFDM) in TBST) for 1h at room temperature. Primary antibodies were diluted 1:10,000 in blocking buffer, and membranes incubated for 16 h at 4°C, followed by three 10 min washing steps in TBST. Secondary antibodies were diluted 1:10,000 in blocking buffer, and membranes incubated for 1 h at room temperature, followed by three 10 min washing steps. ECL Prime WB Detection Reagent (Amersham, RPN2236) was used to visualize bands in a Fusion FX gel documentation system (Vilber).

4.5 Antibodies

Table 4.5.1: Primary antibodies used for western blot (WB), immunofluorescence (IF) and chromatin immunoprecipitation (ChIP-seq)

Primary Antibody	Provider	Cat. No / publication	Application
anti-BrdU	Abcam	ab6326	IF
anti-Ctip2	Abcam	ab18465	IF
anti-DCX	Abcam	ab198723	IF
anti-GSX2 (GSH2)	Merck-Millipore	ABN162	IF
anti-GAPDH	Sigma	G8795	WB
anti-Ki67	Merck-Millipore	MAB4190	IF
anti-MEIS1	M. Torres	Mercader 2005	ChIP-seq
anti-MEIS1	Abcam	ab19867	WB
anti-MEIS1/2/3	Merck-Millipore	05-779	IF
anti-MEIS2	M. Torres	Mercader 2005	IF/WB
anti-MEIS-a	M. Torres	Mercader 2005	ChIP-seq
anti-Nestin	Santa Cruz Biotechnology	sc-23927	IF
anti-Oct-3/4	Santa Cruz Biotechnology	sc-5279	IF
anti-PAX6	Biozol	BLD-901301	IF
anti-PHH3	Cell Signaling Technology	7906S	IF
anti-SOX2	Abcam	ab97959	IF
anti-TBR1	Abcam	ab31940	IF
anti-TBR2 (EOMES)	Abcam	ab23345	IF

Table 4.5.2 Secondary Antibodies used in immunofluorescence

Secondary Antibody	Provider	Cat. No / publication	Application
Anti-Mouse IgG AF488	Invitrogen	A21202	IF
Anti-Mouse IgG AF555	Invitrogen	A21424	IF
Anti-Rabbit IgG AF488	Invitrogen	A11034	IF
Anti-Rabbit IgG AF555	Invitrogen	A21428	IF

4.6 Mouse breeding and tissue preparation

All mouse work was performed in accordance with government regulations (§17 TierSchVersV) and the approved animal protocol ROB-55.2-2532.Vet_02-20-199 from the government of Upper Bavaria for the Helmholtz Zentrum München. Breeding was carried out by technicians of the ING and mouse facility of the Helmholtz

Zentrum München. Mice of the C57BL/6N-Meis1^{em1Bcca} line were bred to homozygosity. Pregnant female mice were euthanized by cervical dislocation, the uterus was dissected, and individual embryos subsequently decapitated. Embryo heads were fixed in 4% freshly prepared formaldehyde solution in PBS for 3h at 4°C, washed in PBS and immersed in 10% sucrose/PBS over night until sinking down. Heads were then embedded in sucrose/gelatin (10%/10%) and subsequently snap-frozen in isopentane cooled on dry ice between -60°C to -80°C. Frozen blocks were stored at -80°C and sectioned on a cryostat to sections of 20 µm. Cryosections were placed on glass slides and stored at -80°C.

4.7 Immunofluorescence staining

Cryosections on glass slides were warmed to room temperature and dried for 20 min before re-hydrating in PBS for 5 min. Sections were blocked for 1 h in blocking solution (0.1 % Triton X-100, 5% normal goat or donkey serum in PBS) at room temperature in a humidiefied chamber. Primary antibodies were diluted 1:500 in blocking solution, incubating the slides o/n at 4°C. Slides were washed 3x in wash buffer (0.5% Triton X-100 in PBS) for 10 min before applying secondary antibodies (1:500 in blocking buffer) for 2h at room temperature, protected from light. Slides were then incubated in 1 µg/ml DAPI for 3 min, and washed 2x10 min in wash buffer, 1x10 min in PBS before dipping in ddH_2O to remove remaining salts. Slides were mounted with Aqua-Poly/Mount (Polysciences).

4.8 Microscopy Imaging and analysis

In-vitro cultured hNSC were imaged using an Evos FL cell imaging system.
In-situ hybridizations of embryonic mouse brains were imaged on a Zeiss 880 upright laser scanning confocal microscope with 20x/0.8NA Plan-Apochromat (a=0.55 mm) objective using the ZEN Black v2.1 software (Zeiss). Individual images were subsequently stitched using the same software.
Immunostainings of embryonic mouse brains and in differentiated hNSC were recorded on a AxioScan 8 using a 20x/0.8NA Plan-Apochromat (a=0.55 mm) objective by the Core Facility Pathology & Tissue Analytics, Helmholtz-Zentrum München.
Images of hNSC stained for BrdU, PHH3 and Ki67 were analyzed with ImageJ (v 1.5.3a) using custom macros. Contours of nuclei were determined in the DAPI

channel, and integrated densities were measured in all channels, followed by background subtraction. The threshold determining positive from negative cells was distinguished for each image, by manually selecting 20 positive cells while being blinded to the treatment of the cells. The ratio of positive to negative cells was calculated for each image, used to compare shRNA-treatments by Welch's T-test.

4.9 Bioinformatic analyses

Bioinformatic analysis programs were executed in R (v4.0.1) using custom scripts. Custom plots were constructed using ggplot (v3.3.2). R functions and command line programs were used with default parameters, unless stated otherwise.

Read processing
Adapters were trimmed from raw reads using cutadapt (v1.16), without quality-based trimming. Reads were mapped to the human genome assembly GRCh37 (hg19) using bowtie2 (v2.3.0) and samtools (v1.2) at a cutoff of mapq >=30. PCR duplicates were removed with Picard tools (v 2.15.0).

Peak calling
Peaks were called using MACS2 (v. 2.1.2) in paired-end mode whenever possible, using input samples as background control.

Irreproducible discovery rate (IDR)
IDR (v.2.0.3, Li et al., 2011) was used for all samples to determine reproducible peaks between replicates. Peaks called by MACS2 with a P-value cut-off of 0.01 were used as input. If only one replicate was given, self-replicates were generated by splitting filtered reads in two groups, then performing peak calling individually with MACS2, followed by IDR analysis.

FRiP
Fraction of reads in peaks (FRiP) is determined by counting the fraction of filtered reads that fall within peak regions, determined by MACS2 (cutoff q = 0.01). The value was calculated for each replicate independently, and averaged for each experiment.

Peak annotation and characterization
For experiments in mouse tisse, coordinates were converted from GRCm38 (mm10) to GRCh37 (hg19) using the R installation of LiftOver (rtracklayer v1.50.0). Peaks from different datasets were overlapped using plyranges (v1.8.0) with a minimal overlap of 1bp. ChIP-seq peaks with a minimal overlap of 1 bp were merged to generate a global peak list. Peak overlaps were visualized using upsetR (v1.4.0). Peaks were assigned to the nearest TSS of UCSC known genes within 1 Mb using the R package ChIPseeker (v1.18.0). These were considered direct target genes when a peak was located within 5 kb of a TSS. Direct target genes were used as

input for overrepresentation analysis performed by clusterProfiler (v3.1.6), with gene sets of the REACTOME pathway.

Motif analysis

Motif Analyses were performed using the MEME-suite web tool (www.meme-suite.org), individual functions were called within the MEME-ChIP program (v5.1.1), using default settings, with 200 bp windows centered on peak summits as input sequences. JASPAR core collection (2018) was selected for reference motifs.
De-novo motif discovery within MEIS binding sites was performed using the unbiased search algorithm MEME (Bailey and Elkan, 1994), which scans for recurring DNA motifs a list of DNA sequences, using 100 bp windows centred on the maximum of each ChIP-seq peak. All peaks were used for motif discovery, and the 10 highest scoring, centrally enriched motifs were reported. Analysis of motif enrichment and distribution within peak centers was performed by CentriMo (Bailey and Machanick, 2012). Previously unknown moitfs were compared to the JASPAR motif database using TOMTOM (Gupta et al., 2007). Position, strand and orientation of motifs was determined using FIMO (Grant et al., 2011).

S-LDSC

*S*tratified LD score regression (S-LDSC) was used to perform partitioned heritability analyses using LDSC(v1.01) as previously described (Finucane et al., 2015, Schormair et al., 2017). I used code previously implemented on the institute server to be used with variable datasets (GWAS summary statistics, genomic region files).

References

Agoston, Z., and Schulte, D. (2009). Meis2 competes with the Groucho co-repressor Tle4 for binding to Otx2 and specifies tectal fate without induction of a secondary midbrain-hindbrain boundary organizer. Development *136*, 3311-3322.

Agoston, Z., Li, N., Haslinger, A., Wizenmann, A., and Schulte, D. (2012). Genetic and physical interaction of Meis2, Pax3 and Pax7 during dorsal midbrain development. BMC Dev Biol *12*, 10.

Agoston, Z., Heine, P., Brill, M.S., Grebbin, B.M., Hau, A.C., Kallenborn-Gerhardt, W., Schramm, J., Gotz, M., and Schulte, D. (2014). Meis2 is a Pax6 co-factor in neurogenesis and dopaminergic periglomerular fate specification in the adult olfactory bulb. Development *141*, 28-38.

Allen, R.P., Barker, P.B., Wehrl, F.W., Song, H.K., and Earley, C.J. (2001). MRI measurement of brain iron in patients with restless legs syndrome. Neurology *56*, 263-265.

Allen, R.P., Walters, A.S., Montplaisir, J., Hening, W., Myers, A., Bell, T.J., and Ferini-Strambi, L. (2005). Restless legs syndrome prevalence and impact: REST general population study. Arch Intern Med *165*, 1286-1292.

Allen, R.P., Stillman, P., and Myers, A.J. (2010). Physician-diagnosed restless legs syndrome in a large sample of primary medical care patients in western Europe: Prevalence and characteristics. Sleep Med *11*, 31-37.

Allen, R.P., Bharmal, M., and Calloway, M. (2011). Prevalence and disease burden of primary restless legs syndrome: results of a general population survey in the United States. Mov Disord *26*, 114-120.

Anderson, S.A., Marin, O., Horn, C., Jennings, K., and Rubenstein, J.L. (2001). Distinct cortical migrations from the medial and lateral ganglionic eminences. Development *128*, 353-363.

Antosova, B., Smolikova, J., Klimova, L., Lachova, J., Bendova, M., Kozmikova, I., Machon, O., and Kozmik, Z. (2016). The Gene Regulatory Network of Lens Induction Is Wired through Meis-Dependent Shadow Enhancers of Pax6. PLoS Genet *12*, e1006441.

Arlotta, P., Molyneaux, B.J., Chen, J., Inoue, J., Kominami, R., and Macklis, J.D. (2005). Neuronal subtype-specific genes that control corticospinal motor neuron development in vivo. Neuron *45*, 207-221.

Arlotta, P., Molyneaux, B.J., Jabaudon, D., Yoshida, Y., and Macklis, J.D. (2008). Ctip2 controls the differentiation of medium spiny neurons and the establishment of the cellular architecture of the striatum. J Neurosci *28*, 622-632.

Astrakas, L.G., Konitsiotis, S., Margariti, P., Tsouli, S., Tzarouhi, L., and Argyropoulou, M.I. (2008). T2 relaxometry and fMRI of the brain in late-onset restless legs syndrome. Neurology *71*, 911-916.

Bagley, J.A., Reumann, D., Bian, S., Levi-Strauss, J., and Knoblich, J.A. (2017). Fused cerebral organoids model interactions between brain regions. Nat Methods *14*, 743-751.

Bai, J., Ramos, R.L., Paramasivam, M., Siddiqi, F., Ackman, J.B., and LoTurco, J.J. (2008). The role of DCX and LIS1 in migration through the lateral cortical stream of developing forebrain. Dev Neurosci *30*, 144-156.

Bailey, T.L., and Elkan, C. (1994). Fitting a mixture model by expectation maximization to discover motifs in biopolymers. Proc Int Conf Intell Syst Mol Biol *2*, 28-36.

Bailey, T.L., and Machanick, P. (2012). Inferring direct DNA binding from ChIP-seq. Nucleic Acids Res *40*, e128.

Bajar, B.T., Wang, E.S., Lam, A.J., Kim, B.B., Jacobs, C.L., Howe, E.S., Davidson, M.W., Lin, M.Z., and Chu, J. (2016). Improving brightness and photostability of green and red fluorescent proteins for live cell imaging and FRET reporting. Sci Rep *6*, 20889.

Baran, R.T., Atar, M., Pirgon, O., Filiz, S., and Filiz, M. (2018). Restless Legs Syndrome and Poor Sleep Quality in Obese Children and Adolescents. J Clin Res Pediatr Endocrinol *10*, 131-138.

Barber, B.A., Liyanage, V.R., Zachariah, R.M., Olson, C.O., Bailey, M.A., and Rastegar, M. (2013). Dynamic expression of MEIS1 homeoprotein in E14.5 forebrain and differentiated forebrain-derived neural stem cells. Ann Anat *195*, 431-440.

Batista-Brito, R., Machold, R., Klein, C., and Fishell, G. (2008). Gene expression in cortical interneuron precursors is prescient of their mature function. Cereb Cortex *18*, 2306-2317.

Bauernfeind, A.L., and Babbitt, C.C. (2017). The predictive nature of transcript expression levels on protein expression in adult human brain. BMC Genomics *18*, 322.

Berthelsen, J., Kilstrup-Nielsen, C., Blasi, F., Mavilio, F., and Zappavigna, V. (1999). The subcellular localization of PBX1 and EXD proteins depends on nuclear import and export signals and is modulated by association with PREP1 and HTH. Genes Dev *13*, 946-953.

Bessa, J., Tavares, M.J., Santos, J., Kikuta, H., Laplante, M., Becker, T.S., Gomez-Skarmeta, J.L., and Casares, F. (2008). meis1 regulates cyclin D1 and c-myc expression, and controls the proliferation of the multipotent cells in the early developing zebrafish eye. Development *135*, 799-803.

Beuter, S., Ardi, Z., Horovitz, O., Wuchter, J., Keller, S., Saha, R., Tripathi, K., Anunu, R., Kehat, O., Kriebel, M.*, et al.* (2016). Receptor tyrosine kinase EphA7 is required for interneuron connectivity at specific subcellular compartments of granule cells. Sci Rep *6*, 29710.

Blasi, F., Bruckmann, C., Penkov, D., and Dardaei, L. (2017). A tale of TALE, PREP1, PBX1, and MEIS1: Interconnections and competition in cancer. Bioessays *39*.

Bocchi, R., Egervari, K., Carol-Perdiguer, L., Viale, B., Quairiaux, C., De Roo, M., Boitard, M., Oskouie, S., Salmon, P., and Kiss, J.Z. (2017). Perturbed Wnt signaling leads to neuronal migration delay, altered interhemispheric connections and impaired social behavior. Nat Commun *8*, 1158.

Bonner, W.A., Hulett, H.R., Sweet, R.G., and Herzenberg, L.A. (1972). Fluorescence activated cell sorting. Rev Sci Instrum *43*, 404-409.

Bouilloux, F., Thireau, J., Venteo, S., Farah, C., Karam, S., Dauvilliers, Y., Valmier, J., Copeland, N.G., Jenkins, N.A., Richard, S.*, et al.* (2016). Loss of the transcription factor Meis1 prevents sympathetic neurons target-field innervation and increases susceptibility to sudden cardiac death. Elife *5*.

Bridge, A.J., Pebernard, S., Ducraux, A., Nicoulaz, A.L., and Iggo, R. (2003). Induction of an interferon response by RNAi vectors in mammalian cells. Nat Genet *34*, 263-264.

Bryja, V., Cervenka, I., and Cajanek, L. (2017). The connections of Wnt pathway components with cell cycle and centrosome: side effects or a hidden logic? Crit Rev Biochem Mol Biol *52*, 614-637.

Bucher, S.F., Seelos, K.C., Oertel, W.H., Reiser, M., and Trenkwalder, C. (1997). Cerebral generators involved in the pathogenesis of the restless legs syndrome. Ann Neurol *41*, 639-645.

Calvo, K.R., Knoepfler, P., McGrath, S., and Kamps, M.P. (1999). An inhibitory switch derepressed by pbx, hox, and Meis/Prep1 partners regulates DNA-binding by pbx1 and E2a-pbx1 and is dispensable for myeloid immortalization by E2a-pbx1. Oncogene *18*, 8033-8043.

Canovas, J., Berndt, F.A., Sepulveda, H., Aguilar, R., Veloso, F.A., Montecino, M., Oliva, C., Maass, J.C., Sierralta, J., and Kukuljan, M. (2015). The Specification of Cortical Subcerebral Projection Neurons Depends on the Direct Repression of TBR1 by CTIP1/BCL11a. J Neurosci *35*, 7552-7564.

Cansler, H.L., Wright, K.N., Stetzik, L.A., and Wesson, D.W. (2020). Neurochemical organization of the ventral striatum's olfactory tubercle. J Neurochem *152*, 425-448.

Cao, J., Spielmann, M., Qiu, X., Huang, X., Ibrahim, D.M., Hill, A.J., Zhang, F., Mundlos, S., Christiansen, L., Steemers, F.J.*, et al.* (2019). The single-cell transcriptional landscape of mammalian organogenesis. Nature *566*, 496-502.

Carney, R.S., Alfonso, T.B., Cohen, D., Dai, H., Nery, S., Stoica, B., Slotkin, J., Bregman, B.S., Fishell, G., and Corbin, J.G. (2006). Cell migration along the lateral cortical stream to the developing basal telencephalic limbic system. J Neurosci *26*, 11562-11574.

Catoire, H., Dion, P.A., Xiong, L., Amari, M., Gaudet, R., Girard, S.L., Noreau, A., Gaspar, C., Turecki, G., Montplaisir, J.Y.*, et al.* (2011). Restless legs syndrome-associated MEIS1 risk variant influences iron homeostasis. Ann Neurol *70*, 170-175.

Ceci, M.L., Pedraza, M., and de Carlos, J.A. (2012). The embryonic septum and ventral pallium, new sources of olfactory cortex cells. PLoS One *7*, e44716.

Chang, C.P., Jacobs, Y., Nakamura, T., Jenkins, N.A., Copeland, N.G., and Cleary, M.L. (1997). Meis proteins are major in vivo DNA binding partners for wild-type but not chimeric Pbx proteins. Mol Cell Biol *17*, 5679-5687.

Chen, B., Wang, S.S., Hattox, A.M., Rayburn, H., Nelson, S.B., and McConnell, S.K. (2008). The Fezf2-Ctip2 genetic pathway regulates the fate choice of subcortical projection neurons in the developing cerebral cortex. Proc Natl Acad Sci U S A *105*, 11382-11387.

Clifford, M.A., Athar, W., Leonard, C.E., Russo, A., Sampognaro, P.J., Van der Goes, M.S., Burton, D.A., Zhao, X., Lalchandani, R.R., Sahin, M.*, et al.* (2014). EphA7 signaling guides cortical dendritic development and spine maturation. Proc Natl Acad Sci U S A *111*, 4994-4999.

Close, J.L., Yao, Z., Levi, B.P., Miller, J.A., Bakken, T.E., Menon, V., Ting, J.T., Wall, A., Krostag, A.R., Thomsen, E.R.*, et al.* (2017). Single-Cell Profiling of an In Vitro Model of Human Interneuron Development Reveals Temporal Dynamics of Cell Type Production and Maturation. Neuron *96*, 949.

Connor, J.R., Wang, X.S., Allen, R.P., Beard, J.L., Wiesinger, J.A., Felt, B.T., and Earley, C.J. (2009). Altered dopaminergic profile in the putamen and substantia nigra in restless leg syndrome. Brain *132*, 2403-2412.

Dardaei, L., Penkov, D., Mathiasen, L., Bora, P., Morelli, M.J., and Blasi, F. (2015). Tumorigenesis by Meis1 overexpression is accompanied by a change of DNA target-sequence specificity which allows binding to the AP-1 element. Oncotarget *6*, 25175-25187.

Desautels, A., Turecki, G., Montplaisir, J., Xiong, L., Walters, A.S., Ehrenberg, B.L., Brisebois, K., Desautels, A.K., Gingras, Y., Johnson, W.G., et al. (2005). Restless legs syndrome: confirmation of linkage to chromosome 12q, genetic heterogeneity, and evidence of complexity. Arch Neurol 62, 591-596.

Doeppner, T.R., Herz, J., Bahr, M., Tonchev, A.B., and Stoykova, A. (2019). Zbtb20 Regulates Developmental Neurogenesis in the Olfactory Bulb and Gliogenesis After Adult Brain Injury. Mol Neurobiol *56*, 567-582.

Domcke, S., Hill, A.J., Daza, R.M., Cao, J., O'Day, D.R., Pliner, H.A., Aldinger, K.A., Pokholok, D., Zhang, F., Milbank, J.H.*, et al.* (2020). A human cell atlas of fetal chromatin accessibility. Science *370*.

Duboule, D. (2007). The rise and fall of Hox gene clusters. Development *134*, 2549-2560.

Dupacova, N., Antosova, B., Paces, J., and Kozmik, Z. (2021). Meis homeobox genes control progenitor competence in the retina. Proc Natl Acad Sci U S A 118.

Dvoretskova, E., Ho, M.C., Kittke, V., Neuhaus, F., Vitali, I., Lam, D.D., Delgado, I., Feng, C., Torres, M., Winkelmann, J., et al. (2024). Spatial enhancer activation influences inhibitory neuron identity during mouse embryonic development. Nat Neurosci.

Earley, C.J., P, B.B., Horska, A., and Allen, R.P. (2006). MRI-determined regional brain iron concentrations in early- and late-onset restless legs syndrome. Sleep Med *7*, 458-461.

Earley, C.J., Kuwabara, H., Wong, D.F., Gamaldo, C., Salas, R., Brasic, J., Ravert, H.T., Dannals, R.F., and Allen, R.P. (2011). The dopamine transporter is decreased in the striatum of subjects with restless legs syndrome. Sleep *34*, 341-347.

Earley, C.J., Kuwabara, H., Wong, D.F., Gamaldo, C., Salas, R.E., Brasic, J.R., Ravert, H.T., Dannals, R.F., and Allen, R.P. (2013). Increased synaptic dopamine in the putamen in restless legs syndrome. Sleep *36*, 51-57.

Earley, C.J., Uhl, G.R., Clemens, S., and Ferre, S. (2017). Connectome and molecular pharmacological differences in the dopaminergic system in restless legs syndrome (RLS): plastic changes and neuroadaptations that may contribute to augmentation. Sleep Med *31*, 71-77.

Ekbom, K.A. (1960). Restless legs syndrome. Neurology *10*, 868-873.

ENCODE Project Consortium. (2012). An integrated encyclopedia of DNA elements in the human genome. Nature *489*, 57-74.

Englund, C., Fink, A., Lau, C., Pham, D., Daza, R.A., Bulfone, A., Kowalczyk, T., and Hevner, R.F. (2005). Pax6, Tbr2, and Tbr1 are expressed sequentially by radial glia, intermediate progenitor cells, and postmitotic neurons in developing neocortex. J Neurosci *25*, 247-251.

Fellmann, C., Hoffmann, T., Sridhar, V., Hopfgartner, B., Muhar, M., Roth, M., Lai, D.Y., Barbosa, I.A., Kwon, J.S., Guan, Y.*, et al.* (2013). An optimized microRNA backbone for effective single-copy RNAi. Cell Rep *5*, 1704-1713.

Ferretti, E., Marshall, H., Popperl, H., Maconochie, M., Krumlauf, R., and Blasi, F. (2000). Segmental expression of Hoxb2 in r4 requires two separate sites that integrate cooperative interactions between Prep1, Pbx and Hox proteins. Development *127*, 155-166.

Figeys, D., McBroom, L.D., and Moran, M.F. (2001). Mass spectrometry for the study of protein-protein interactions. Methods *24*, 230-239.

Finucane, H.K., Bulik-Sullivan, B., Gusev, A., Trynka, G., Reshef, Y., Loh, P.R., Anttila, V., Xu, H., Zang, C., Farh, K.*, et al.* (2015). Partitioning heritability by functional annotation using genome-wide association summary statistics. Nat Genet *47*, 1228-1235.

Fire, A., Xu, S., Montgomery, M.K., Kostas, S.A., Driver, S.E., and Mello, C.C. (1998). Potent and specific genetic interference by double-stranded RNA in Caenorhabditis elegans. Nature *391*, 806-811.

Fornes, O., Castro-Mondragon, J.A., Khan, A., van der Lee, R., Zhang, X., Richmond, P.A., Modi, B.P., Correard, S., Gheorghe, M., Baranasic, D.*, et al.* (2020). JASPAR 2020: update of the open-access database of transcription factor binding profiles. Nucleic Acids Res *48*, D87-D92.

Gao, X., Schwarzschild, M.A., Wang, H., and Ascherio, A. (2009). Obesity and restless legs syndrome in men and women. Neurology *72*, 1255-1261.

Garcia-Borreguero, D., Stillman, P., Benes, H., Buschmann, H., Chaudhuri, K.R., Gonzalez Rodriguez, V.M., Hogl, B., Kohnen, R., Monti, G.C., Stiasny-Kolster, K.*, et al.* (2011). Algorithms for the diagnosis and treatment of restless legs syndrome in primary care. BMC Neurol *11*, 28.

Garcia-Moreno, F., Lopez-Mascaraque, L., and de Carlos, J.A. (2008). Early telencephalic migration topographically converging in the olfactory cortex. Cereb Cortex *18*, 1239-1252.

Ghanem, N., Yu, M., Poitras, L., Rubenstein, J.L., and Ekker, M. (2008). Characterization of a distinct subpopulation of striatal projection neurons expressing the Dlx genes in the basal ganglia through the activity of the I56ii enhancer. Dev Biol *322*, 415-424.

Gibson, G. (2012). Rare and common variants: twenty arguments. Nat Rev Genet *13*, 135-145.

Godau, J., Klose, U., Di Santo, A., Schweitzer, K., and Berg, D. (2008). Multiregional brain iron deficiency in restless legs syndrome. Mov Disord *23*, 1184-1187.

Golonzhka, O., Nord, A., Tang, P.L.F., Lindtner, S., Ypsilanti, A.R., Ferretti, E., Visel, A., Selleri, L., and Rubenstein, J.L.R. (2015). Pbx Regulates Patterning of the Cerebral Cortex in Progenitors and Postmitotic Neurons. Neuron *88*, 1192-1207.

Grant, C.E., Bailey, T.L., and Noble, W.S. (2011). FIMO: scanning for occurrences of a given motif. Bioinformatics *27*, 1017-1018.

Gross, A., Schulz, C., Kolb, J., Koster, J., Wehner, S., Czaplinski, S., Khilan, A., Rohrer, H., Harter, P.N., Klingebiel, T.*, et al.* (2018). Tumorigenic and Antiproliferative Properties of the TALE-Transcription Factors MEIS2D and MEIS2A in Neuroblastoma. Cancer Res *78*, 1935-1947.

Gupta, S., Stamatoyannopoulos, J.A., Bailey, T.L., and Noble, W.S. (2007). Quantifying similarity between motifs. Genome Biol *8*, R24.

Hau, A.C., Grebbin, B.M., Agoston, Z., Anders-Maurer, M., Muller, T., Gross, A., Kolb, J., Langer, J.D., Doring, C., and Schulte, D. (2017). MEIS homeodomain proteins facilitate PARP1/ARTD1-mediated eviction of histone H1. J Cell Biol *216*, 2715-2729.

Heine, P., Dohle, E., Bumsted-O'Brien, K., Engelkamp, D., and Schulte, D. (2008). Evidence for an evolutionary conserved role of homothorax/Meis1/2 during vertebrate retina development. Development *135*, 805-811.

Hening, W., Walters, A.S., Allen, R.P., Montplaisir, J., Myers, A., and Ferini-Strambi, L. (2004). Impact, diagnosis and treatment of restless legs syndrome (RLS) in a primary care population: the REST (RLS epidemiology, symptoms, and treatment) primary care study. Sleep Med *5*, 237-246.

Hirabayashi, Y., Itoh, Y., Tabata, H., Nakajima, K., Akiyama, T., Masuyama, N., and Gotoh, Y. (2004). The Wnt/beta-catenin pathway directs neuronal differentiation of cortical neural precursor cells. Development *131*, 2791-2801.

Hu, J., Liao, J., Sathanoori, M., Kochmar, S., Sebastian, J., Yatsenko, S.A., and Surti, U. (2015). CNTN6 copy number variations in 14 patients: a possible candidate gene for neurodevelopmental and neuropsychiatric disorders. J Neurodev Disord *7*, 26.

Huang, H., Rastegar, M., Bodner, C., Goh, S.L., Rambaldi, I., and Featherstone, M. (2005). MEIS C termini harbor transcriptional activation domains that respond to cell signaling. J Biol Chem *280*, 10119-10127.

Hyman-Walsh, C., Bjerke, G.A., and Wotton, D. (2010). An autoinhibitory effect of the homothorax domain of Meis2. FEBS J *277*, 2584-2597.

Ivashkiv, L.B., and Donlin, L.T. (2014). Regulation of type I interferon responses. Nat Rev Immunol *14*, 36-49.

Jansen, P.R., Watanabe, K., Stringer, S., Skene, N., Bryois, J., Hammerschlag, A.R., de Leeuw, C.A., Benjamins, J.S., Munoz-Manchado, A.B., Nagel, M.*, et al.* (2019). Genome-wide analysis of insomnia in 1,331,010 individuals identifies new risk loci and functional pathways. Nat Genet *51*, 394-403.

Jassal, B., Matthews, L., Viteri, G., Gong, C., Lorente, P., Fabregat, A., Sidiropoulos, K., Cook, J., Gillespie, M., Haw, R.*, et al.* (2020). The reactome pathway knowledgebase. Nucleic Acids Res *48*, D498-D503.

Jinek, M., Chylinski, K., Fonfara, I., Hauer, M., Doudna, J.A., and Charpentier, E. (2012). A programmable dual-RNA-guided DNA endonuclease in adaptive bacterial immunity. Science *337*, 816-821.

Jones, K.A., Luo, Y., Dukes-Rimsky, L., Srivastava, D.P., Koul-Tewari, R., Russell, T.A., Shapiro, L.P., Srivastava, A.K., and Penzes, P. (2018). Neurodevelopmental disorder-associated ZBTB20 gene variants affect dendritic and synaptic structure. PLoS One *13*, e0203760.

Jung, I., Schmitt, A., Diao, Y., Lee, A.J., Liu, T., Yang, D., Tan, C., Eom, J., Chan, M., Chee, S.*, et al.* (2019). A compendium of promoter-centered long-range chromatin interactions in the human genome. Nat Genet *51*, 1442-1449.

Kerr, J.F., Wyllie, A.H., and Currie, A.R. (1972). Apoptosis: a basic biological phenomenon with wide-ranging implications in tissue kinetics. Br J Cancer *26*, 239-257.

Kim, J.Y., Jeong, H.S., Chung, T., Kim, M., Lee, J.H., Jung, W.H., and Koo, J.S. (2017). The value of phosphohistone H3 as a proliferation marker for evaluating invasive breast cancers: A comparative study with Ki67. Oncotarget *8*, 65064-65076.

Knoepfler, P.S., Calvo, K.R., Chen, H., Antonarakis, S.E., and Kamps, M.P. (1997). Meis1 and pKnox1 bind DNA cooperatively with Pbx1 utilizing an interaction surface disrupted in oncoprotein E2a-Pbx1. Proc Natl Acad Sci U S A *94*, 14553-14558.

Koo, B.B., Bagai, K., and Walters, A.S. (2016). Restless Legs Syndrome: Current Concepts about Disease Pathophysiology. Tremor Other Hyperkinet Mov (N Y) *6*, 401.

Lai, C.K., Norddahl, G.L., Maetzig, T., Rosten, P., Lohr, T., Sanchez Milde, L., von Krosigk, N., Docking, T.R., Heuser, M., Karsan, A.*, et al.* (2017). Meis2 as a critical player in MN1-induced leukemia. Blood Cancer J *7*, e613.

Lam, D.D., Antic Nikolic, A., Zhao, C., Mirza-Schreiber, N., Krezel, W., Oexle, K., and Winkelmann, J. (2022). Intronic elements associated with insomnia and restless legs syndrome exhibit cell-type-specific epigenetic features contributing to MEIS1 regulation. Hum Mol Genet 31, 1733-1746.

Lancaster, M.A., Renner, M., Martin, C.A., Wenzel, D., Bicknell, L.S., Hurles, M.E., Homfray, T., Penninger, J.M., Jackson, A.P., and Knoblich, J.A. (2013). Cerebral organoids model human brain development and microcephaly. Nature *501*, 373-379.

Lancaster, M.A., and Knoblich, J.A. (2014a). Generation of cerebral organoids from human pluripotent stem cells. Nat Protoc *9*, 2329-2340.

Lancaster, M.A., and Knoblich, J.A. (2014b). Organogenesis in a dish: modeling development and disease using organoid technologies. Science *345*, 1247125.

Landt, S.G., Marinov, G.K., Kundaje, A., Kheradpour, P., Pauli, F., Batzoglou, S., Bernstein, B.E., Bickel, P., Brown, J.B., Cayting, P.*, et al.* (2012). ChIP-seq guidelines and practices of the ENCODE and modENCODE consortia. Genome Res *22*, 1813-1831.

Leid, M., Ishmael, J.E., Avram, D., Shepherd, D., Fraulob, V., and Dolle, P. (2004). CTIP1 and CTIP2 are differentially expressed during mouse embryogenesis. Gene Expr Patterns *4*, 733-739.

Li, Q.H., Brown, J.B., Huang, H.Y., and Bickel, P.J. (2011). Measuring Reproducibility of High-Throughput Experiments. Ann Appl Stat *5*, 1752-1779.

Lin, L., Huang, M., Shi, X., Mayakonda, A., Hu, K., Jiang, Y.Y., Guo, X., Chen, L., Pang, B., Doan, N.*, et al.* (2019). Super-enhancer-associated MEIS1 promotes transcriptional dysregulation in Ewing sarcoma in co-operation with EWS-FLI1. Nucleic Acids Res *47*, 1255-1267.

Liu, Y., Liu, H., Sauvey, C., Yao, L., Zarnowska, E.D., and Zhang, S.C. (2013). Directed differentiation of forebrain GABA interneurons from human pluripotent stem cells. Nat Protoc 8, 1670-1679.

Loh, P.R., Bhatia, G., Gusev, A., Finucane, H.K., Bulik-Sullivan, B.K., Pollack, S.J., Schizophrenia Working Group of Psychiatric Genomics, C., de Candia, T.R., Lee, S.H., Wray, N.R.*, et al.* (2015). Contrasting genetic architectures of schizophrenia and other complex diseases using fast variance-components analysis. Nat Genet *47*, 1385-1392.

Longobardi, E., Penkov, D., Mateos, D., De Florian, G., Torres, M., and Blasi, F. (2014). Biochemistry of the tale transcription factors PREP, MEIS, and PBX in vertebrates. Dev Dyn *243*, 59-75.

Ma, L., Wang, Y., Hui, Y., Du, Y., Chen, Z., Feng, H., Zhang, S., Li, N., Song, J., Fang, Y.*, et al.* (2019). WNT/NOTCH Pathway Is Essential for the Maintenance and Expansion of Human MGE Progenitors. Stem Cell Reports *12*, 934-949.

Machon, O., Masek, J., Machonova, O., Krauss, S., and Kozmik, Z. (2015). Meis2 is essential for cranial and cardiac neural crest development. BMC Dev Biol *15*, 40.

Maeda, R., Mood, K., Jones, T.L., Aruga, J., Buchberg, A.M., and Daar, I.O. (2001). Xmeis1, a protooncogene involved in specifying neural crest cell fate in Xenopus embryos. Oncogene *20*, 1329-1342.

Mahe, E.A., Madigou, T., Serandour, A.A., Bizot, M., Avner, S., Chalmel, F., Palierne, G., Metivier, R., and Salbert, G. (2017). Cytosine modifications modulate the chromatin architecture of transcriptional enhancers. Genome Res *27*, 947-958.

Maher, B. (2008). Personal genomes: The case of the missing heritability. Nature *456*, 18-21.

Mahmoud, A.I., Kocabas, F., Muralidhar, S.A., Kimura, W., Koura, A.S., Thet, S., Porrello, E.R., and Sadek, H.A. (2013). Meis1 regulates postnatal cardiomyocyte cell cycle arrest. Nature *497*, 249-253.

Maintainer, B.P. (2020). liftOver: Changing genomic coordinate systems with rtracklayer::liftOver.

Marcos, S., Gonzalez-Lazaro, M., Beccari, L., Carramolino, L., Martin-Bermejo, M.J., Amarie, O., Mateos-San Martin, D., Torroja, C., Bogdanovic, O., Doohan, R.*, et al.* (2015). Meis1 coordinates a network of genes implicated in eye development and microphthalmia. Development *142*, 3009-+.

Margariti, P.N., Astrakas, L.G., Tsouli, S.G., Hadjigeorgiou, G.M., Konitsiotis, S., and Argyropoulou, M.I. (2012). Investigation of unmedicated early onset restless legs syndrome by voxel-based morphometry, T2 relaxometry, and functional MR imaging during the night-time hours. AJNR Am J Neuroradiol *33*, 667-672.

Marin, O., and Rubenstein, J.L. (2001). A long, remarkable journey: tangential migration in the telencephalon. Nat Rev Neurosci *2*, 780-790.

Marin, O., Yaron, A., Bagri, A., Tessier-Lavigne, M., and Rubenstein, J.L. (2001). Sorting of striatal and cortical interneurons regulated by semaphorin-neuropilin interactions. Science *293*, 872-875.

Marin, O. (2013). Cellular and molecular mechanisms controlling the migration of neocortical interneurons. Eur J Neurosci *38*, 2019-2029.

Martin-Lopez, E., Xu, C., Liberia, T., Meller, S.J., and Greer, C.A. (2019). Embryonic and postnatal development of mouse olfactory tubercle. Mol Cell Neurosci *98*, 82-96.

Mathias, R.A., Hening, W., Washburn, M., Allen, R.P., Lesage, S., Wilson, A.F., and Earley, C.J. (2006). Segregation analysis of restless legs syndrome: possible evidence for a major gene in a family study using blinded diagnoses. Hum Hered *62*, 157-164.

Meneely, S., Dinkins, M.L., Kassai, M., Lyu, S., Liu, Y., Lin, C.T., Brewer, K., Li, Y., and Clemens, S. (2018). Differential Dopamine D1 and D3 Receptor Modulation and Expression in the Spinal Cord of Two Mouse Models of Restless Legs Syndrome. Front Behav Neurosci *12*, 199.

Mercader, N., Leonardo, E., Piedra, M.E., Martinez, A.C., Ros, M.A., and Torres, M. (2000). Opposing RA and FGF signals control proximodistal vertebrate limb development through regulation of Meis genes. Development *127*, 3961-3970.

Mercati, O., Huguet, G., Danckaert, A., Andre-Leroux, G., Maruani, A., Bellinzoni, M., Rolland, T., Gouder, L., Mathieu, A., Buratti, J.*, et al.* (2017). CNTN6 mutations are risk factors for abnormal auditory sensory perception in autism spectrum disorders. Mol Psychiatry *22*, 625-633.

Moskow, J.J., Bullrich, F., Huebner, K., Daar, I.O., and Buchberg, A.M. (1995). Meis1, a PBX1-related homeobox gene involved in myeloid leukemia in BXH-2 mice. Mol Cell Biol *15*, 5434-5443.

Mucsi, I., Molnar, M.Z., Ambrus, C., Szeifert, L., Kovacs, A.Z., Zoller, R., Barotfi, S., Remport, A., and Novak, M. (2005). Restless legs syndrome, insomnia and quality of life in patients on maintenance dialysis. Nephrol Dial Transplant *20*, 571-577.

Nagano, T., Yoneda, T., Hatanaka, Y., Kubota, C., Murakami, F., and Sato, M. (2002). Filamin A-interacting protein (FILIP) regulates cortical cell migration out of the ventricular zone. Nat Cell Biol *4*, 495-501.

Nagano, T., Morikubo, S., and Sato, M. (2004). Filamin A and FILIP (Filamin A-Interacting Protein) regulate cell polarity and motility in neocortical subventricular and intermediate zones during radial migration. J Neurosci *24*, 9648-9657.

Nagao, M., Ogata, T., Sawada, Y., and Gotoh, Y. (2016). Zbtb20 promotes astrocytogenesis during neocortical development. Nat Commun *7*, 11102.

Nielsen, J.V., Blom, J.B., Noraberg, J., and Jensen, N.A. (2010). Zbtb20-induced CA1 pyramidal neuron development and area enlargement in the cerebral midline cortex of mice. Cereb Cortex *20*, 1904-1914.

Nikouei, K., Munoz-Manchado, A.B., and Hjerling-Leffler, J. (2016). BCL11B/CTIP2 is highly expressed in GABAergic interneurons of the mouse somatosensory cortex. J Chem Neuroanat *71*, 1-5.

Noctor, S.C., Martinez-Cerdeno, V., Ivic, L., and Kriegstein, A.R. (2004). Cortical neurons arise in symmetric and asymmetric division zones and migrate through specific phases. Nat Neurosci *7*, 136-144.

Novershtern, N., Subramanian, A., Lawton, L.N., Mak, R.H., Haining, W.N., McConkey, M.E., Habib, N., Yosef, N., Chang, C.Y., Shay, T.*, et al.* (2011). Densely interconnected transcriptional circuits control cell states in human hematopoiesis. Cell *144*, 296-309.

Nowakowski, R.S., Lewin, S.B., and Miller, M.W. (1989). Bromodeoxyuridine immunohistochemical determination of the lengths of the cell cycle and the DNA-synthetic phase for an anatomically defined population. J Neurocytol *18*, 311-318.

Nurnberg, S.T., Rendon, A., Smethurst, P.A., Paul, D.S., Voss, K., Thon, J.N., Lloyd-Jones, H., Sambrook, J.G., Tijssen, M.R., HaemGen, C.*, et al.* (2012). A GWAS sequence variant for platelet volume marks an alternative DNM3 promoter in megakaryocytes near a MEIS1 binding site. Blood *120*, 4859-4868.

Oceguera-Yanez, F., Kim, S.I., Matsumoto, T., Tan, G.W., Xiang, L., Hatani, T., Kondo, T., Ikeya, M., Yoshida, Y., Inoue, H.*, et al.* (2016). Engineering the AAVS1 locus for consistent and scalable transgene expression in human iPSCs and their differentiated derivatives. Methods *101*, 43-55.

Ochi, S., Imaizumi, Y., Shimojo, H., Miyachi, H., and Kageyama, R. (2020). Oscillatory expression of Hes1 regulates cell proliferation and neuronal differentiation in the embryonic brain. Development *147*.

Oppenheim, H. (1923). Lehrbuch der Nervenkrankheiten. *7*, 1774.

Osumi, N., Shinohara, H., Numayama-Tsuruta, K., and Maekawa, M. (2008). Concise Review: Pax6 Transcription Factor Contributes to both Embryonic and Adult Neurogenesis as a Multifunctional Regulator. *26*, 1663-1672.

Oulad-Abdelghani, M., Chazaud, C., Bouillet, P., Sapin, V., Chambon, P., and Dolle, P. (1997). Meis2, a novel mouse Pbx-related homeobox gene induced by retinoic acid during differentiation of P19 embryonal carcinoma cells. Dev Dyn *210*, 173-183.

Owa, T., Taya, S., Miyashita, S., Yamashita, M., Adachi, T., Yamada, K., Yokoyama, M., Aida, S., Nishioka, T., Inoue, Y.U.*, et al.* (2018). Meis1 Coordinates Cerebellar Granule Cell Development by Regulating Pax6 Transcription, BMP Signaling and Atoh1 Degradation. J Neurosci *38*, 1277-1294.

Patel, A.V., Chaney, K.E., Choi, K., Largaespada, D.A., Kumar, A.R., and Ratner, N. (2016). An ShRNA Screen Identifies MEIS1 as a Driver of Malignant Peripheral Nerve Sheath Tumors. EBioMedicine *9*, 110-119.

Penkov, D., San Martin, D.M., Fernandez-Diaz, L.C., Rossello, C.A., Torroja, C., Sanchez-Cabo, F., Warnatz, H.J., Sultan, M., Yaspo, M.L., Gabrieli, A.*, et al.* (2013). Analysis of the DNA-Binding Profile and Function of TALE Homeoproteins Reveals Their Specialization and Specific Interactions with Hox Genes/Proteins. Cell Rep *3*, 1321-1333.

Pichler, I., Marroni, F., Volpato, C.B., Gusella, J.F., Klein, C., Casari, G., De Grandi, A., and Pramstaller, P.P. (2006). Linkage analysis identifies a novel locus for restless legs syndrome on chromosome 2q in a South Tyrolean population isolate. Am J Hum Genet 79, 716-723.

Pliner, H.A., Packer, J.S., McFaline-Figueroa, J.L., Cusanovich, D.A., Daza, R.M., Aghamirzaie, D., Srivatsan, S., Qiu, X., Jackson, D., Minkina, A.*, et al.* (2018). Cicero Predicts cis-Regulatory DNA Interactions from Single-Cell Chromatin Accessibility Data. Mol Cell *71*, 858-871 e858.

Qu, Z., Zhang, H., Huang, M., Shi, G., Liu, Z., Xie, P., Li, H., Wang, W., Xu, G., Zhang, Y.*, et al.* (2016). Loss of ZBTB20 impairs circadian output and leads to unimodal behavioral rhythms. Elife *5*.

Quadrato, G., Nguyen, T., Macosko, E.Z., Sherwood, J.L., Min Yang, S., Berger, D.R., Maria, N., Scholvin, J., Goldman, M., Kinney, J.P.*, et al.* (2017). Cell diversity and network dynamics in photosensitive human brain organoids. Nature *545*, 48-53.

R Core Team (2020). R: A language and environment for statistical computing. R Foundation for Statistical Computing.

Rao, D.D., Senzer, N., Cleary, M.A., and Nemunaitis, J. (2009). Comparative assessment of siRNA and shRNA off target effects: what is slowing clinical development. Cancer Gene Ther *16*, 807-809.

Rubenstein, J.L.R., and Campbell, K. (2013). Comprehensive developmental neuroscience : patterning and cell type specification in the developing CNS and PNS. In Comprehensive developmental neuroscience : patterning and cell type specification in the developing CNS and PNS (Amsterdam: Elsevier/Academic Press), p. 3 volumes (various pagings).

Rubenstein, J.L.R., and Rakic, P. (2013). Comprehensive developmental neuroscience : patterning and cell type specification in the developing CNS and PNS. In (Amsterdam: Elsevier/Academic Press), p. 3 volumes (various pagings).

Ruppert, E. (2019). Restless arms syndrome: prevalence, impact, and management strategies. Neuropsychiatr Dis Treat *15*, 1737-1750.

Sato, M., and Nagano, T. (2005). Involvement of filamin A and filamin A-interacting protein (FILIP) in controlling the start and cell shape of radially migrating cortical neurons. Anat Sci Int *80*, 19-29.

Schormair, B., Kemlink, D., Roeske, D., Eckstein, G., Xiong, L., Lichtner, P., Ripke, S., Trenkwalder, C., Zimprich, A., Stiasny-Kolster, K.*, et al.* (2008). PTPRD (protein tyrosine phosphatase receptor type delta) is associated with restless legs syndrome. Nat Genet *40*, 946-948.

Schormair, B., Zhao, C., Bell, S., Didriksen, M., Nawaz, M.S., Schandra, N., Stefani, A., Hogl, B., Dauvilliers, Y., Bachmann, C.G., et al. (2024). Genome-wide meta-analyses of restless legs syndrome yield insights into genetic architecture, disease biology and risk prediction. Nat Genet.

Schormair, B., Zhao, C., Bell, S., Tilch, E., Salminen, A.V., Putz, B., Dauvilliers, Y., Stefani, A., Hogl, B., Poewe, W.*, et al.* (2017). Identification of novel risk loci for restless legs syndrome in genome-wide association studies in individuals of European ancestry: a meta-analysis. Lancet Neurol *16*, 898-907.

Schulte, D., and Geerts, D. (2019). MEIS transcription factors in development and disease. Development *146*.

Schulte, E.C., Kousi, M., Tan, P.L., Tilch, E., Knauf, F., Lichtner, P., Trenkwalder, C., Hogl, B., Frauscher, B., Berger, K.*, et al.* (2014). Targeted resequencing and systematic in vivo functional testing identifies rare variants in MEIS1 as significant contributors to restless legs syndrome. Am J Hum Genet *95*, 85-95.

Shanmugam, K., Green, N.C., Rambaldi, I., Saragovi, H.U., and Featherstone, M.S. (1999). PBX and MEIS as non-DNA-binding partners in trimeric complexes with HOX proteins. Mol Cell Biol *19*, 7577-7588.

Shen, W.F., Montgomery, J.C., Rozenfeld, S., Moskow, J.J., Lawrence, H.J., Buchberg, A.M., and Largman, C. (1997). AbdB-like Hox proteins stabilize DNA binding by the Meis1 homeodomain proteins. Mol Cell Biol *17*, 6448-6458.

Shin, S., and Vemuri, M. (2009). Culture and Differentiation of Human Neural Stem Cells. Protocols for Neural Cell Culture Springer Protocols Handbooks, 51-73.

Smemo, S., Tena, J.J., Kim, K.H., Gamazon, E.R., Sakabe, N.J., Gomez-Marin, C., Aneas, I., Credidio, F.L., Sobreira, D.R., Wasserman, N.F.*, et al.* (2014). Obesity-associated variants within FTO form long-range functional connections with IRX3. Nature *507*, 371-375.

Spieker, N., van Sluis, P., Beitsma, M., Boon, K., van Schaik, B.D., van Kampen, A.H., Caron, H., and Versteeg, R. (2001). The MEIS1 oncogene is highly expressed in neuroblastoma and amplified in cell line IMR32. Genomics *71*, 214-221.

Spieler, D., Kaffe, M., Knauf, F., Bessa, J., Tena, J.J., Giesert, F., Schormair, B., Tilch, E., Lee, H., Horsch, M.*, et al.* (2014). Restless legs syndrome-associated intronic common variant in Meis1 alters enhancer function in the developing telencephalon. Genome Res *24*, 592-603.

Telley, L., Agirman, G., Prados, J., Amberg, N., Fievre, S., Oberst, P., Bartolini, G., Vitali, I., Cadilhac, C., Hippenmeyer, S.*, et al.* (2019). Temporal patterning of apical progenitors and their daughter neurons in the developing neocortex. Science *364*.

Tonchev, A.B., Tuoc, T.C., Rosenthal, E.H., Studer, M., and Stoykova, A. (2016). Zbtb20 modulates the sequential generation of neuronal layers in developing cortex. Mol Brain *9*, 65.

Toresson, H., Parmar, M., and Campbell, K. (2000). Expression of Meis and Pbx genes and their protein products in the developing telencephalon: implications for regional differentiation. Mech Dev *94*, 183-187.

Trenkwalder, C., Allen, R., Hogl, B., Clemens, S., Patton, S., Schormair, B., and Winkelmann, J. (2018). Comorbidities, treatment, and pathophysiology in restless legs syndrome. Lancet Neurol *17*, 994-1005.

Tucker, E.S., Lehtinen, M.K., Maynard, T., Zirlinger, M., Dulac, C., Rawson, N., Pevny, L., and LaMantia, A.-S. (2010). Proliferative and transcriptional identity of distinct classes of neural precursors in the mammalian olfactory epithelium. Development (Cambridge, England) *137*, 2471-2481.

Verginelli, F., Perin, A., Dali, R., Fung, K.H., Lo, R., Longatti, P., Guiot, M.C., Del Maestro, R.F., Rossi, S., di Porzio, U.*, et al.* (2013). Transcription factors FOXG1 and Groucho/TLE promote glioblastoma growth. Nat Commun *4*, 2956.

Visel, A., Minovitsky, S., Dubchak, I., and Pennacchio, L.A. (2007). VISTA Enhancer Browser--a database of tissue-specific human enhancers. Nucleic Acids Res *35*, D88-92.

Vogel, C., and Marcotte, E.M. (2012). Insights into the regulation of protein abundance from proteomic and transcriptomic analyses. Nat Rev Genet *13*, 227-232.

Waclaw, R.R., Ehrman, L.A., Pierani, A., and Campbell, K. (2010). Developmental origin of the neuronal subtypes that comprise the amygdalar fear circuit in the mouse. J Neurosci *30*, 6944-6953.

Wang, Y., Bagheri-Fam, S., and Harley, V.R. (2005). SOX13 is up-regulated in the developing mouse neuroepithelium and identifies a sub-population of differentiating neurons. Brain Res Dev Brain Res *157*, 201-208.

Wang, Y.Z., Yamagami, T., Gan, Q., Wang, Y., Zhao, T., Hamad, S., Lott, P., Schnittke, N., Schwob, J.E., and Zhou, C.J. (2011). Canonical Wnt signaling promotes the proliferation and neurogenesis of peripheral olfactory stem cells during postnatal development and adult regeneration. J Cell Sci *124*, 1553-1563.

Wichterle, H., Turnbull, D.H., Nery, S., Fishell, G., and Alvarez-Buylla, A. (2001). In utero fate mapping reveals distinct migratory pathways and fates of neurons born in the mammalian basal forebrain. Development *128*, 3759-3771.

Wiegreffe, C., Simon, R., Peschkes, K., Kling, C., Strehle, M., Cheng, J., Srivatsa, S., Liu, P., Jenkins, N.A., Copeland, N.G.*, et al.* (2015). Bcl11a (Ctip1) Controls Migration of Cortical Projection Neurons through Regulation of Sema3c. Neuron *87*, 311-325.

Winkelmann, J., Muller-Myhsok, B., Wittchen, H.U., Hock, B., Prager, M., Pfister, H., Strohle, A., Eisensehr, I., Dichgans, M., Gasser, T.*, et al.* (2002). Complex segregation analysis of restless legs syndrome provides evidence for an autosomal dominant mode of inheritance in early age at onset families. Ann Neurol *52*, 297-302.

Winkelmann, J., Polo, O., Provini, F., Nevsimalova, S., Kemlink, D., Sonka, K., Hogl, B., Poewe, W., Stiasny-Kolster, K., Oertel, W.*, et al.* (2007a). Genetics of restless legs syndrome (RLS): State-of-the-art and future directions. Mov Disord *22 Suppl 18*, S449-458.

Winkelmann, J., Schormair, B., Lichtner, P., Ripke, S., Xiong, L., Jalilzadeh, S., Fulda, S., Putz, B., Eckstein, G., Hauk, S.*, et al.* (2007b). Genome-wide association study of restless legs syndrome identifies common variants in three genomic regions. Nat Genet *39*, 1000-1006.

Winkelmann, J., Czamara, D., Schormair, B., Knauf, F., Schulte, E.C., Trenkwalder, C., Dauvilliers, Y., Polo, O., Hogl, B., Berger, K.*, et al.* (2011). Genome-wide association study identifies novel restless legs syndrome susceptibility loci on 2p14 and 16q12.1. PLoS Genet *7*, e1002171.

Winkelmann, J., Allen, R.P., Hogl, B., Inoue, Y., Oertel, W., Salminen, A.V., Winkelman, J.W., Trenkwalder, C., and Sampaio, C. (2018). Treatment of restless legs syndrome: Evidence-based review and implications for clinical practice (Revised 2017)(section sign). Mov Disord *33*, 1077-1091.

Woodworth, M.B., Greig, L.C., Liu, K.X., Ippolito, G.C., Tucker, H.O., and Macklis, J.D. (2016). Ctip1 Regulates the Balance between Specification of Distinct Projection Neuron Subtypes in Deep Cortical Layers. Cell Rep *15*, 999-1012.

Xiang, P., Wei, W., Hofs, N., Clemans-Gibbon, J., Maetzig, T., Lai, C.K., Dhillon, I., May, C., Ruschmann, J., Schneider, E.*, et al.* (2017). A knock-in mouse strain facilitates dynamic tracking and enrichment of MEIS1. Blood Adv *1*, 2225-2235.

Xiong, L., Catoire, H., Dion, P., Gaspar, C., Lafreniere, R.G., Girard, S.L., Levchenko, A., Riviere, J.B., Fiori, L., St-Onge, J.*, et al.* (2009). MEIS1 intronic risk haplotype associated with restless legs syndrome affects its mRNA and protein expression levels. Hum Mol Genet *18*, 1065-1074.

Yang, N., Chanda, S., Marro, S., Ng, Y.H., Janas, J.A., Haag, D., Ang, C.E., Tang, Y., Flores, Q., Mall, M.*, et al.* (2017). Generation of pure GABAergic neurons by transcription factor programming. Nat Methods *14*, 621-628.

Yao, J., Lai, E., and Stifani, S. (2001). The winged-helix protein brain factor 1 interacts with groucho and hes proteins to repress transcription. Mol Cell Biol *21*, 1962-1972.

Yengo, L., Sidorenko, J., Kemper, K.E., Zheng, Z., Wood, A.R., Weedon, M.N., Frayling, T.M., Hirschhorn, J., Yang, J., Visscher, P.M.*, et al.* (2018). Meta-analysis of genome-wide association studies for height and body mass index in approximately 700000 individuals of European ancestry. Hum Mol Genet *27*, 3641-3649.

Zhang, X., Friedman, A., Heaney, S., Purcell, P., and Maas, R.L. (2002). Meis homeoproteins directly regulate Pax6 during vertebrate lens morphogenesis. Genes Dev *16*, 2097-2107.

Zhang, Y., Liu, T., Meyer, C.A., Eeckhoute, J., Johnson, D.S., Bernstein, B.E., Nusbaum, C., Myers, R.M., Brown, M., Li, W., et al. (2008). Model-based analysis of ChIP-Seq (MACS). Genome Biol 9, R137.

Supplementary Figures

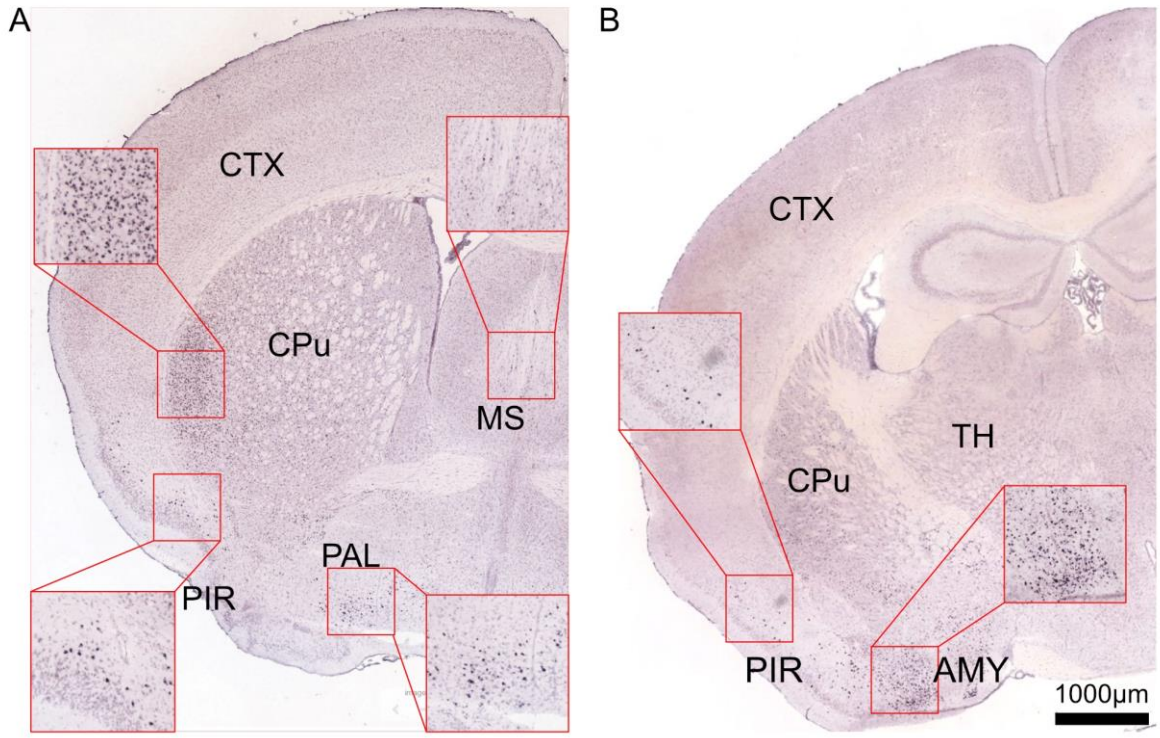

Supplementary Figure 1: *Meis1* in-situ hybridization at P56. Coronoal secions. A) anterior section, B) posterior section). Images from e the Allen Brain Atlas (https://mouse.brain-map.org) AMY: amygdala, CPu: caudoputamen, CTX: cortex, MS: medial septum, PAL: pallium, PIR: piriform cortex, TH: thalamus

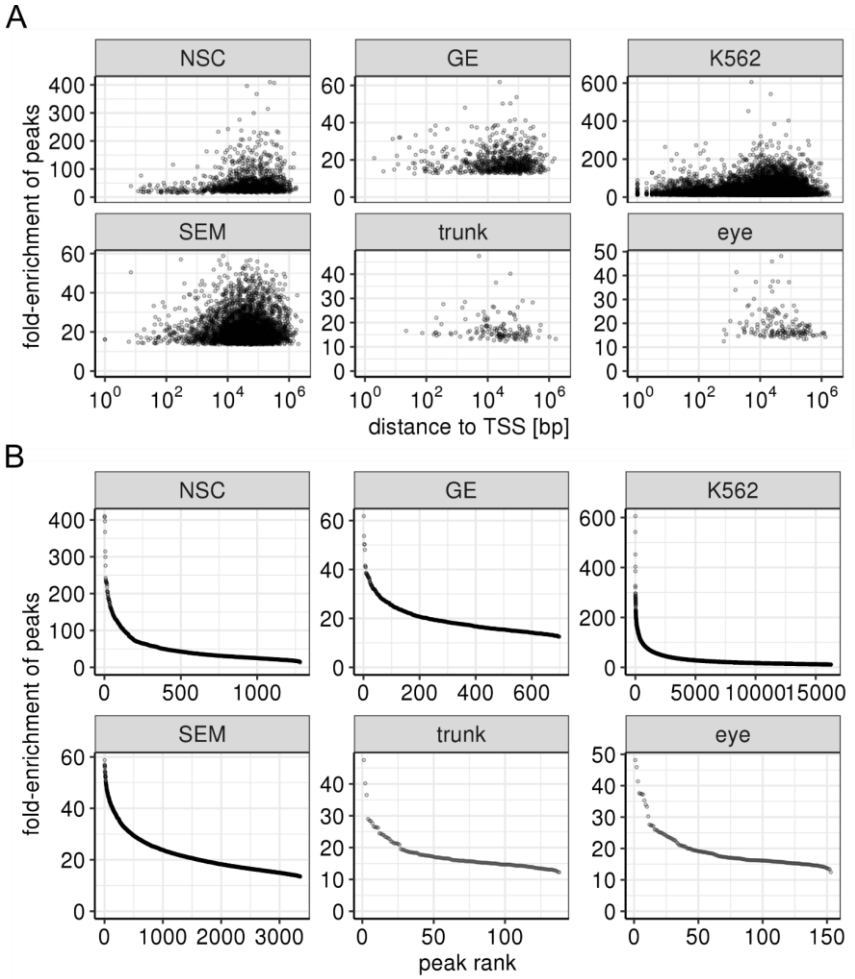

Supplementary Figure 2: ChIP-seq peak enrichment over background. A) fold-enrichment of ChIP-seq peaks in respect to distance to nearest TSS. B) fold-enrichment vs peak rank.

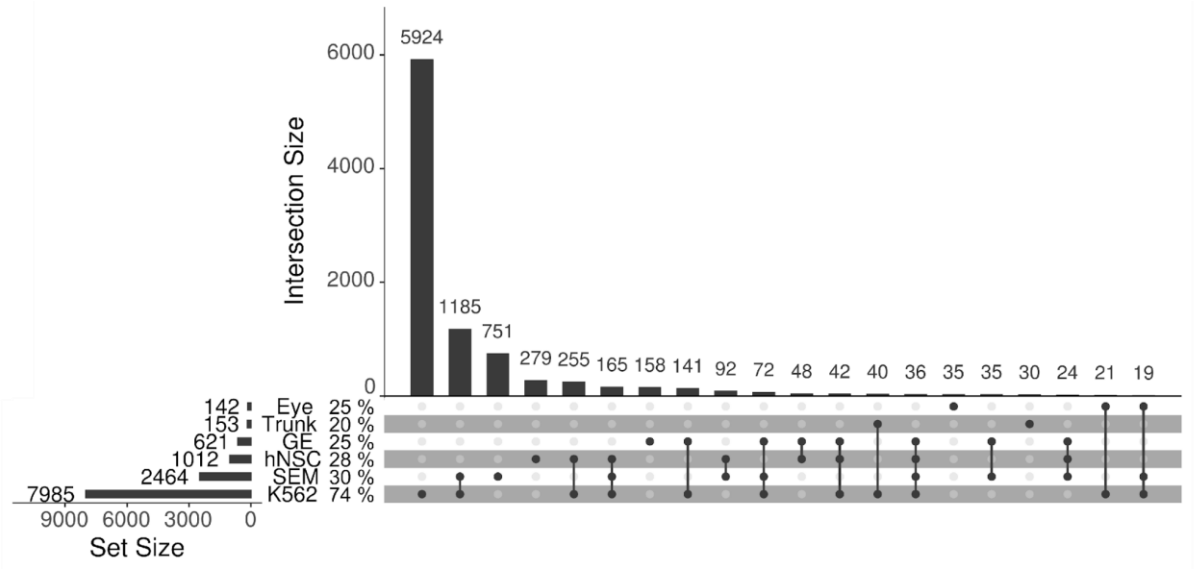

Supplementary Figure 3: Overlap between ChIP-seq target genes. Peaks were assigned to the nearest TSS within 1 Mb using ChIPseeker. Percentage of specific target genes is indicated for each dataset.

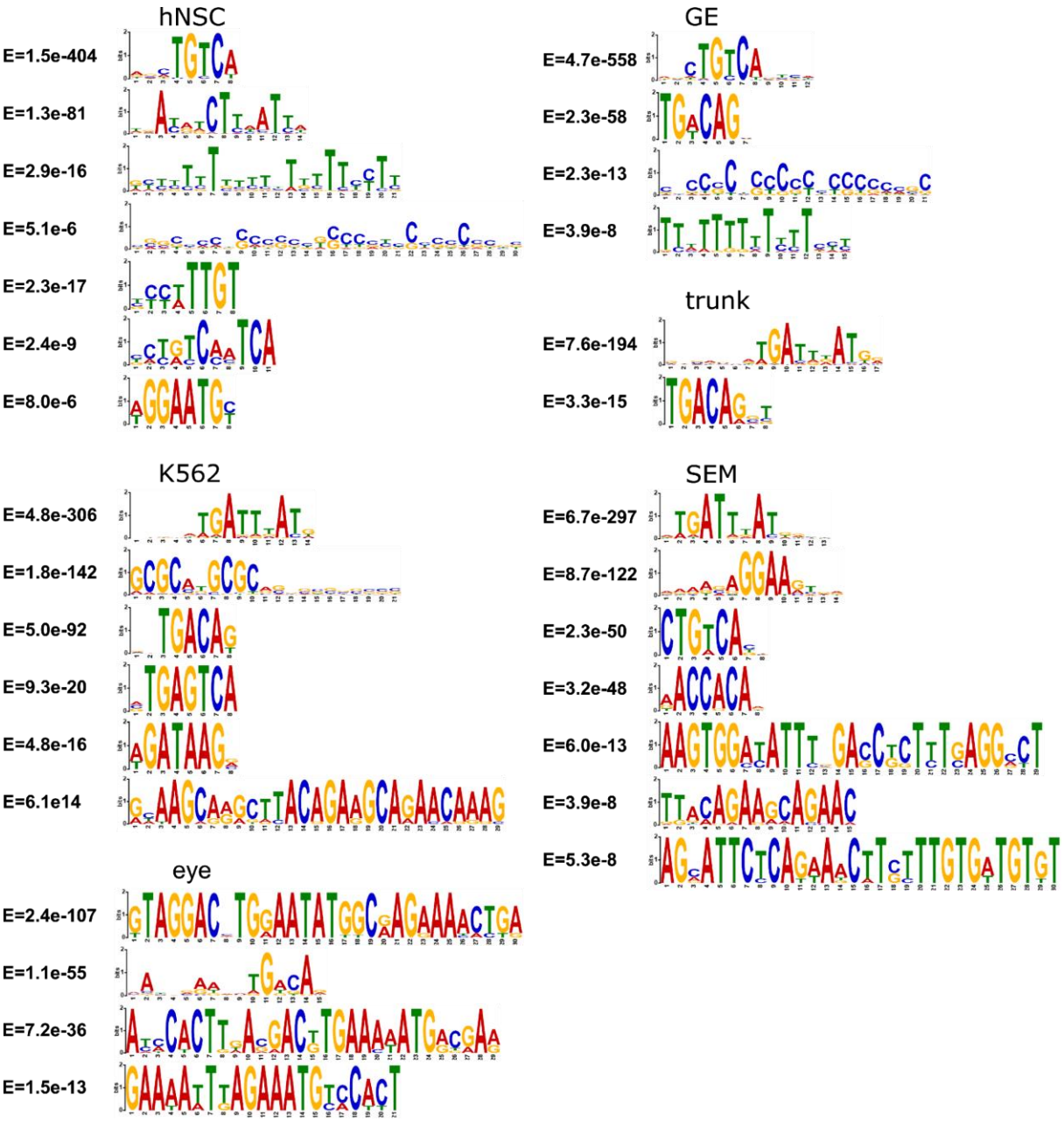

Supplementary Figure 4: De-novo identified binding motifs by MEME. All motifs with E < 10^{-5} are listed. Sequences without central enrichment are highlighted in red.

Figures and Tables

Figures

Tables

Acknowledgments

First and foremost, I want to express my sincere gratitude to Juliane Winkelmann for giving me the opportunity to work in her lab on this fascinating project, and for providing encouragement and continuous support in all matters.

I express the highest appreciation to Daniel Lam for all the skills, wisdom, time, and encouragement he has delivered, helping me to develop my scientific mind and enabling me to pursue various ideas and interests throughout my research.

I want to extend my sincere thanks Konrad Oexle, Barbara Schormair and Aaro Salminen for their critical minds, constructive feedback and inspiring discussions.

I am also grateful to Chen Zhao and Swati Parekh for expert bioinformatics consultation and mentoring.

A special thanks to Monika Zimmerman, Julia Vandrey, Celestine Dutta and Elisabeth Stephan for making the wet lab a pristine environment by providing both atmosphere and excellent working conditions.

I want to appreciate the whole team of the ING for warm working environment, laughs, friendliness and assistance in all aspects.

I want to acknowledge Elisabeth Graf and Sandy Lösecke, as well as Annette Feuchtinger and Ulrike Buchholz for their invaluable help in perfecting experimental techniques.

I am extremely thankful to my family for their support, constant patience and encouragement throughout the years.

Finally, I give my deepest gratitude to Sabrina Weser, providing unwavering support and understanding, as well as professional and moral counsel throughout the most challenging situations.